ISAS - INTERNATIONAL SCHOOL FOR ADVANCED STUDIES

Relativistic Radiation Hydrodynamics in Spherical Flows and Applications to Accretion onto Compact Objects

by

Luca Zampieri

Thesis submitted for the degree of
"Doctor Philosophiae"

Astrophysics Sector

SUPERVISORS

Prof. Aldo Treves

Prof. John C. Miller

Dott. Roberto Turolla

October 1995

Relativistic Radiation Hydrodynamics in Spherical Flows and Applications to Accretion onto Compact Objects

by

Luca Zampieri

Thesis submitted for the degree of
"Doctor Philosophiae"

Astrophysics Sector

SUPERVISORS

Prof. Aldo Treves

Prof. John C. Miller

Dott. Roberto Turolla

October 1995

Acknowledgments

... Noi soli, coscienza di questo

risplender d'astri ...

(David Maria Turoldo)

a Fabiola e ...

CONTENTS

PREFACE

The topic of this thesis is the study of radiation hydrodynamics in spherical accretion flows around compact objects and its relevance in connection with the modelling of compact X–ray sources. In the last decades, the accretion of matter onto black holes and neutron stars has been recognized as the mechanism at the origin of the high energy emission from Galactic compact sources and Active Galactic Nuclei. Since then, the study of the accretion process in a variety of different environments has became an issue of fundamental importance in theoretical astrophysics. In particular, the analysis of the interaction between matter and radiation is certainly a key ingredient in formulating physically realistic models which can account for the observational properties of X–ray sources. Moreover, in the vicinity of compact objects relativistic effects, such as gravitational redshift, aberration and advection of photons, become important and a general relativistic approach to the study of radiative transfer in differentially moving media is definitely required. In this thesis, this study has been carried out by means of a general relativistic treatment of the radiative transfer equation, which exploits the expansion of the specific intensity of the radiation field into moments (Thorne 1981). In order to determine self–consistently the dynamics of the accretion flow, which is influenced by the interaction with the radiation field, the moment equations are coupled to the conservation equations for the matter fluid and then solved numerically using two original codes suitably designed for the integration of systems of partial differential equations of elliptic (stationary) and hyperbolic (time–dependent) type, respectively. A brief presentation of this general relativistic moment formalism is sketched in the first part of *Chapter 1*. The assumption of spherical symmetry is certainly not adequate to describe in full realism much of the phenomenology observed in compact X–ray sources and it is not my intention to go deeply into a detailed treatment and modelling of these objects. However, there are some classes of compact X–ray sources, such as bright Low

Mass X–ray Binaries accreting near the Eddington limit and old isolated neutron stars accreting from the interstellar medium, for which radiative transfer in one dimensional flows might give at least a qualitative indication of the expected emission properties. In the second part of Chapter 1, I will briefly review, the observational data and the present understanding of these sources and, in connection with this, I will discuss the possible relevance of the radiative transfer calculations in spherical accretion flows which is carried out in the following chapters.

The original results which I have obtained from the investigation of radiation hydro-dynamics are contained in the following three chapters. In *Chapter 2* the effects of bulk acceleration of photons in radially inflowing/outflowing, optically thick atmospheres will be investigated. In fact, in the scattering process, in addition to thermal motion also ordered bulk motion of the electrons can affect the photon distribution in phase–space. To study this effect, we solve analytically the moment equations in two different ways: the first method follows closely the classical approach by Payne & Blandford (1981), whereas the second is presented here for the first time. The spectrum shows both a shift in frequency and the formation of a typical high/low energy tail for inflowing/outflowing atmospheres. This effect, called dynamical comptonization, is produced entirely by the bulk motion of the gas and become relevant if the quantity $\tau v/c$, where τ is the electron scattering optical depth and v is the flow velocity, is of order unity. In the second half of Chapter 2, we will investigate the role of bulk acceleration of photons in connection with the formation of the spectrum in neutron stars accreting near the Eddington limit. The flow dynamics and the frequency–dependent transfer problem are self–consistently solved for a cold, scattering atmosphere, including General Relativity. The relevance of these results in connection with the observed spectral properties of bright Low Mass X–ray Binaries with a high energy tail, and of Cygnus X–2 in particular, is also discussed.

The second topic of relativistic radiative transfer on which I concentrated is the study of the thermal and radiative structure of static, geometrically thin atmospheres around neutron stars accreting well below the Eddington limit. The leading motivation for this

study stems from the determination of X–ray spectral properties of old isolated neutron stars accreting from the interstellar medium, which may show up as very weak, soft X–ray sources, as originally suggested by Ostriker, Rees & Silk (1970). This investigation has been carried out on the wake of the seminal paper by Zel'dovich & Shakura (1969) and the results which we have obtained are presented in *Chapter 3*. We have proved that two distinct types of solutions, characterized by very different temperatures, exist for a certain range of accretion rates: in the low temperature models ($T \sim 10^6$ K), the opacity is dominated by free–free and matter and radiation are in local thermodynamical equilibrium, whereas the newly discovered "hot" solutions have temperatures $\sim 10^9$ K and are dominated by self–comptonization of bremsstrahlung photons. We have found also that at very low accretion rates there is a unique solution, the "cold" one discovered by Zel'dovich & Shakura and, since we are interested in investigating the spectral properties of neutron stars accreting at very low rates, we focussed on the determination of the spectral properties of these solutions. As it will be discussed in Chapter 3, the spectra emitted by cold, thermalized atmospheres are significantly distorted with respect to a black body at the star's effective temperature, showing both a broad maximum and a high energy tail which become progressively more pronounced as the accretion rate decreases. In the remainder of Chapter 3, on the basis of the actual form of the spectrum emitted by the atmospheres of neutron stars accreting at low rates and in the hypothesis that a relic magnetic field can channel the accretion flow onto the polar caps, a detailed investigation of the observability of old isolated neutron stars accreting from the interstellar medium has been presented. Old neutron stars might contribute up to 10% to the detected soft X–ray background, although in this case about 10 sources per $\deg^{-2}$ should be observable at low sensitivity limits ($\sim 10^{-3}$ counts s^{-1}) by ROSAT.

Compact X–ray sources are usually variable on a wide range of time–scales and a lot of information about the physical processes acting in these sources can be inferred by a detailed observational and theoretical investigation of their variability. Then, on

the basis of the increasing interest toward the time–dependent analyses of the X–ray signal from compact X–ray sources, we have started a careful study of time–dependent radiative transfer in spherical symmetry, which is culminated with the construction of a lagrangian time–dependent numerical code for the solutions of radiation hydrodynamics equations. At present, this code has been applied to the investigation of the stability properties of spherical accretion onto black holes, presented in *Chapter 4*. We decided to make the first application of this code to black hole accretion since it is quite an interesting problem per sé and, although it has been extensively studied starting from the early seventies, no definite proof of the stability of its solutions had yet been given. As shown by many authors, the flow properties are fixed once the accretion rate is specified, so that stationary solutions can be completely characterized by their position in the accretion rate–luminosity plane. It was already known since the middle eighties that, on this plane, two disconnected branches of solutions exist for a certain range of accretion rates, a high and a low luminosity branch, characterized by very different thermal and radiative processes. We have shown that the low luminosity branch is completely stable, whereas part of the high luminosity branch is unstable to thermal perturbations and tends to develop a hydrodynamical shock at about 10^3–10^4 gravitational radii.

Finally, I take the opportunity to list all the relevant papers from which all or part of the results presented in this thesis have been taken: for Chapter 1 Nobili, Turolla & Zampieri (1993), Zampieri, Miller & Turolla (1995); for Chapter 2 Zampieri, Turolla & Treves (1993); for Chapter 3 Turolla *et al.* (1994), Zampieri *et al.* (1995), Zane *et al.* (1995); for Chapter 4 Zampieri, Miller & Turolla (1995).

List of Frequently Used Symbols

ISM	Interstellar Medium
LMXB	Low Mass X–ray Binary
NS	Neutron Star
ONS	Old Neutron Star
XRB	X–ray Background

CHAPTER 1
INTRODUCTION

This thesis contains a thorough investigation of the transfer of radiation in spherically symmetric accretion flows onto compact objects within a variety of different assumptions. Although they rely on such a common framework, each of the following three chapters will deal with a different and specific aspect of relativistic radiation hydrodynamics, namely the effects of dynamical comptonization in spherical flows, the study of the thermal structure and the formation of the spectrum in atmospheres of neutron stars accreting at low rates and the stability properties of time–dependent, spherical accretion onto black holes. All but the last of these topics have been carefully investigated having in mind their possible application to certain classes of astrophysical sources in which they could be of importance. In this respect, as it will be discussed in sections 1.2 and 1.3, the results contained in the second and third chapters could be relevant in connection with the observed phenomenology of bright Low Mass X–ray Binaries accreting near the Eddington limit and with the detectability issue of Old isolated Neutron Stars accreting from the interstellar medium.

The first part of this introductory chapter (section 1.1) contains a brief review of the derivation of the relativistic radiation hydrodynamics equations in spherical symmetry which will be extensively applied in the remainder of this thesis to the study of the transfer of radiation in accretion flows onto compact objects. In sections 1.2 and 1.3, we will briefly sketch the present observational status and theoretical understanding of bright Low Mass X–ray Binaries (LMXBs) and Old isolated Neutron Stars (ONSs). We argue that the spectral effects of dynamical comptonization produced by bulk motion in a radial inflow can be of importance in explaining the high energy tails of the spectra emitted by LMXBs and that radiative transfer calculations in spherical symmetry can be assumed valid in describing the emission properties of ONSs, provided that the effects of the reduced emitting area are taken into account.

1.1 RELATIVISTIC RADIATION HYDRODYNAMICS
IN SPHERICAL SYMMETRY

Radiative transfer in differentially–moving media has been extensively investigated in the past and a large body of literature is available on this subject (see Mihalas & Mihalas 1984 and references therein). Despite the large efforts, however, works dealing with the transfer of radiation through media moving at relativistic speeds are comparatively few. The special relativistic transfer equation was firstly derived by Thomas (1930) and, including Thomson scattering, by Simon (1963) and Castor (1972); a thorough derivation can be found in the monograph by Mihalas & Mihalas. Stationary solutions in spherical symmetry were discussed by Mihalas (1980), Mihalas, Winkler & Norman (1984) and Hauschildt & Wehrse (1991). Radiative transfer in curved spacetimes was investigated by Lindquist (1966), Anderson & Spiegel (1972), Schmid–Burgk (1978), Thorne (1981), Schinder (1988), Schinder & Bludman (1989), Anile & Romano (1992) and Nobili, Turolla & Zampieri (1993). All the solutions of the relativistic transfer problem found up to now were obtained using a number of different approaches: in some cases the transfer equation is directly solved for the specific intensity I of the radiation field, as in the Tangent Ray Method (Mihalas, Kunasz & Hummer 1975; Mihalas 1980; Schinder & Bludman 1989) and in the DOME method (Hauschildt & Wehrse 1991); in certain circumstances it is assumed that the normalized intensity (i.e. the specific intensity divided by the radiation energy density) is slowly varying along the characteristics of the radiative transfer equation and then flux–limited expressions for the radiative flux and stress tensor can be obtained, as in the Flux–limited Diffusion Theory (Levermore & Pomraning 1981; Melia & Zylstra 1991; Anile & Romano 1992); finally, in other situations the angular dependence is removed by expanding I into moments and the moment equations are then integrated (Thorne 1981; Nobili, Turolla & Zampieri 1993). Each method has both advantages and disadvantages which depend on the specific problem considered.

In the following we will concentrate on the covariant moment formalism introduced

by Thorne (1981), which can be profitably used to get, at least, an approximate solution for I by introducing ,"a priori", reasonable expressions for the Eddington factors which relate moments of order higher than the truncation order to any of the lower order moments.

We will denote with u^α the 4–velocity of the reference frame comoving with the gas flow. In this frame the energy and momentum conservation equations can be obtained by projecting the 4–divergence of the stress–energy tensor of the matter plus radiation fluid along u^α and orthogonal to it, giving (we follow the conventions that Greek indices run from 0 to 3 and covariant derivatives are denoted with a semi–colon; we use a spacelike signature $(-,+,+,+)$)

$$u_\alpha \left(T_M^{\alpha\beta} + T_R^{\alpha\beta} \right)_{;\beta} = 0 \,, \tag{1.1}$$

$$h_{\gamma\alpha} \left(T_M^{\alpha\beta} + T_R^{\alpha\beta} \right)_{;\beta} = 0 \,, \tag{1.2}$$

where $h_{\gamma\alpha} = g_{\gamma\alpha} + u_\gamma u_\alpha$ is the projection tensor orthogonal to the 4–velocity and

$$T_M^{\alpha\beta} = (e+p)\, u^\alpha u^\beta + p g^{\alpha\beta} \,, \tag{1.3}$$

$$T_R^{\alpha\beta} = \mathcal{M} u^\alpha u^\beta + 2\mathcal{M}^{(\alpha} u^{\beta)} + \mathcal{M}^{\alpha\beta} + \frac{1}{3}\mathcal{M} h^{\alpha\beta} \tag{1.4}$$

are the matter and radiation stress–energy tensors, respectively; e and p are the energy density and pressure of the gas. This system of equations must be supplemented with the rest–mass conservation equation

$$(\rho u^\alpha)_{;\alpha} = 0 \,, \tag{1.5}$$

where ρ is the rest–mass density of the matter measured in the comoving frame. In equation (1.4) the stress–energy tensor of the radiation field is expressed in terms of the Projected Symmetric Trace–Free (PSTF) moments (Thorne 1981)

$$\mathcal{M}^{\alpha_1 \cdots \alpha_k} = \frac{1}{c} \left(\int I n^{\alpha_1} ... n^{\alpha_k} d\Omega \right)^{Trace-Free} \,, \tag{1.6}$$

where $I = I(x^\alpha, p^\alpha)$ is the specific intensity of the radiation field and n^α is the unit vector which gives the direction of propagation of a photon as seen in the rest frame of the fiducial observer u^α. Integration is over solid angle in the projected space and "Trace–Free" denotes the consequence of the usual tensor operation. By definition, the PSTF moments are symmetric tensors which lie entirely in the projected space and represent the relativistic analogue of the classical moments of the specific intensity (see e.g. Chandrasekhar 1960). In terms of PSTF moments, I can be written as

$$I = c \sum_{k=0}^{\infty} \frac{(2k+1)!!}{4\pi k!} \mathcal{M}^{\alpha_1 \ldots \alpha_k} n_{\alpha_1} \ldots n_{\alpha_k} \,. \tag{1.7}$$

The specific intensity obeys the general relativistic equation of radiative transfer

$$2 \frac{dN}{dl} = S \,, \tag{1.8}$$

where $N = (c^2/2h)(I/\nu^3)$ is the photon occupation number ($\nu = cu^\alpha p_\alpha/h$ is the photon frequency measured in the comoving frame), l is a non–affine parameter along the photon trajectory in phase–space and S is a source function which describes the effects of the interaction between matter and radiation, its actual form depending on the radiative processes which are considered. The moments of the source function, $S^{\alpha_1 \ldots \alpha_k}$, can be defined in analogy with equation (1.6). If there is no interaction, $S = 0$ and N is conserved along each photon trajectory. Moment equations can be obtained taking the PSTF moments (i.e. projecting orthogonal to u^α, performing the symmetrization and removing the trace) of the relativistic transfer equation (1.8) and this gives rise to an infinite hierarchy of differential equations.

In spherical symmetry we can define a local orthonormal frame comoving with the flow as $\{e_{\hat{0}}, e_{\hat{r}}, e_{\hat{\theta}}, e_{\hat{\varphi}}\}$, with $e_{\hat{0}} = u$, $e_{\hat{r}}$ being in the radial direction and $e_{\hat{\theta}}$, $e_{\hat{\varphi}}$ being orthogonal to each other and to $e_{\hat{r}}$. Since in this case I and S are invariant under rotations of the photon direction n^α about $e_{\hat{r}}$, it is possible to show that all of the components of each PSTF moment of rank k can be evaluated in the comoving frame as functions of the radial one

$$W_k \equiv \mathcal{M}^{\hat{r} \ldots \hat{r}} = 2\pi \frac{k!(2k+1)}{(2k+1)!!} \frac{1}{c} \int I P^k(\mu) d\mu \,, \tag{1.9}$$

$$S_k \equiv \mathcal{S}^{\hat{r}...\hat{r}} = 2\pi \frac{k!(2k+1)}{(2k+1)!!} \frac{h}{c^3} \int \nu^3 S P^k(\mu) d\mu, \tag{1.10}$$

where $P^k(\mu)$ is the Legendre polynomial of order k, $\mu = n^{\hat{r}}$ and $\hat{\alpha}$ denotes the $e_{\hat{\alpha}}$ component. In particular

$$\mathcal{M} = W_0, \tag{1.11}$$

$$\mathcal{M}^\alpha = W_1 e_{\hat{r}}^\alpha, \tag{1.12}$$

$$\mathcal{M}^{\alpha\beta} = W_2 \left(e_{\hat{r}}^\alpha e_{\hat{r}}^\beta - \frac{1}{2} e_{\hat{\theta}}^\alpha e_{\hat{\theta}}^\beta - \frac{1}{2} e_{\hat{\varphi}}^\alpha e_{\hat{\varphi}}^\beta \right), \tag{1.13}$$

In the following we will denote with w_k and s_k the frequency integrated radial moments of the specific intensity and the source function, respectively:

$$w_k(r) = \int_0^\infty W_k(r,\nu) d\nu, \tag{1.14}$$

$$s_k(r) = \int_0^\infty S_k(r,\nu) d\nu. \tag{1.15}$$

It is easy to see that w_0 is the radiation energy density and $c w_1$ is the radial component of the radiative flux.

Moments equations form a recursive system of differential equations which is not closed, since at any given order k_{max} it contains moments up to order k_{max+1} in the frequency–integrated case (and k_{max+2} in the frequency–dependent case). This means that, in order to use these equations for calculations, it is necessary to make some "ad hoc" assumption to close the system (see e.g. Fu 1987, Cernohorsky & Bludman 1994 and references therein) and this is usually done on physical grounds by introducing suitable closure functions which relate $W_{k_{max+1}}/w_{k_{max+1}}$ (and $W_{k_{max+2}}$ where necessary) to moments of lower order. Since the behaviour of all of the moments is known in the asymptotic limits (when the interaction between matter and radiation is either very strong or completely absent), it is sufficient to prescribe a reasonable smooth function that connects these two limits (see e.g. Nobili, Turolla & Zampieri 1991). Clearly uncertainties in this will introduce some error into the calculation of the lower order moments, whose magnitude will be dependent on the closure relation but turns out to

be no larger than $\sim 15\%$ for the range of parameter values typical for real astrophysical flows (Turolla & Nobili 1988).

In the following chapters of this thesis, this formalism will be applied to the solution of radiative transfer in both stationary and time–dependent flows. Since the equations and the assumptions are different in the two cases, we will discuss them separately. Finally, we note that in the remainder of this thesis we will adopt the notation and conventions introduced in this section.

1.1.1 Stationary regime

Now, we assume that the spacetime is stationary and can be described by the spherically symmetric, Schwarzschild line–element

$$ds^2 = -\left(1 - \frac{r_g}{r}\right) c^2 dt^2 + \left(1 - \frac{r_g}{r}\right)^{-1} dr^2 + r^2(d\theta^2 + \sin^2\theta \, d\phi^2), \qquad (1.16)$$

where $r_g = 2GM/c^2$ is the gravitational radius.

Using the line–element (1.16), the equations of radiation hydrodynamics (1.1), (1.2) and (1.5) in the stationary regime (i.e. putting the derivatives at fixed r equal to zero) can be cast in the form (see Nobili, Turolla & Zampieri 1991)

$$e' - (P + e)\frac{\rho'}{\rho} + \frac{x r_g s_0}{yv/c} = 0 \qquad \text{Energy equation}, \qquad (1.17)$$

$$(P + e)\frac{y'}{y} + P' + \frac{x r_g s_1}{y} = 0 \qquad \text{Euler equation}, \qquad (1.18)$$

$$\frac{(vy)'}{(vy)} + \frac{\rho'}{\rho} + 2 = 0 \qquad \text{Continuity equation}, \qquad (1.19)$$

where a prime denotes derivative with respect to $\ln x$ ($x = r/r_g$ is the adimensional Eulerian radial coordinate), $y = \sqrt{(1 - 1/x)/(1 - v^2/c^2)}$ and v is the velocity of the gas with respect to the fixed Eulerian frame. Here v is assumed positive for outward motion. In the following we will consider also situations in which v will be positive for inward motion (accretion flows); in this case, all the equations presented in this section are valid provided that v is turned in $-v$ and the accretion rate $\dot{M}$ in $-\dot{M}$. It

is possible to show that equations (1.17)–(1.19) can be written in the alternative form (Nobili, Turolla & Zampieri 1991)

$$\frac{T'}{T} - (\gamma - 1)\frac{\rho'}{\rho} + \frac{x r_g s_0}{B(P + e)yv/c} = 0,\tag{1.20}$$

$$\left(\frac{v^2}{c^2} - \frac{v_s^2}{c^2}\right)\frac{(yv)'}{(yv)} - 2\frac{v_s^2}{c^2} + \frac{1}{2xy^2} - \frac{x r_g}{(P + e)yv/c}\left[(\gamma - 1)s_0 - \frac{v}{c}s_1\right] = 0,\tag{1.21}$$

$$\dot{M} = 4\pi x^2 r_g^2 \rho yv,\tag{1.22}$$

where T is the gas temperature, $\gamma = 1 + b/B$ is the local adiabatic exponent, $v_s^2 \equiv \partial P/\partial\rho|_{entropy} = a + b^2/B$ is the adiabatic sound speed squared and a, b and B are ancillary thermodynamic quantities defined by

$$B = \frac{T}{P + e}\left(\frac{\partial e}{\partial T}\right)_\rho, \qquad a = \frac{\rho}{P + e}\left(\frac{\partial P}{\partial\rho}\right)_T, \qquad b = \frac{T}{P + e}\left(\frac{\partial P}{\partial T}\right)_\rho.\tag{1.23}$$

In the following only the first two moment equations ($k = 0, 1$) are retained and we assume that this suffices to ensure a satisfactory treatment of radiative transfer at all optical depths, the main reason for such a choice being just to make numerical solution an affordable task. The maximal fractional error induced by taking into account only the first two frequency integrated moments w_0 and w_1 was estimated by Turolla & Nobili (1988) to be about 15%, so that our approximation seems to be not too drastic. Upon truncation of the moment expansion to $k_{max} = 1$, the two frequency–dependent moment equations governing the radiation field can be directly derived from equation (5.10a) of Thorne (1981); they read

$$\frac{W_1}{W_0}\left[\frac{\partial\ln W_1}{\partial\ln x} + 2 + \frac{d\ln y}{d\ln x}\left(1 - \frac{\partial\ln W_1}{\partial\ln\nu}\right)\right] + \frac{v}{c}\left[\frac{\partial\ln W_0}{\partial\ln x} + \right.$$

$$\left. + \left(\frac{d\ln(yv)}{d\ln x} + 2\right)\left(1 - \frac{1}{3}\frac{\partial\ln W_0}{\partial\ln\nu}\right) - \left(\frac{d\ln(yv)}{d\ln x} - 1\right)\frac{W_2}{W_0}\frac{\partial\ln W_2}{\partial\ln\nu}\right] = \frac{S_0 x r_g}{yW_0},\tag{1.24}$$

$$\frac{1}{3}\frac{\partial\ln W_0}{\partial\ln x} + \frac{d\ln y}{d\ln x}\left(1 - \frac{1}{3}\frac{\partial\ln W_0}{\partial\ln\nu}\right) + \frac{W_2}{W_0}\left(\frac{\partial\ln W_2}{\partial\ln x} + 3 - \frac{d\ln y}{d\ln x}\frac{\partial\ln W_2}{\partial\ln\nu}\right) +$$

$$+\frac{v}{c}\left[\frac{W_1}{W_0}\frac{\partial \ln W_1}{\partial \ln x}+\frac{1}{5}\frac{W_1}{W_0}\left(7\frac{d\ln(yv)}{d\ln x}+8\right)-\frac{1}{5}\frac{W_1}{W_0}\left(3\frac{d\ln(yv)}{d\ln x}+2\right)\frac{\partial \ln W_1}{\partial \ln \nu}-\right.$$

$$\left.-\frac{W_3}{W_0}\left(\frac{d\ln(yv)}{d\ln x}-1\right)\left(1+\frac{\partial \ln W_3}{\partial \ln \nu}\right)\right]=\frac{S_1 x R_g}{y W_0}. \tag{1.25}$$

Here the W_k have the dimensions of erg cm^{-3} Hz^{-1}, whereas the cS_k are in units of erg cm^{-3} s^{-1} Hz^{-1}. The presence of both a gravitational field and a non–vanishing velocity gradient introduces a *frequency–mixing* of moments related to the ν–derivatives of W_1 appearing in equation (1.24) and of W_0 in equation (1.25); as a consequence, in the relativistic transfer problem it is not possible, in general, to combine the two moment equations into a single second order partial differential equation for the radiation energy density, as in the newtonian case. For the sake of concreteness, we shall write in the following the explicit expressions for the source moments when the dominant radiative processes are bremsstrahlung and electron scattering. This particular case can be thought, in fact, to be well representative of quite general astrophysical situations in which magnetic fields play no substantial role. We assume that Kirchhoff's law is valid (emitters and absorbers in thermodynamic equilibrium throughout the fluid) and that non–conservative scattering can be treated in the Fokker–Planck approximation by means of Kompaneets equation (Rybicki and Lightman 1979). Kompaneets equation holds only for a thermal, non–relativistic electron distribution and if the photon energy is small compared to the electron rest mass. Recent calculations (Loeb, McKee and Lahaw 1991) show, however, that Kompaneets equation can be safely used for electron temperatures up to $\sim 2 \times 10^9$ K (see also Prasad *et al.* 1988; Shestakov, Kershaw & Prasad 1988 for a general treatment of the Compton Fokker–Planck equation). Under these assumptions the source moments can be written as (see equations (6.6) and (6.14) of Thorne 1981)

$$\frac{S_0 x r_g}{y W_0}=\frac{k_{es}\rho x r_g}{y}\left\{\frac{kT}{m_e c^2}\left[\frac{\partial^2 \ln W_0}{\partial(\ln \nu)^2}+\left(\frac{\partial \ln W_0}{\partial \ln \nu}+\frac{h\nu}{kT}-3\right)\frac{\partial \ln W_0}{\partial \ln \nu}+\right.\right.$$

$$\left.\left.+\frac{h\nu}{kT}+\frac{c^3 W_0}{4\pi K T \nu^2}\left(\frac{\partial \ln W_0}{\partial \ln \nu}-1\right)\right]+\frac{1}{k_{es}W_0}\left(\epsilon_{ff}-k_{ff}W_0\right)\right\}, \tag{1.26}$$

$$\frac{S_1 x r_g}{y W_0} = -\frac{k_{es}\rho x r_g}{y}\left(1 + \frac{k_{ff}}{k_{es}}\right)\frac{W_1}{W_0}. \tag{1.27}$$

In equations (1.26) and (1.27) k_{es} is the electron scattering opacity and ϵ_{ff} and k_{ff} are the frequency–dependent free–free emissivity and opacity; using the Kirchhoff law the free–free emissivity can be re–expressed as $\epsilon_{ff} = k_{ff}B_\nu(T)$, where $B_\nu(T)$ is the Planck function.

The first two frequency integrated moment equations can be obtained by integrating in frequency equations (1.24) and (1.25) and requiring that $W_k \to 0$ as $\nu \to \infty$; they read

$$w_1' + \frac{v}{c}w_0' + \frac{v}{c}w_2\left(\frac{(vy)'}{vy} - 1\right) + 2w_1\left(1 + \frac{y'}{y}\right) + \frac{4}{3}\frac{v}{c}w_0\left(\frac{(vy)'}{vy} + 2\right) = \frac{s_0 x r_g}{y}, \tag{1.28}$$

$$w_2' + \frac{v}{c}w_1' + \frac{1}{3}w_0' + w_2\left(3 + \frac{y'}{y}\right) + 2\frac{v}{c}w_1\left(\frac{(vy)'}{vy} + 1\right) + \frac{4}{3}\frac{y'}{y}w_0 = \frac{s_1 x r_g}{y}, \tag{1.29}$$

where a prime denotes again derivative with respect to $\ln x$. In equations (1.28) and (1.29) w_0 and w_1 have the dimensions of energy density and cs_0 and cs_1 are in units of erg cm^{-3} s^{-1}. Neglecting the non–linear term which accounts for induced emission in the Kompaneets equation, the frequency integrated source moments can be written

$$s_0 = \rho(\bar{\epsilon} - \kappa_0 w_0) + k_{es}\rho w_0 \frac{4K}{m_e c^2}(T - T_\gamma), \tag{1.30}$$

$$s_1 = -\rho\kappa_1 w_1, \tag{1.31}$$

Here $\bar{\epsilon}$ is the frequency integrated free–free emissivity, k_0 and k_1 are the absorption and flux mean opacities and T_γ is the radiation temperature, defined by

$$T_\gamma = \frac{1}{4K}\frac{\int_0^\infty h\nu W_0(r,\nu)\,d\nu}{\int_0^\infty W_0(r,\nu)\,d\nu}\;\text{K}. \tag{1.32}$$

1.1.2 Time–dependent regime

We next introduce the spherically symmetric, comoving–frame line element

$$ds^2 = -a^2 c^2 dt^2 + b^2 d\mu^2 + r^2 \left(d\theta^2 + \sin^2 \theta d\varphi^2 \right) , \tag{1.33}$$

where t and μ are the Lagrangian time and the comoving radial coordinate (taken to be the rest mass contained within a comoving spherical shell), r is the Eulerian radial coordinate and a and b are two functions of t and μ which need to be computed.

In order to calculate self–consistently the metric tensor $g^{\alpha\beta}$ which describes the geometry of the space–time, we need to solve the Einstein Field Equations for the system

$$R^{\alpha\beta} - \frac{1}{2} g^{\alpha\beta} R = \frac{8\pi G}{c^4} \left(T_M^{\alpha\beta} + T_R^{\alpha\beta} \right) . \tag{1.34}$$

The complete system of radiation hydrodynamic equations (1.1), (1.2) and (1.5) along with the Einstein Field Equations (1.34) and the line element (1.33) can be cast in the form (Rezzolla & Miller 1994; Zampieri, Miller & Turolla 1995)

$$e_t - h\rho_t + acs_0 = 0 \quad \text{Energy equation}, \tag{1.35}$$

$$u_t + ac \left[\frac{\Gamma}{b} \left(\frac{p_\mu + bs_1}{\rho h} \right) + \frac{4\pi G r}{c^4} \left(p + \frac{1}{3} w_0 + w_2 \right) + \right.$$
$$\left. + \frac{GM}{c^2 r^2} \right] = 0 \quad \text{Euler equation}, \tag{1.36}$$

$$\frac{(\rho r^2)_t}{\rho r^2} + ac \left(\frac{u_\mu - 4\pi G b r w_1 / c^4}{r_\mu} \right) = 0 \quad \text{Continuity equation}, \tag{1.37}$$

$$b = \frac{1}{4\pi r^2 \rho} , \tag{1.38}$$

$$\frac{(ah)_\mu}{ah} + \frac{h\rho_\mu - e_\mu + bs_1}{h\rho} = 0 , \tag{1.39}$$

$$M_\mu = \frac{4\pi r^2 r_\mu}{c^2} \left(e + w_0 + \frac{u}{\Gamma} w_1 \right) , \tag{1.40}$$

where

$$u = \frac{r_t}{ac} \tag{1.41}$$

is the radial component of the fluid 4–velocity measured in the fixed Eulerian frame, $\Gamma = (1 + u^2 - 2GM/c^2r)^{1/2} = r_\mu/b$ is the general relativistic analogue of the Lorentz factor, M represents the effective gravitational mass (for black hole + gas + radiation) contained within radius r and $h = (e+p)/\rho$ is the specific enthalpy. Here, the subscripts t and μ denote partial derivatives with respect to the corresponding variables and s_0 and s_1 are the frequency–integrated radial moments of the source function S. In spherical symmetry and with the line–element (1.33), the first two frequency integrated moment equations can be written (Thorne 1981, equation [5.10c])

$$\frac{1}{b^{4/3}r^{8/3}}\left(w_0 b^{4/3} r^{8/3}\right)_t + \frac{c}{abr^2}(w_1 a^2 r^2)_\mu + \left(\frac{b_t}{b} - \frac{r_t}{r}\right) w_2 - acs_0 = 0\,, \qquad (1.42)$$

$$\frac{1}{b^2 r^2}\left(w_1 b^2 r^2\right)_t + \frac{c}{3a^3 b}(w_0 a^4)_\mu + \frac{c}{br^3}(w_2 ar^3)_\mu - acs_1 = 0\,. \qquad (1.43)$$

In equations (1.42) and (1.43) w_0 and w_1 have the dimensions of energy density and cs_0 and cs_1 are in units of erg cm^{-3} s^{-1}.

1.2 BRIGHT LOW MASS X–RAY BINARIES

Already in 1965 Zel'dovich & Guseynov pointed out that X–rays emitted from single–line spectroscopic binaries would provide strong evidence for the presence of either a black hole or a neutron star. With the increasing precision of positional measurement of the X–ray telescopes, the positive identification of the optical counterparts and the periodicity inferred both by the line shift of the optical star and the periodic modulation of the X–ray flux, gave support to this idea and, at present, the theoretical models which best describe the observed phenomenology of X–ray binary sources are based on the transfer of mass through a stellar wind or an accretion disc from the companion component to the compact star. As can be seen in figure 1.1, where the position of the 339 sources detected by UHURU (The Fourth UHURU Catalogue, Forman *et al.* 1978), is shown in galactic coordinates, it is evident the existence of a population of relatively bright objects which are concentrated along the Galactic plane and whose optical counterparts (when identified) reside at distances ranging from 500 pc to 10 Kpc,
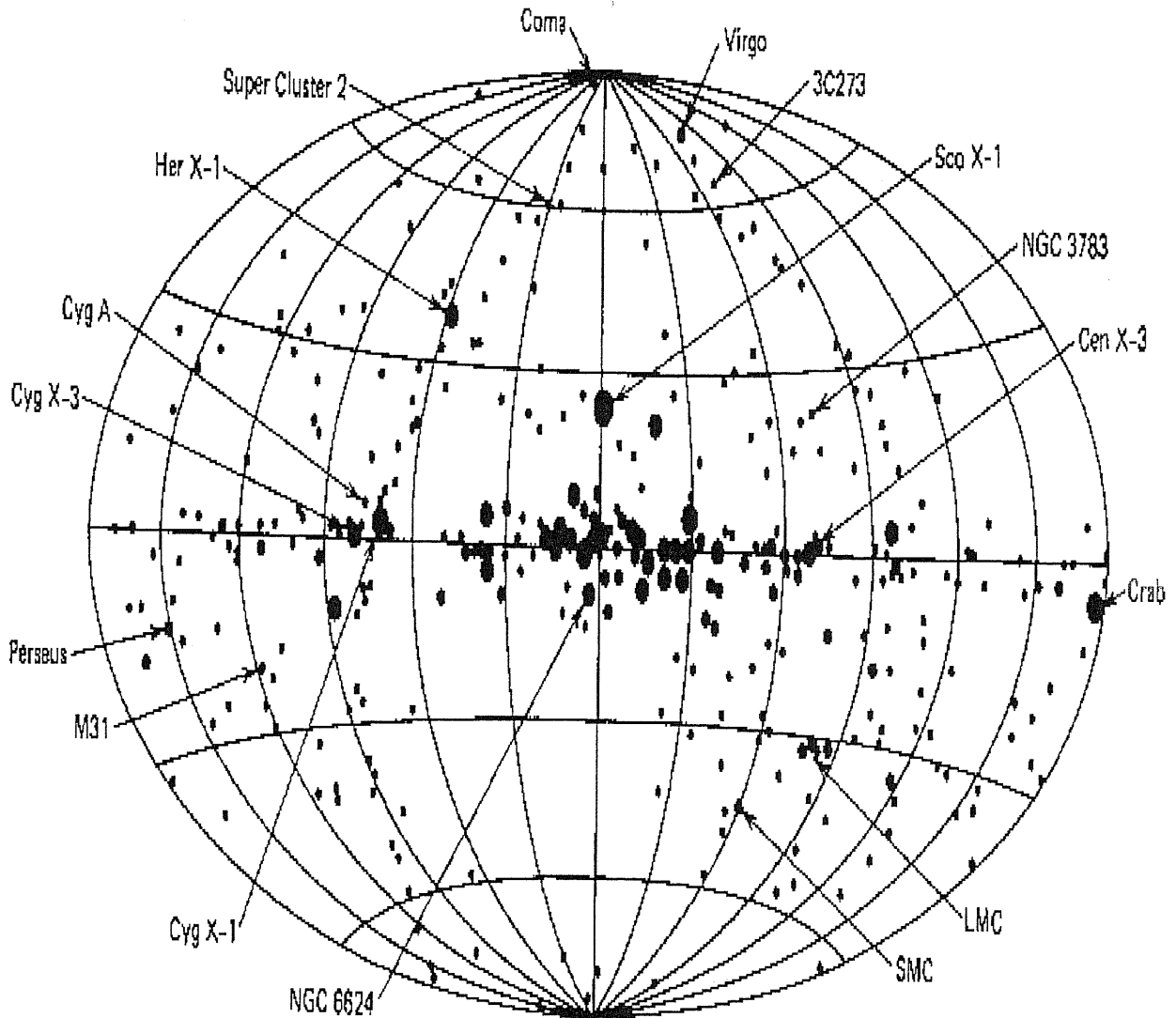
Figure 1.1 – The X–ray sources in Galactic coordinates reported in The Fourth UHURU Catalogue, Forman *et al.* (1978). The size of the symbols is proportional to the logarithm of the peak source intensity.

confirming their Galactic origin. Within this population of Galactic X–ray sources, a further distinction can be made on the basis of the spectral properties of the optical counterparts (Bradt & McClintock 1983): one group of sources is associated with O–B supergiants (High Mass X–ray Binaries, HMXBs), which are much more massive and younger than the stars of later spectral type associated with the second group of sources (Low Mass X–ray Binaries, LMXBs).
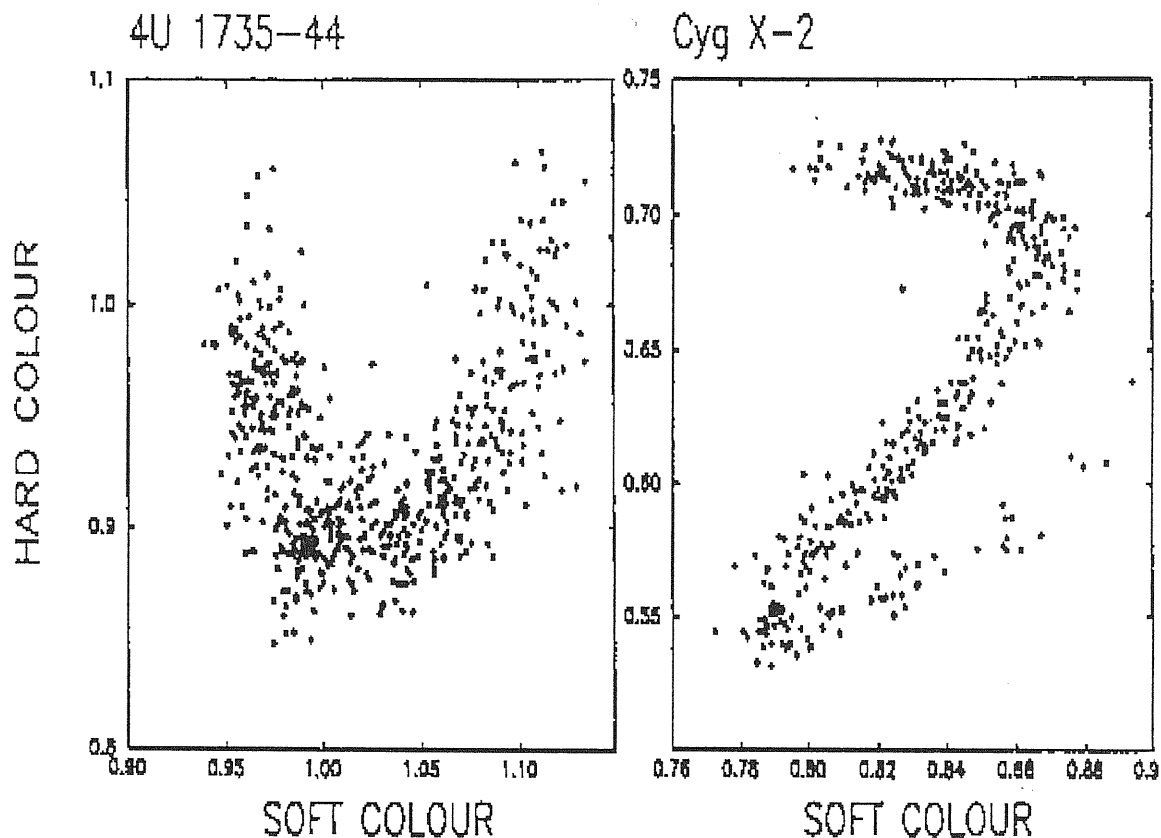
4U 1735-44   Cyg X-2

Figure 1.2 – The color–color diagram of an atoll (left; EXOSAT ME data on 4U 1735-44) and a Z (right; EXOSAT ME data on Cyg X–2) source (taken from van der Klis 1991).

The bright LMXBs, which have very high luminosities in the range 10^{37}–10^{38} erg s^{-1}, show very interesting observational properties as far as the emitted spectrum and the X–ray variability are concerned (for a review of the properties of X–ray binaries see e.g. White, Nagase & Parmar 1993). The spectrum of LMXBs is rather complex and is characterized by a decay in the flux above 6–10 keV, which contrasts with the substantially harder emission of X–ray pulsators; in some sources, however, a steep high energy tail (above 20 keV) is observed (see e.g. Maurer *et al.* 1982, Matt *et al.* 1990 and references therein). A good fit to the observed spectra is often obtained with the superposition of two components, like a a multitemperature black body disk plus a boundary layer black body (Mitsuda *et al.* 1984, 1989), or a boundary layer black

body plus an unsaturated comptonized disc component with the form of a power law (White, Peacock & Taylor 1985; White *et al.* 1986; White, Stella & Parmar 1988), or a comptonized spectrum (Ponman, Foster & Ross 1990; Lamb 1989, 1991). Often several different models fit the data (Vacca *et al.* 1987).

Bright LMXBs usually show variations in X–ray intensity and spectra on time–scales from several hours to days. These variations are commonly visualized in two types of diagrams, the hardness–intensity diagram and the color–color diagram. The "hardness ratios", also called "colors", are defined as the ratio of the count rates in two different spectral bands (after subtracting the background) and are a traditional way to characterize X–ray spectra which has been used since the early days in X–ray astronomy. In the color–color diagram, LMXBs are found in a rather narrow band of hardness ratios (Schulz, Hasinger & Trümper 1989). Although a positive correlation is often observed between the spectral hardness and intensity and in the color–color diagrams, inverse correlations ore multi–valued dependencies are also well documented (see figure 1.2). Along with the variations of the X–ray intensity on time–scales of hours to days, the flux of bright LMXBs undergo rapid variability on much shorter time–scales. The main diagnostic to study this high frequency variability is through the power spectrum (square modulus of the Fourier transform) of the X–ray signal. Studying the variation of the power spectrum with X–ray intensity in the EXOSAT data of the source GX 5-1, van der Klis *et al.* (1985) found that the source exhibited intensity– dependent, quasi–periodic oscillations between $\sim$ 20–40 Hz, appearing as a peak in the power spectrum. After this important discovery, quasi periodic oscillations (QPOs) were soon found in other bright LMXBs, such as Sco X–1 (Middleditch & Priedhorsky 1986) and Cyg X–2 (Hasinger *et al.* 1986). Since these sources were known at that time to be characterized by multivalued hardness–intensity and color–color diagrams, it was then quickly realized that the complicated patterns described on these diagrams could be related to their QPOs properties. This investigations culminated in the identification of two distinct "morphological classes" of bright LMXBs, the Z and atoll sources (Hasinger

1987; Hasinger & van der Klis 1989), whose names derive from the form of their typical tracks on the color–color diagrams.

The six objects which appear to belong to the class of Z sources show typical three-branched Z patterns on the hardness–intensity and color–color diagrams (see again figure 1.2), whose form depends on any individual source and, for each source, on the spectral bands used for the definitions of the colors. The three branches have been historically called horizontal branch (HB), normal branch (NB) and flaring branch (FB). As X-ray intensity varies on time–scales of hours to days, the source appears to move in a continuous but not periodic way along the three branches, never jumping from one to the other. This suggests that a single parameter can be used to establish a one–to–one correspondence between the position along the Z and the source state. Usually it is assumed that this parameter can be identified with the accretion rate (van der Klis 1989, 1991). The appearance of a peak in the power spectrum during the motion of the source along the color–color diagram marks the presence of horizontal branch QPOs (HB QPOs) and normal/flaring branch QPOs (NB/FB QPOs) with different centroid frequencies. Along with QPOs, various noise component are often detected in the X–ray signal of Z sources, which can differ along each branch.

The typical tracks of atoll sources in the color–color diagrams, shown in figure 1.2, exhibit an elongated, upwardly curved branch, called banana branch (BN), and two or more island zones, where the source do not move very much with time. The motion along the pattern is again regular without jumps, although not periodic. No QPOs are present in the power spectrum, which is dominated by noise components.

If the accretion of matter from the companion star is the source of energy of LMXBs, any plausible physical scenario must explain the spectral properties and the very complex patterns described by these sources on the hardness–intensity and color–color diagrams, along with the characteristic presence of quasi periodic oscillations of variable frequencies in relation with the position of the source on these diagrams. According to the model of Alpar & Shaham (1985) (see also Lamb *et al.* 1985), HB QPOs would

originate from the interaction of the neutron star magnetosphere with a Keplerian disc. This interaction would cause a modulation of the accretion rate at the beat frequency between the disc and the neutron star spin frequencies. NB/FB QPOs seem to be produced by a completely different mechanism, as suggested by Fortner, Lamb & Miller (1989) (see also Lamb 1989, 1991; Miller & Park 1995). Since Z sources have luminosities and accretion rates near the Eddington limit, in the inner part of the accretion disc the effects of radiation pressure should become important (see e.g. Shakura & Sunyaev 1973); the disc itself may be driven in a puffed–up state, originating an approximately radial accretion flow component. In these conditions, the flow can become overstable and start to oscillate at a frequency comparable with that observed for NB QPOs. A tentative interpretation of the Z/atoll classification (Hasinger & van der Klis 1989) suggest that Z sources have higher values of both the accretion rate and the neutron star magnetic field than those of atoll sources. The higher magnetic field explain why HB QPOs, which are likely to be a magnetospheric phenomenon, occur only in Z sources and the higher accretion rate can explain why NB/FB QPOs have only been observed in Z sources. The suppression of HB QPOs in this high accretion rate state would be caused by the "engulfing" of the magnetosphere by the inflated accretion disc. Such a qualitative picture is in accordance with the unified model of X–ray spectra and QPOs of bright LMXBs proposed by Lamb and collaborators (Fortner, Lamb & Miller 1989; Lamb 1989, 1991; Miller & Lamb 1992; Miller & Park 1995). According to this model, a weakly magnetized neutron star accretes gas simultaneously from a Keplerian disc fed by the companion star and a spherical corona produced by radiation pressure in the inner part of the disc. When the luminosity is comparatively low ($\sim 0.5 L_{Edd}$), unsaturated comptonization of soft photons in the hot (10-30 keV) central corona around the neutron star surface could produce the characteristic power law with high energy cutoff component observed in the HB of Z sources; the soft (~ 1 keV) black body component would be produced by saturated comptonization of photons from the inner disc and/or the neutron star magnetosphere and would increase with the increase of $\dot{M}$ along the

HB. According to the model by Alpar & Shaham (1985), the HB QPOs are caused by the interaction of the small magnetosphere with the inner disc. At luminosities $\gtrsim 0.9 L_{Edd}$, the radiation pressure in the disc drives some plasma into a more extended inner disk corona, which surrounds the hot central corona and cools to temperatures ~ 1 keV. Radiation drag causes the inner disc corona to lose its angular momentum and fall approximately radially toward the neutron star. The angular momentum conservation limits the radial mass flux to at most $\sim 30\%$ of the total mass flux. Then, the spectrum is modified as it passes through the cool, optically thick inner disc corona because of direct Compton effect. The hard part of the spectrum is progressively degradated as the optical depth increases and this would cause the characteristic decrease of the soft and hard colors observed along the NB of LMXBs. NB QPOs are attributed to overstable oscillations of the radial flow (Fortner, Lamb & Miller 1989; Miller & Lamb 1992; Miller & Park 1995). The spectral changes and FB QPOs along the flaring branch may be caused by complicated physical phenomena, such as photohydrodynamics modes which grow in amplitude as luminosity becomes $\gtrsim 0.9 L_{Edd}$.

Then, the observed phenomenology of Z sources appears to indicate that, at a certain stage, the accretion pattern can be regarded as approximately spherical because of the effects of radiation pressure. In addition, if these sources have low magnetic fields ($B \lesssim 10^9$ G), as it seems to be indicated by the absence in the spectrum of cyclotron absorption and/or emission lines, the radiative opacities are presumably not very affected and radiative transfer calculations neglecting the presence of magnetic fields can provide reasonable results. In these conditions, we argue that the spectral effects of dynamical comptonization produced by the bulk motion of a radial inflow of gas can be of importance in explaining the high energy tails of the spectra emitted by Z sources accreting near the Eddington limit. As it will be shown in Chapter 2, bulk motion comptonization is expected to become important in regions where the electron scattering optical depth τ is larger than unity and the infall velocity of the accretion flow v is such that $\tau v/c \sim 1$; owing to the large value of the accretion rate, both conditions turn

out to be satisfied for Z sources in the normal branch and then we expect dynamical comptonization to produce observable effects on their spectra.

1.3 OLD ISOLATED NEUTRON STARS

The discovery in 1967 of the first radio pulsar (Hewish *et al.* 1968) gave the first observational proof of the existence of neutron stars. Born from the supernova explosion which ends the life of massive stars, neutron stars are estimated to be as many as $\sim 10^9$ in our Galaxy, their actual number depending on the evolution of the supernova rate explosion during the past history of the Galaxy. If certain conditions are satisfied, at a certain stage of their life isolated neutron stars can undergo accretion from the surrounding interstellar gas and may show up as weak, soft X–ray sources, as firstly suggested by Ostriker, Rees & Silk (1970). For a star moving supersonically with velocity v relative to the interstellar gas, the amount of mass which is accreted per unit time is given by (Novikov & Thorne 1973)

$$\dot{M} = \pi r_c^2 \rho v \simeq 6 \times 10^9 \left(\frac{M_*}{M_\odot}\right)^2 \left(\frac{n}{1 \text{ cm}^{-3}}\right) \left(\frac{v}{40 \text{ Km s}^{-1}}\right)^{-3} \text{ g s}^{-1}, \qquad (1.44)$$

where $r_c = 2GM_*/v^2$ is the gravitational capture radius (M_* is the mass of the neutron star). As shown by equation (1.44), the supply of fuel to make lone neutron stars shining in the sky depends on the actual geography of the interstellar medium and on their velocity and position relative to it (these topics will be discussed in more detail in Chapter 3). However, in the first stages after their formation, isolated neutron stars are probably strongly magnetized and can emit intense electromagnetic dipole radiation in the radio band at the expense of their rotational energy. This low–frequency photons will produce a non–negligible radiation pressure on the surrounding medium which will inhibit any possible accretion of interstellar material until the neutron star slows down to periods of few seconds; for typical neutron star parameters and assuming a magnetic dipole model for the emission, this would require a characteristic time (Treves, Colpi &

Lipunov 1993)

$$t \simeq 5 \times 10^9 \left(\frac{r_*}{10^6 \text{ cm}}\right)^{-3} \left(\frac{M_*}{M_\odot}\right)^{-1} \left(\frac{B_i}{10^{12} \text{ G}}\right)^{-2} \left(\frac{B_f}{10^{12} \text{ G}}\right) \times$$

$$\times \left(\frac{n}{1 \text{ cm}^{-3}}\right)^{-1/2} \left(\frac{v}{40 \text{ Km s}^{-1}}\right) \text{ yr},$$

(1.45)

where r_* is the NS radius, B_i is the magnetic field at the surface of the NS at birth and B_f is the residual field strength. Then, for typical values of the density of the interstellar medium and of the velocity of the neutron star (see Chapter 3), t turns out to be close to the age of the Galaxy. However, if a decay of the magnetic field occurs, most of the isolated neutron stars are sufficiently old in order to start accretion from the interstellar medium. Once the flow penetrates the accretion radius, it will proceed unaffected until the Alfvèn radius is reached, where the magnetic pressure becomes equal to the ram pressure of the gas:

$$r_A = \frac{B^2 r_*^6}{\sqrt{2GM_* \dot{M}}} \simeq 4 \times 10^{10} \left(\frac{r_*}{10^6 \text{ cm}}\right)^{12/7} \left(\frac{M_*}{M_\odot}\right)^{-5/7} \times$$

$$\times \left(\frac{B}{10^{12} \text{ G}}\right)^{4/7} \left(\frac{n}{1 \text{ cm}^{-3}}\right)^{-2/7} \left(\frac{v}{40 \text{ Km s}^{-1}}\right)^{6/7} \text{ cm}.$$

(1.46)

At this point, matter is channeled along the magnetic field lines and accretion can be stopped if the centrifugal acceleration exerted on the matter flowing along the field lines is greater than the gravitational acceleration, i.e. when the angular velocity of rotation of the neutron star is larger than the Keplerian angular velocity at r_A. So, if the accretion rate decreases below the minimum value

$$\dot{M}_{min} \simeq 10^{18} \left(\frac{r_*}{10^6 \text{ cm}}\right)^6 \left(\frac{M_*}{M_\odot}\right)^{-5/3} \left(\frac{B}{10^{12} \text{ G}}\right)^2 \left(\frac{P}{1 \text{ s}}\right)^{-7/3} \text{ g s}^{-1},$$

(1.47)

where P is the neutron star spin period, accretion cannot proceed further on. Comparing equations (1.44) and (1.47), for the typical values of n and v expected for Old isolated Neutron Stars (ONSs) accreting from the interstellar medium, accretion turns out to be possible for a relic field $B \sim 10^9$ G and periods of the order of a few seconds. Observations of pulsars (Lyne, Manchester & Taylor 1985; Bhattacharya *et al.* 1992)

seem to suggest a decay of the magnetic field of neutron stars over a time $\sim 10^7$ yr or longer. However, evidence for a long lived component $(10^9$–10^{10} G), comes from the observations of old accreting neutron stars in binaries and millisecond pulsars (Kulkarni 1986). Then, for isolated ONSs, fields of 10^6, 10^9 or 10^{12} G can be equally plausible. If the magnetic field is large, the accreted material may be temporarily stopped and, under these circumstances, the accretion process may be cyclic with recurrence time of 10^6 s (Treves, Colpi & Lipunov 1993). For this reason in the following we will consider a magnetic field $B = 10^9$ G, which ensures that accretion takes place and is essentially steady.

Since $\dot{M}$ is very small, the accreting plasma is likely to be channeled along the magnetic field lines onto the polar caps (for $B \sim 10^9$ G $r_* \ll r_A$). Then, the energy of the infalling matter will be released mainly when the accretion flow impinges the neutron star surface near the magnetic poles. The details of the flow braking are rather different according to the mechanisms which are effective in stopping the flow. If binary Coulomb collisions between the infalling ions and the atmospheric electrons dominate, as it is expected at very low values of $\dot{M}$, the accretion flow can be stopped at several Thomson depths and the resulting spectrum can be thermalized at a temperature approximately equal to the star effective temperature (see Zel'dovich & Shakura 1969; see also Alme & Wilson 1973)

$$T_{eff} = \left(\frac{L}{4\pi r_*^2 f_s \sigma}\right)^{1/4} \simeq 90 \left(\frac{f_s}{10^{-3}}\right)^{-1/4} \left(\frac{r_*}{10^6 \text{ cm}}\right)^{-3/4} \left(\frac{M_*}{M_\odot}\right)^{3/4} \times$$
$$\times \left(\frac{n}{1 \text{ cm}^{-3}}\right)^{1/4} \left(\frac{v}{40 \text{ Km s}^{-1}}\right)^{-3/4} \text{ eV} , \tag{1.48}$$

where $L = GM_*\dot{M}/r_*$ and f_s is the fraction of the surface area which undergoes accretion. Then, ONSs emit typically in the ultraviolet and soft X–ray bands. On the other hand, although its actual occurrence has not yet been proved at low accretion rates, the appearance of plasma instabilities can lead to the formation of a shock above the neutron star surface and, at the shock front, a large fraction of the kinetic energy of the incoming matter can be thermalized at very high temperatures. In this case the

emission of copious hard X–ray or γ–ray fluxes are expected (Shapiro & Salpeter 1975). Finally, cooling curves (Nomoto & Tsuruta 1987) show that the surface temperature of a NS will drop below 20 eV in a characteristic time $\sim 10^6$ yr and then the emission from the cooling of the interior can be certainly neglected after as much as 10^9 yr.

All of the previous investigations have been limited to computing the spectrum at relatively high values of the accretion rate, which are certainly not relevant for ONSs accreting from the interstellar medium. A thorough investigation of the emitted spectrum turns out to be certainly a key ingredient in order to correctly address the issue of detecting these sources, since the choice of the energy bands where to look for and the absorption of the interstellar medium are strongly related to the ONSs emission properties and in particular to the actual shape of their spectrum. In addition, if the magnetic field is sufficiently low ($B \lesssim 10^9$ G) its effects on the radiative opacities are presumably not very important and radiative transfer calculations without considering the presence of magnetic fields can provide reasonable results. For these reasons, we decided to carry out a detailed investigation of the transfer of radiation in the atmosphere of a neutron star accreting at low rates assuming that the stopping of the incoming flow is due mainly to binary Coulomb collisions. Although our radiative transfer calculations has been performed in spherically symmetric, we argue that they can be assumed still valid in presence of low magnetic fields and polar cap accretion, provided that the effects of the reduced emitting area are taken into account. This will clearly produce a hardening of the emitted spectrum since all of the accretion energy is released in a comparatively smaller area. The results of this study and their application to the detectability of ONSs will be presented in Chapter 3.

CHAPTER 2
DYNAMICAL COMPTONIZATION
IN SPHERICAL FLOWS

In the second section of this chapter we will re–investigate the effects of bulk acceleration of photons in radially inflowing atmospheres within the framework of the moment equations. We will solve analytically these equations in two different ways: the first method (separation of variables) follows closely the classical approach by Payne & Blandford (1981), whereas the second, which exploits the technique of the Fourier transforms, will be presented for the first time here. We will re-cover all of the main properties of dynamical comptonization in spherical flows, namely the drift of the centroid toward high frequencies and the formation of a high energy tail with a well defined spectral index. This method will allow us to work out also an analytical solution for radial spherical outflows, whose properties are somewhat reversed with respect to those of inflows: shift toward low frequencies and formation of a low frequency, power law tail. To get more insight, we present also a detailed study of dynamical comptonization from the microphysical point of view and, starting from these results, we discuss the limit of validity of the present approach.

In the second part of this chapter, we will investigate the role of bulk acceleration of photons in connection with the formation of the spectrum in neutron stars accreting near the Eddington limit. As it will be analyzed in section 2.3, the physical conditions encountered in the inner part of the accretion flow seem to be favourable in order for bulk heating of photons to be of importance. A thorough numerical investigation of the deformation of the spectrum induced by dynamical comptonization shows that, at near Eddington luminosities, a power law, high energy tail with spectral index ~ 3 (count rate) can form above 10 keV. The flow dynamics and the transfer of radiation are self–consistently solved for a spherically symmetric, "cold" scattering flow, including General Relativity. The possible relevance of these numerical results in connection with the observed spectral properties of Z sources, and Cygnus X–2 in particular, is discussed.

2.1 INTRODUCTION

In the scattering against an electron at rest a photon will lose energy according to the Compton formula. However, if the electron is moving, it can transfer part of its kinetic energy to the photon; such an effect is called inverse Compton. In certain situations, the effects of comptonization of photons by electrons in thermal motion in a static medium can be of primary importance in modifying the spectral distribution of the radiation field. In general, the transfer of photons through a relativistic electron gas is governed by the Boltzmann equation in which the interaction term contains the Klein–Nishina cross section averaged over a relativistic Maxwellian distribution (Pomraning 1973; Kershaw, Prasad & Beason 1986; Kershaw 1987). Because of its complicated structure, a number of authors have attempted to model this equation by a diffusion equation (Fokker–Planck approximation). In particular, Kompaneets (1957) first derived a diffusion equation valid for non–relativistic electrons and small photon energies. Katz (1976) extended the Kompaneets work to the study of photon diffusion through a finite homogeneous isothermal plasma (see also Sunyaev & Titarchuk 1980) and found that, for moderate optical thickness, the emergent spectrum shows a power law, high energy tail, whose index depends on the electron temperature and the optical depth. Finally, Prasad *et al.* (1988) and Shestakov, Kershaw & Prasad (1988) obtained an analytic expression for the diffusion coefficient of the Fokker–Planck equation which describes correctly comptonization for arbitrary values of the photon energy and electron temperature.

All of the previous studies concentrated on the effects of thermal comptonization of photons by electrons in thermal motion in a static medium. However, to the same extent, also bulk ordered motion of the electrons could affect the photon distribution in phase–space. Already in 1978, Rees (1978) and Begelman (1978) showed that, if radiation is propagating through a medium which is accreting onto a black hole and in which the optical depth is sufficiently large, at a certain radius the inward flow velocity can become equal to the outward diffusion velocity of the photons and radiation is effectively trapped

into the accreting gas. However, they did not consider the extent and consequences of dynamics on the spectrum of photons. The first systematic investigation of the effects induced by the bulk motion of the gas on the radiation field (dynamical comptonization) has been presented by Blandford & Payne (1981a,b) and Payne & Blandford (1981). They derived the transfer (Boltzmann) equation for a gas moving at non–relativistic velocities in flat space–time. In the static limit they re–obtain the Kompaneets equation for a finite medium. Particularizing their equation to an accreting spherical inflow and neglecting thermal comptonization, they were able to evaluate quantitatively the effects of photon trapping solving the equation by separation of variables. If photons are emitted near the trapping radius, they undergo a lot of scatterings and most of them are dragged inward, resulting in a severe decrease of the outward flux. Photons cannot escape easily but, if they do, they gain significant amount of energy from collisions with the inflowing electrons. Then, because of the work done by the radial inflow on the escaping photons, the emergent spectrum shows both a drift to high frequencies and the formation of a high energy tail whose index depends on the velocity profile. We note that this effect is similar to Fermi acceleration of cosmic rays and has been independently discussed within the framework of the acceleration of charged particles, photons and neutrinos also by other authors (see e.g. Schneider & Bogdan 1989 and references therein). However, if the thermal velocity of the flow cannot be neglected in comparison with that of the ordered motion, the combined effects of bulk heating and ordinary thermal comptonization need to be considered. This problem was fully investigated by Colpi (1988), which presented an analytical solution of the transfer equation for an isothermal spherical inflow in which velocity is proportional to free–fall and induced scattering and free–free absorption are neglected. The effects of the bulk acceleration of photons modify in two ways the thermal spectrum: first through an overall decrease of the emitted flux, second washing out the Wien peak and producing again a power law whose index depends on the ratio between the Compton and the infall time–scales. Finally, the effects of dynamical comptonization in accretion onto neutron

stars were investigated analytically by Mastichiadis & Kylafis (1992), which found that, in the case of near critical accretion, the emergent spectrum is much flatter than for black hole accretion.

One of the most promising astrophysical environments in which bulk heating of photons might have a significant role is the inner part of the spherical accretion flow onto neutron stars radiating near the Eddington limit. In this case, the drag exerted on the accretion flow by the radiation pressure is so effective that the gas decelerates and a settling regime is established above the neutron star surface, as found by Maraschi, Reina & Treves (1978). Stationary spherical near–critical accretion onto neutron stars has been studied also by Miller (1990) and, including General Relativity, by Park & Miller (1991), who obtained very similar results. The density near the star surface becomes sufficiently high that radiation interacts strongly with the inflowing gas and, even in the absence of emission processes, the emergent spectrum can be modified by dynamical comptonization due to bulk motion.

2.2 DYNAMICAL COMPTONIZATION

In this section we will present the solution of the first two frequency–dependent moment equations for a spherical inflow/outflow of matter in which the only effective interaction between gas and radiation is due to Thomson scattering and the optical depth is everywhere greater than one. This problem was fully investigated by Payne and Blandford (1981) for a converging fluid flow. They solved the transfer equation within the same assumptions and found that, provided certain conditions are satisfied, the flow can strongly modify the initial spectral distribution of photons through comptonization due to bulk gas motion: the emerging spectrum shows a distinctive power law, high energy tail with a spectral index dependent on the velocity gradient. In the following we will reconsider this problem within the framework of moment equations. We will obtain an analytical solution for the radiative flux and will show that dynamical comptonization can be effective in modifying the spectral shape of the radiation field also in optically

thick spherical outflows.

Let's consider for the moment a spherical inflow in which the velocity profile is assumed to be a power law (we neglect thermal motion and assume v positive for inward motion):

$$v = v_{in} \left(\frac{r}{r_{in}} \right)^{\beta} , \qquad (2.1)$$

where r_{in} is the inner radius and $v_{in} = v(r_{in})$. In order to make the analytical treatment possible, in analogy with Payne & Blandford, we switch off gravity setting

$$y = \frac{1}{\sqrt{1 - (v/c)^2}} ,$$

$$\frac{d \ln y}{d \ln r} = \frac{(v/c)^2}{1 - (v/c)^2} \frac{d \ln v}{d \ln r} ,$$

so that, to first order in v/c, $y = 1$ and $d \ln y / d \ln r = 0$. With these assumptions, from the continuity equation (equation (1.22)) it follows immediately that the density can be written as

$$\rho = \rho_{in} \left(\frac{r}{r_{in}} \right)^{-(2+\beta)} . \qquad (2.2)$$

Using equation (2.2) the electron scattering optical depth between r and ∞ turns out to be:

$$\tau = \int_r^{\infty} k_{es} \rho dr = \frac{k_{es} \rho r}{1 + \beta} \propto r^{-(1+\beta)} , \qquad (2.3)$$

which implies that $\beta > -1$ for the optical depth to decrease with increasing radius.

Now we assume that the diffusion approximation holds ($\tau \gg 1$). In this case it is known that $W_1/W_0 = O[1/\tau]$, $W_2/W_0 = O[(v/c + 1/\tau)/\tau]$ and $W_3/W_0 = O[(v/c + 1/\tau)/\tau^2]$ (see Thorne, Flammang & Żytkow 1981). Retaining all terms of order 1, $1/\tau$ and v/c in the moment equations (1.24) and (1.25) and putting $S_0 = 0$ and $S_1 = -k_{es} \rho W_1$ (see equations (1.26) and (1.27) where only Thomson scattering is considered), we obtain

$$\frac{\partial W_1}{\partial \ln t} - \frac{v}{c} \frac{\partial W_0}{\partial \ln t} - 2W_1 + (2 + \beta) \frac{v}{c} \left(W_0 - \frac{1}{3} \frac{\partial W_0}{\partial \ln \nu} \right) = 0 , \qquad (2.4)$$

$$\frac{\partial W_0}{\partial \ln t} - 3(1 + \beta)\tau W_1 = 0 , \qquad (2.5)$$

where $k_{es}\rho r$ has been rewritten as $(1+\beta)\tau$ (see equation (2.3)) and we have introduced the new variable

$$t = 3(1+\beta)\tau\frac{v}{c} \propto r^{-1}\,,\tag{2.6}$$

$$\frac{\partial}{\partial \ln r} = -\frac{\partial}{\partial \ln t}\,.$$

Dividing equation (2.4) by v/c, taking the derivative with respect to $\ln t$ and eliminating $\partial W_0/\partial \ln t$, $\partial^2 W_0/\partial \ln t^2$ and $\partial^2 W_0/\partial \ln t \partial \ln \nu$ by means of equation (2.5), we obtain, after some manipulation, a single second order partial differential equation for the flux W_1

$$t\frac{\partial^2 W_1}{\partial t^2} + (\beta - 1 - t)\frac{\partial W_1}{\partial t} + \left(1 - \frac{2\beta}{t}\right)W_1 - \frac{2+\beta}{3}\frac{\partial W_1}{\partial \ln \nu} = 0\,,\tag{2.7}$$

which, introducing the new variable $u_1 = W_1 t^{-2}$, can be recast in the form

$$t\frac{\partial^2 u_1}{\partial t^2} + (3 + \beta - t)\frac{\partial u_1}{\partial t} - u_1 - \frac{2+\beta}{3}\frac{\partial u_1}{\partial \ln \nu} = 0\,.\tag{2.8}$$

Following Payne & Blandford, the solution of equation (2.8) can be found by separation of variables: writing $u_1 = \phi(t)\nu^{-p}$, equation (2.8) becomes a confluent hypergeometric equation for ϕ which can be solved once suitable regularity conditions are imposed as $t \to 0$ and $t \to \infty$. Asking that the photon number flux becomes a constant for $t \to 0$ and that the adiabatic compression of photons is recovered for $t \to \infty$, the regular solution turns out to be the superposition of eigenfunctions corresponding to the discrete spectrum of eigenvalues $(p_n; n = 0, ..., \infty)$ of the confluent hypergeometric equation (see Abramowitz & Stegun 1970). Then, W_1 can be written as a superposition of modes, each one of the form ν^{-p_n} with $p_n = 3(n+1)/(2+\beta)$, as found by Payne and Blandford:

$$W_1 = t^2 \sum_{n=0}^{\infty} A_n L_n(t)\nu^{-3(n+1)/(2+\beta)}\tag{2.9}$$

where $L_n(t)$ are the Laguerre polynomials of order n and A_n are constants to be fixed by the boundary condition. For $\beta = -1/2$ and $n = 0$, $p_0 = 2$, so the spectrum at high enough frequencies is expected to be a power law with spectral index 2 in the free–fall case.

In the following we will consider an alternative approach to the solution of equation (2.8) which exploits the technique of the Fourier transform and allows to select automatically the well-behaved solutions. This method will provide us an easier way of handling the regularity conditions which will be particularly useful in the case of spherical outflows. We will start again from equation (2.8) which is a Fokker–Planck equation and can be written in the form

$$\frac{\partial^2 (tu_1)}{\partial t^2} - \frac{\partial}{\partial t}\left[(t - 1 - \beta)u_1\right] = \frac{\partial u_1}{\partial z}, \tag{2.10}$$

where $z = 3\ln\nu/(2 + \beta)$. Fourier transforming equation (2.10) with respect to t, we obtain

$$ik(1 - ik)\frac{\partial \tilde{u}_1}{\partial ik} - \frac{\partial \tilde{u}_1}{\partial z} = -(1 + \beta)ik\tilde{u}_1, \tag{2.11}$$

where $\tilde{u}_1$ is the Fourier transform of u_1 and is given by

$$\tilde{u}_1(k, z) = \frac{1}{2\pi}\int_{-\infty}^{+\infty} e^{-ikt}u_1(t,\nu)dt. \tag{2.12}$$

This method has the advantage of reducing the order of the partial differential equation which becomes of first order in the k–space and can be solved using standard techniques once a boundary condition is imposed. A monochromatic flux of photons of frequency ν_0 is put into the flow at a given t_0:

$$u_1(t,\nu) = A(\nu)\delta(t - t_0) \qquad \nu = \nu_0, \tag{2.13}$$

which can be Fourier transformed to give

$$\tilde{u}_1(k, z) = A(z)e^{-ikt_0} \qquad z = z_0 = 1. \tag{2.14}$$

The solution of equation (2.11) with the boundary condition (2.14) is

$$\tilde{u}_1 = A(z_0)\left[ik\left(e^{z-z_0} - 1\right) + 1\right]^{1+\beta}\exp\left[-\frac{ikt_0 e^{z-z_0}}{ik(e^{z-z_0} - 1) + 1}\right]. \tag{2.15}$$

Applying the inverse transformation to equation (2.15), we finally get the solution of equation (2.10) (see Appendix A, equation (A5))

$$u_1 = A(\nu_0)\frac{\xi^{-\beta/2}}{1-\xi}\left(\frac{t_0}{t}\right)^{(2+\beta)/2}\exp\left(-\frac{\xi t + t_0}{1-\xi}\right)I_{2+\beta}\left[2\frac{(\xi t t_0)^{1/2}}{1-\xi}\right],\qquad(2.16)$$

where $\xi = (\nu_0/\nu)^{3/(2+\beta)}$ and $I_{2+\beta}$ is the modified Bessel function of order $2 + \beta$. Taking the limit $t \to 0$ in equation (2.16) and recalling that

$$I_{2+\beta}(\psi) \simeq \frac{1}{\Gamma(3+\beta)}\left(\frac{\psi}{2}\right)^{2+\beta}\qquad \psi \to 0,\qquad(2.17)$$

where $\Gamma(3 + \beta)$ is the Γ–function, the radiative flux turns out to be

$$W_1 = t^2 u_1 = \frac{A(\nu_0)}{\Gamma(3+\beta)}\frac{\xi}{(1-\xi)^{3+\beta}}t^2 t_0^{2+\beta}\exp\left(-\frac{t_0}{1-\xi}\right)\qquad t \to 0.\qquad(2.18)$$

At high frequencies ($\nu \gg \nu_0$, $\xi \ll 1$) we recover the asymptotic dependence on frequency given by equation (2.9)

$$W_1 \propto \xi = \left(\frac{\nu}{\nu_0}\right)^{-3/(2+\beta)}\qquad t \to 0,\ \nu \gg \nu_0.\qquad(2.19)$$

We emphasize that the main advantage of this method is that the Fourier transform automatically selects the well–behaved regular solutions which are Lebesgue integrable and then does not require any regularity condition to be imposed. This fact is particularly advantageous for spherical outflows for which the handling of such conditions is not so straightforward. For this reason here we will repeat the calculation for spherical outflows using the Fourier transform method and will not consider further on the approach which exploits the separation of variables. Taking now v positive for outward motion, assuming that diffusion holds and combining together the first two moment equations, we get

$$t\frac{\partial^2 W_1}{\partial t^2} + (\beta - 1 + t)\frac{\partial W_1}{\partial t} - \left(1 + \frac{2\beta}{t}\right)W_1 + \frac{2+\beta}{3}\frac{\partial W_1}{\partial \ln\nu} = 0,\qquad(2.20)$$

which, introducing the new variable $u_1 = W_1 t^{-2}$ and after some manipulation, can be recast in the form

$$\frac{\partial^2(t u_1)}{\partial t^2} + \frac{\partial}{\partial t}\left[(t + 1 + \beta)u_1\right] = \frac{\partial u_1}{\partial \bar{z}},\qquad(2.21)$$

where $\bar{z} = -3 \ln \nu / (2 + \beta)$. In strict analogy to what has been done previously, the solution of equation (2.21) is obtained imposing the boundary condition (2.13), Fourier transforming and applying the inverse transformation, which yields

$$u_1 = A(\nu_0) \frac{\xi^{-\beta/2}}{\xi - 1} \left(\frac{t_0}{t} \right)^{(2+\beta)/2} \exp \left(-\frac{\xi t + t_0}{\xi - 1} \right) I_{2+\beta} \left[2 \frac{(\xi t t_0)^{1/2}}{\xi - 1} \right] . \qquad (2.22)$$

Taking again the limit $t \to 0$ and considering frequencies $\nu \ll \nu_0$ ($\xi \gg 1$), we get for the radiative flux

$$W_1 = t^2 u_1 = \frac{A(\nu_0)}{\Gamma(3 + \beta)} \frac{\xi}{(\xi - 1)^{3+\beta}} t^2 t_0^{2+\beta} \exp \left(-\frac{t_0}{\xi - 1} \right)$$

$$\propto \xi^{-(2+\beta)} = \left(\frac{\nu}{\nu_0} \right)^3 \qquad t \to 0, \ \nu \ll \nu_0 . \qquad (2.23)$$

irrespectively to β. Then, dynamical comptonization in spherical outflows tends to modify the input spectral shape producing a power law, low energy tail whose index is independent of the shape of the velocity profile.

The results presented in this section have been derived imposing as boundary condition a monochromatic photon input. However, since equations (2.10) and (2.21) are linear, for more complex input spectra, the solution can be obtained as a superposition over ν_0 of equation (2.16) or equation (2.22), the weighting function $A(\nu_0)$ representing the input spectral shape:

$$W_1 = t^2 \int_0^\infty u_1(t, \nu; \nu_0) d\nu_0 . \qquad (2.24)$$

The fact that equation (2.7) (equation (2.20)) can be re-written as a Fokker–Planck equation says that dynamical comptonization can be described essentially as a diffusion process in frequency, which has three basic features: convection, diffusion and the production of a power law spectrum. This process causes not only the distortion but also an overall shift in frequency of the input spectral shape. As can be seen from figures 2.1 and 2.2, where the emergent ($t \to 0$) flux is shown for different injection radii (t_0), the peak of the spectrum shifts toward high frequencies for spherical inflows and toward

Figure 2.1 – Emergent ($t \rightarrow 0$) spectrum for a radial converging flow ($u_1 = t^{-2}W_1$; see equation (2.18)). Here $\beta = -1/2$ (free–fall) and $t_0 = 1/3$ (dash–dotted line), 1 (dashed line), 3 (continuous line).

low frequencies for outflows. In addition, the distortion and the drift of the spectrum is clearly present only if $t_0 \sim 1$, that is to say only if radiation passes through a region where it is effectively trapped into the flow. It is interesting to note that, if $2 + \beta = 0$, the diffusion term in equation (2.7) (equation (2.20)) disappears and any input spectrum will be unaffected. As shown by equation (2.2), this is possible only for a constant density flow: in fact, although photons are convected (transported outward) by the gas, in this case no compression (decompression) is exerted by the inflowing (outflowing) medium on the radiation field and no energy is transferred to it through compressional work.

2.2.1 Microphysics of Dynamical Comptonization

More insight on the results presented in the previous section can be obtained considering bulk motion comptonization from the microphysical point of view. If electrons are moving with velocity v, the photon energy ϵ, as seen by the observer at rest, will change
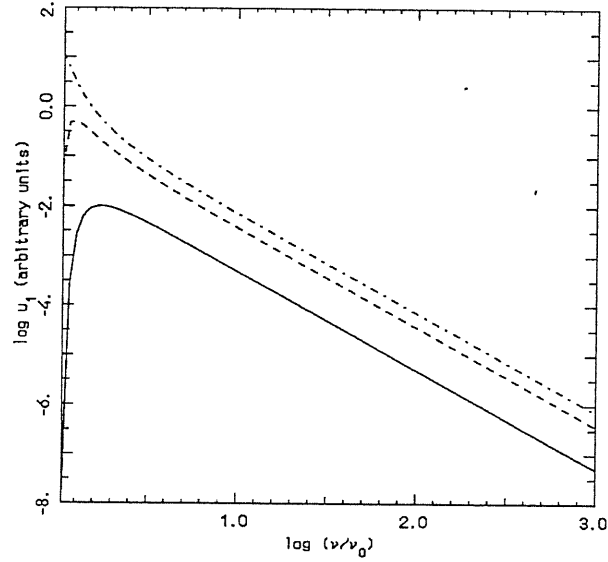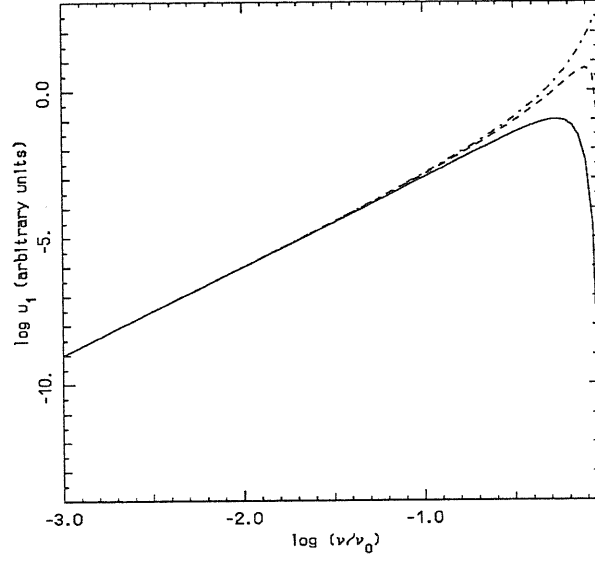
Figure 2.2 – Emergent $(t \rightarrow 0)$ spectrum for a radial outflow $(u_1 = t^{-2}W_1$; see equation (2.23)). Here $\beta = 1$ and $t_0 = 1/3$ (dash–dotted line), 1 (dashed line), 3 (continuous line).

in the scattering process. The Doppler shift transformations for the photon energy from the observer frame K to the electron rest frame K' are

$$\epsilon' = \epsilon\gamma \left(1 - \frac{v}{c}\cos\theta\right) , \qquad (2.25)$$

$$\epsilon_1' = \epsilon_1\gamma \left(1 - \frac{v}{c}\cos\theta_1\right) , \qquad (2.26)$$

while the inverse transformations from K' to K are

$$\epsilon = \epsilon'\gamma \left(1 + \frac{v}{c}\cos\theta'\right) , \qquad (2.27)$$

$$\epsilon_1 = \epsilon_1'\gamma \left(1 + \frac{v}{c}\cos\theta_1'\right) , \qquad (2.28)$$

where ϵ_1 is the photon energy after the scattering, θ (θ_1) is the angle between the incident (outgoing) photon and the electron velocity and a prime denotes quantities evaluated in the electron rest frame. If, in this frame, the scattering is conservative and isotropic, we have

$$\epsilon_1' = \epsilon' , \qquad (2.29)$$

$$\langle \epsilon_1 \rangle_{\Omega_1'} = \epsilon_1' \gamma = \epsilon' \gamma \,. \tag{2.30}$$

Equation (2.30) has been calculated from equation (2.28) averaging over all outgoing photons directions Ω_1' in the electron rest frame. Now, in the observer frame K the mean energy change per scattering is given by (see also Rybicki and Lightman 1979)

$$\langle \Delta\epsilon \rangle_{\Omega_1'} = \langle \epsilon_1 \rangle_{\Omega_1'} - \epsilon = [\gamma^2 (1 - (v/c)\cos\theta) - 1]\,\epsilon \,. \tag{2.31}$$

If the radiation field is isotropic in K, equation (2.31) yields the well–known result for the mean energy change

$$\langle\langle \Delta\epsilon \rangle\rangle_{\Omega_1'\Omega} = \gamma^2 (v/c)^2 \epsilon \,. \tag{2.32}$$

In the diffusion limit, however, photons are not isotropic and, in the electron rest frame, the radiation field has an angular distribution

$$f(\theta') = 1 + \frac{\cos\theta'}{\tau} \,. \tag{2.33}$$

Transforming to the observer frame (equation (2.27)) and averaging upon θ', one gets for the mean energy change the expression (Nobili, Turolla & Zampieri 1993)

$$\langle\langle \Delta\epsilon \rangle\rangle_{\Omega_1'\Omega'} = -\frac{v/c}{v/c + 3\tau}\langle \epsilon \rangle_{\Omega'} \simeq -\frac{v/c}{\tau}\langle \epsilon \rangle_{\Omega'} \,, \tag{2.34}$$

which is positive or negative according to the sign of v. Since photons produced in a region where $\tau \gg 1$ undergo N_s scatterings before escaping to infinity, the total energy variation is $\sim N_s\langle\langle \Delta\epsilon \rangle\rangle_{\Omega_1'\Omega'}/\langle \epsilon \rangle_{\Omega'}$. The number of scatterings for photons diffusing through a moving medium is $\sim T/t_s$ where $t_s \sim L/(c\tau)$ is the scattering time–scale, $T \sim L/v_d$ is the total travel time, L is the characteristic dimension of the region and $v_d = c/\tau + v$ is the diffusion velocity as measured in the observer frame. N_s is given then by

$$N_s \sim \frac{\tau^2}{1 + (v/c)\tau} \tag{2.35}$$

and the total fractional energy change turns out to be

$$N_s\frac{\langle\langle \Delta\epsilon \rangle\rangle_{\Omega_1'\Omega'}}{\langle \epsilon \rangle_{\Omega'}} \sim -\frac{(v/c)\tau}{1 + (v/c)\tau} \,. \tag{2.36}$$

When v is negative, as in accretion flows, N_s diverges when $(v/c)\tau \to -1$, just implying that in our approximate treatment photons produced at or below the trapping radius never reach infinity being advected inward by the matter flow. For $(v/c)\tau \approx -1$, the total fractional energy gain is typically of order unity. On the contrary no trapping radius exists for outgoing flows, $v > 0$, and the total energy variation, which is now negative, approaches -1 for large values of $(v/c)\tau$.

This simple argument shows that the energy of the emergent photons may be substantially different from their initial energy if τ is large enough even if $v/c \ll 1$. Dynamics is therefore expected to have non negligible effects on the observed radiation spectrum whenever photons are produced in a region where $|v/c|\tau \sim 1$. This result is due to the fact that, in the electron rest frame, the photon energy is unchanged during the scattering process. This amounts to saying that the electron has effectively infinite mass and does not experience any recoil in K'. It can absorb the momentum change of the photon without modifying its velocity. For the observer K, photons which bounce against the electron will gain energy if they move toward it and will lose energy if they move in the same direction. The process is similar to the reflection of particles against a moving mirror, although it is complicated by the presence of aberration and Doppler effects. The net energy gained (lost) in the observer frame K by a certain angular distribution of incident photons is supplied (absorbed) by the infinite reservoir of kinetic energy of the electron. The ultimate source of energy is the external field which has accelerated the electron to the velocity v.

Then, the effectiveness of the process is essentially related to the possibility of neglecting the recoil of the electron. However, if the energy of the incident photon in K' is not small with respect to the rest mass of the electron, it is no more possible to neglect the recoil since the photon will lose energy in the scattering process according to the Compton formula

$$\epsilon_1' = \frac{\epsilon'}{1 + \epsilon'(1 - \cos\Theta)/mc^2}, \tag{2.37}$$

where $\cos\Theta = \cos\theta_1' \cos\theta' + \sin\theta_1' \sin\theta' \cos(\varphi' - \varphi_1')$ is the cosine of the angle between

the incident and the outgoing photons measured in the rest frame (φ' and φ_1' are the azimuthal angles of the incident and scattered photons) and m is the electron mass. If $\epsilon' \ll mc^2$, we can write

$$\epsilon_1' \simeq \epsilon' \left[1 - \frac{\epsilon'}{mc^2}(1 - \cos\Theta) \right] . \tag{2.38}$$

Inserting equation (2.38) into equation (2.28), averaging (2.27) and (2.28) over the angular distribution (2.33) and over all of the outgoing photon directions in K', we get

$$\langle\langle\epsilon_1\rangle\rangle_{\Omega_1'\Omega'} = \gamma\epsilon' \left[1 - \frac{\epsilon'}{mc^2} \left(1 - \frac{v/c}{9\tau} \right) \right] , \tag{2.39}$$

$$\langle\epsilon\rangle_{\Omega'} = \gamma\epsilon' \left(1 + \frac{v/c}{3\tau} \right) . \tag{2.40}$$

Then, the mean energy change is given by

$$\langle\langle\Delta\epsilon\rangle\rangle_{\Omega_1'\Omega'} = -\frac{v/c + \epsilon'(3\tau - v/3c)/mc^2}{v/c + 3\tau} \langle\epsilon\rangle_{\Omega'} . \tag{2.41}$$

Comparing equation (2.34) with equation (2.41), if the photon energy becomes relatively large, it is not possible to neglect the recoil of the electron and, even for an inflowing atmosphere ($v < 0$), high energy photons can lose more energy through ordinary Compton effect than what they gain through bulk motion comptonization. This energy will be turned into electron thermal energy. This effect is particularly important when the optical depth is very large, so that photons will undergo a lot of scatterings before escaping to infinity. Although dynamical comptonization tends to increase the mean photon energy in each scattering, when ϵ' increases this process can be stopped by the fact that the recoil term $\epsilon'(3\tau - v/3c)/mc^2$ in equation (2.41) becomes important. Then, a significant amount of energy can be transferred to electrons and the ordinary thermal comptonization cannot be neglected. If $\tau \gg 1$, it is easy to see that the condition for heating or cooling due to the bulk motion to overcome the electron recoil can be written as follows

$$\frac{\epsilon'}{mc^2} \lesssim \frac{(v/c)^2}{3\tau |v|/c} . \tag{2.42}$$

Since $3\tau(v/c)$ must be of order unity for dynamical comptonization to be effective, equation (2.42) says simply that the kinetic energy per unit mass of the ordered motion of the electron must be greater than the energy of the incident photon measured in the electron rest frame. Whenever this equation is not satisfied, it is no longer possible to neglect the electron recoil and a more generalized treatment of the transfer of radiation including thermal comptonization has to be considered.

We note also that, in the present analysis, the velocity of the electron could originate partly from its thermal motion. Although we are not interested here to make a detailed calculation, in this case an additional term would appear in equation (2.41) which accounts for the thermal motion and would be proportional to the mean thermal velocity $\langle v_{th} \rangle \sim (KT/m)^{1/2}$, where T is the electron temperature. Then, as shown by Blandford & Payne (1981a), if $(12KT/m)^{1/2} \geq v$ the ordinary inverse Compton effect will dominate and a detailed treatment of the transfer of radiation has necessarily to include thermal along with bulk motion comptonization (see e.g. Colpi 1988).

2.3 NEAR CRITICAL ACCRETION ONTO NEUTRON STARS

In this section we will study the effects of bulk acceleration of photons on the spectrum emitted at the surface of a non–rotating, unmagnetized neutron star which undergoes spherical accretion at near critical rates. We assume that X–ray radiation is generated by the conversion of gravitational potential energy, as matter is accreted onto the neutron star. If the flow velocity vanishes at the neutron star surface, the efficiency of the accretion process is given by the variation of the specific gravitational energy E_p

$$\eta_{eff} = (E_p)_\infty - (E_p)_* = 1 - \left(\sqrt{-g_{00}}\right)_* = 1 - \sqrt{1 - \frac{2GM_*}{c^2 r_*}} \sim \frac{GM_*}{c^2 r_*}, \qquad (2.43)$$

where M_* and r_* denote the neutron star mass and radius, respectively, and we used vacuum Schwarzschild solution to describe the gravitational field outside the star. By introducing the adimensional radial coordinate $x = r/r_g$, $r_g = 2GM_*/c^2$, and the

accretion rate $\dot{M}$, the total luminosity observed at infinity is

$$L_\infty = \eta_{eff}\dot{M}c^2 = \left(1 - \sqrt{1 - \frac{1}{x_*}}\right)\dot{M}c^2 .\qquad (2.44)$$

The complete analysis of a steady–state, spherically symmetric gas flow onto a compact star is a complex task since the appearance of shocks and/or of a boundary layer at the neutron star surface should be expected. However, some reasonable simplifying assumptions can be made if one is not interested in treating in detail the inner accretion layer where nearly all the energy is released. First of all we note that $\eta_{eff} \sim 0.1$ for $M_* \sim 1.4M_\odot$ and $r_* \sim 10$ km, so that $L_\infty/L_{Edd} = l_\infty \sim 1$ if $\dot{M}/\dot{M}_{Edd} = \dot{m} \sim 1$, where $L_{Edd} = 4\pi GM_*c/k_{es}$ is the Eddington luminosity and $\dot{M}_{Edd} = L_{Edd}/c^2$ is the critical accretion rate. By comparing this value for l_∞ with the maximal luminosity attainable in black hole accretion, $l_{bh} \lesssim 0.01$ (see Nobili, Turolla & Zampieri 1991), it follows that the infalling gas can radiate, at most, a few percent of the total energy output before the impact with the surface of the star. We can therefore safely neglect emission processes in the accreting gas and treat the material as a pure scattering medium. In this hypothesis the radiation spectrum observed at infinity is formed in the boundary layer by processes which are not important to specify in detail since the overall spectral properties are determined mainly by scatterings as radiation propagates outward. The main goal of our investigation is to study the effects of dynamics on radiative transfer and therefore we consider only coherent (Thomson) scattering. We make the further assumption that the plasma is "cold", in the sense that its enthalpy is always much less than effective gravity. This is equivalent to say that the the gas velocity is everywhere greater than the sound speed and limits the validity of our approach to the supersonic part of the flow.

The equations governing the dynamics of the matter gas and the transfer of radiation in spherical, stationary accretion in a Schwarzschild gravitational field have been presented in Chapter 1 (equations (1.20)–(1.22), (1.28) and (1.29)). In the case of a "cold" ($T = 0$, $P = 0$, $e = \rho c^2$), pure scattering ($s_0 = 0$, $s_1 = -k_{es}\rho w_1$) plasma they

reduce to the form (here the velocity v is assumed positive for inward motion)

$$\frac{v^2}{c^2}\frac{(yv)'}{yv} = -\frac{1}{2y^2 x} + \frac{k_{es}xr_g}{yc^2}w_1 , \tag{2.45}$$

$$2k_{es}r_g x^2 \rho \left(\frac{v}{c}\right) y = \dot{m} , \tag{2.46}$$

$$w_1' - \frac{v}{c}w_0' + 2w_1\left(1+\frac{y'}{y}\right) - \frac{v}{c}w_0\left[f\left(\frac{(yv)'}{yv}-1\right) + \frac{4}{3}\left(\frac{(yv)'}{yv}+2\right)\right] = 0 , \tag{2.47}$$

$$\left(f+\frac{1}{3}\right)w_0' - \frac{v}{c}w_1' + \left[f' + f\left(3+\frac{y'}{y}\right) + \frac{4}{3}\frac{y'}{y}\right]w_0 -$$

$$- 2\frac{v}{c}w_1\left[\frac{(yv)'}{yv}+1\right] = -\frac{k_{es}\rho x r_g w_1}{y} . \tag{2.48}$$

The comoving luminosity L is related to w_1 by $L = 4\pi x^2 r_g^2 c w_1$. To close the system, we have introduced the variable Eddington factor, $f = w_2/w_0$, where w_2 is the radial moment of second order of the specific intensity. In the following we assume that f is a given function of the optical depth τ of the form

$$f(\tau) = \frac{2}{3(1+\tau^2)} . \tag{2.49}$$

The fact that dynamical effects on radiative transfer are going to be relevant in the present model, can be easily shown. As discussed in the previous section, bulk motion comptonization is expected to become important in regions where $\tau > 1$ and $\tau v/c \sim 1$. Using equations (2.44) and (2.46), neglecting relativistic corrections and assuming $\tau \sim k_{es}\rho x r_g$, we have that

$$(\tau v/c)_* \sim \frac{\dot{m}}{2x_*} \sim l_\infty , \tag{2.50}$$

which shows that close to the star surface $\tau v/c$ is indeed not far from unity for near critical accretion.

To compute the emitted spectrum, we need to solve the first two frequency–dependent moment equations for a pure scattering flow (see again Chapter 1, equations (1.24) and (1.25) with $v > 0$ inward)

$$\frac{\partial W_1}{\partial \ln x} + 2W_1 + \frac{d\ln y}{d\ln x}\left(W_1 - \frac{\partial W_1}{\partial \ln \nu}\right) -$$
$$-\frac{v}{c}\left\{\frac{\partial W_0}{\partial \ln x} + (\beta + 2)W_0 - \left[f(\beta - 1) + \frac{1}{3}(\beta + 2)\right]\frac{\partial W_0}{\partial \ln \nu}\right\} = 0, \qquad (2.51)$$

$$\left(f + \frac{1}{3}\right)\frac{\partial W_0}{\partial \ln x} + f\left(3 + \frac{d\ln f}{d\ln x}\right)W_0 +$$
$$+\frac{d\ln y}{d\ln x}\left[W_0 - \left(f + \frac{1}{3}\right)\frac{\partial W_0}{\partial \ln \nu}\right] - \frac{v}{c}\left[\frac{\partial W_1}{\partial \ln x} + \frac{1}{5}(7\beta + 8)W_1 - \frac{1}{5}(3\beta + 2)\frac{\partial W_1}{\partial \ln \nu}\right] -$$
$$-g(\beta - 1)\left(W_1 + \frac{\partial W_1}{\partial \ln \nu}\right) = -\frac{k_{es}\rho x r_g W_1}{y}, \qquad (2.52)$$

where W_0 and W_1 are the frequency–dependent moments and $\beta = d\ln(yv)/d\ln x$. In writing equations (2.51) and (2.52) we have assumed that the Eddington factors $f = W_2/W_0$ and $g = W_3/W_1$, where W_2 and W_3 are the higher order moments which enter equations (1.24) and (1.25), are independent of frequency: f is given again by equation (2.49) and $g = 3f/5$.

The solution of equations (2.45)–(2.48) provides the velocity and density profiles of the matter gas and the radial evolution of the frequency–integrated moments, once boundary conditions are given. In treating a pure scattering problem one of the conditions must fix the value of either the radiation energy density or of the flux at some radius. Computed models were obtained assigning the value of the luminosity far from the star (l_∞). Since M_* and r_* are known, equation (2.44) gives immediately the accretion rate, while the two remaining boundary conditions are

$$w_0 = w_1 \qquad x = x_{out} \qquad \text{(radial streaming)} \qquad (2.53)$$

and

$$\frac{v}{c} = \sqrt{\frac{1 - l_\infty}{x}} \qquad x = x_{out} \qquad \text{("modified" free fall)}. \qquad (2.54)$$

It should be noted that l_∞ is the only free parameter of the model. Equations (2.51) and (2.52) have to be solved as a two points boundary value problem in space and an initial value problem in frequency. In our particular case, we have assigned the flux spectral distribution at the star surface

$$W_1(x_*, \nu) = F(\nu),\qquad\qquad(2.55)$$

with the additional constraint that

$$\int_0^\infty F(\nu)\,d\nu = w_1(x_*),\qquad\qquad(2.56)$$

where $w_1(x_*)$ is the frequency–integrated flux at x_*, as given by the solution of equations (2.45)–(2.48); the remaining radial condition is again

$$W_0 = W_1 \qquad x = x_{out} \qquad \text{(radial streaming)}.\qquad(2.57)$$

In the case of an unmagnetized neutron star accreting close to the Eddington limit, as we are considering here, we assume that photons are generated only at the surface, through some convenient mechanism that could convert the kinetic energy of the infalling gas into radiation with a given spectral distribution. The simplest choice that can be made is that the input spectrum is Planckian in shape

$$W_1(x_*, \nu) = A\,\frac{(h\nu/KT_*)^3}{\exp(h\nu/KT_*) - 1},\qquad\qquad(2.58)$$

where the temperature $T_* = T(x_*)$ is fixed by the condition

$$T_* = \left(\frac{L_\infty}{4\pi r_*^2 \sigma}\right)^{1/4}.\qquad\qquad(2.59)$$

This expression for T_* is justified if the effective optical depth in the flow is always smaller than unity, as indeed should be the case in all our models. The constant A appearing in equation (2.58) is determined by normalization (2.56). Two different sets of frequency boundary conditions have been used in the calculations, according to the

value of l_∞ which characterizes the model. For models with luminosity $l_\infty \lesssim 0.4$ the spectrum drifts toward low frequencies because gravitational redshift dominates over dynamical comptonization (see the following discussion), so that both conditions must be specified at the largest frequency mesh point ν_{max}

$$\frac{\partial \ln W_0}{\partial \ln \nu} = \frac{\partial \ln W_1}{\partial \ln \nu} \qquad \nu = \nu_{max} , \tag{2.60}$$

$$\frac{\partial \ln W_0}{\partial \ln \nu} = 3 - \frac{h\nu}{KT_*} \qquad \nu = \nu_{max} \quad \text{(Wien law)}. \tag{2.61}$$

The situation is reversed for models with luminosity $l_\infty \gtrsim 0.4$ and the previous conditions are replaced by

$$\frac{\partial \ln W_0}{\partial \ln \nu} = \frac{\partial \ln W_1}{\partial \ln \nu} \qquad \nu = \nu_{min} , \tag{2.62}$$

$$\frac{\partial \ln W_0}{\partial \ln \nu} = 2 \qquad \nu = \nu_{min} \quad \text{(Rayleigh–Jeans law)}. \tag{2.63}$$

Conditions (2.61) and (2.63) express the fact that W_0 must remain black body in shape at high (low) frequencies while (2.60) and (2.62) derive from the request that $W_1 \propto W_0$ in a pure scattering medium. A discussion on how frequency conditions should be placed in solving the transfer problem in moving media can be found in Mihalas, Kunasz & Hummer (1976), Nobili, Turolla & Zampieri (1993) and Turolla, Zampieri & Nobili (1995). Numerical integrations show that in a small luminosity range around $l_\infty = 0.4$ both sets of boundary conditions work satisfactorily.

The self–consistent velocity and density profiles obtained from the simultaneous integration of the hydrodynamical and frequency–integrated moment equations has been used in equations (2.51) and (2.52) to compute the emitted spectrum. Once a solution has been obtained, we compared the integral of W_1 with the corresponding solution for the frequency–integrated flux w_1 and found that the fractional error was always less than few percent. This ensures that the computed velocity and density profiles are consistent with the solution of the frequency–dependent moment equations.
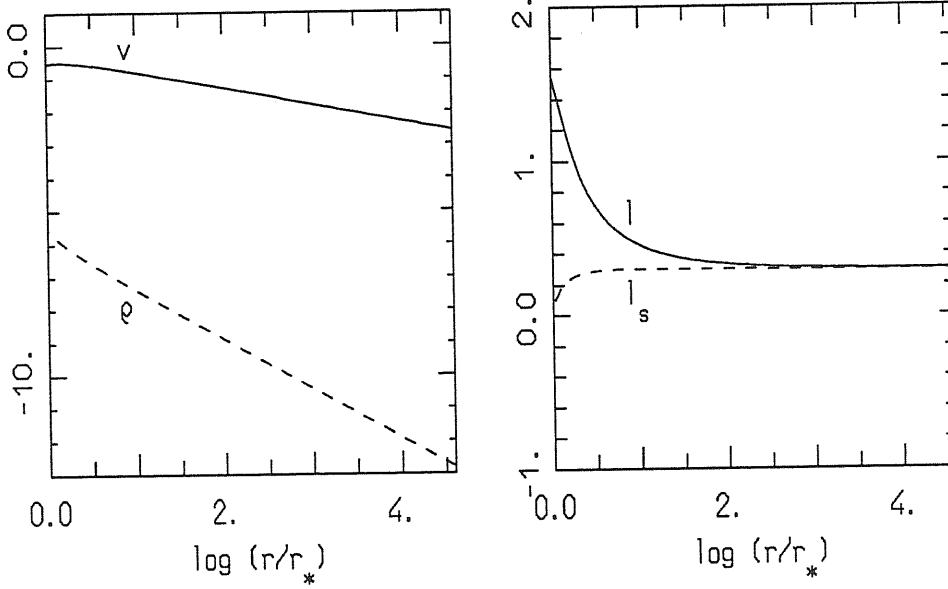
Figure 2.3 – Velocity v, density ρ, stationary $l_s = l_\infty[1 + (y - 1)/\eta_{eff}]/(1 - 1/x)$ and comoving l luminosities versus radius for the model with $l_\infty = 0.3$. Scales are logarithmic and density is in g cm^{-3}.

2.3.1 Numerical Results

The results of numerical integrations of equations (2.45)–(2.48) are shown in figures 2.3 and 2.4, for two representative values of l_∞, $l_\infty = 0.3$ and $l_\infty = 0.9$ respectively; in all models $M_* = 1.4\ M_\odot$ and $r_* = 10^6$ cm. The settling regime is a common feature of all high luminosity solutions and is clearly visible in figure 2.4. The overall behaviour of our models is close to that one found by Maraschi, Reina & Treves (1978), Miller (1990) and Park & Miller (1991) under quite similar assumptions. In order to simulate the effects of a disc component, we have computed also another model with $l_\infty = 0.9$ but with a mass flux reduced of about 70%. In fact, as discussed in Chapter 1, within the framework of the unified model of Low Mass X–ray Binaries (Lamb 1989, 1991) the angular momentum conservation limits the radial mass flux to at most $\sim 30\%$ of the total mass flux. In these assumptions, a significant fraction of the mass flux is contained
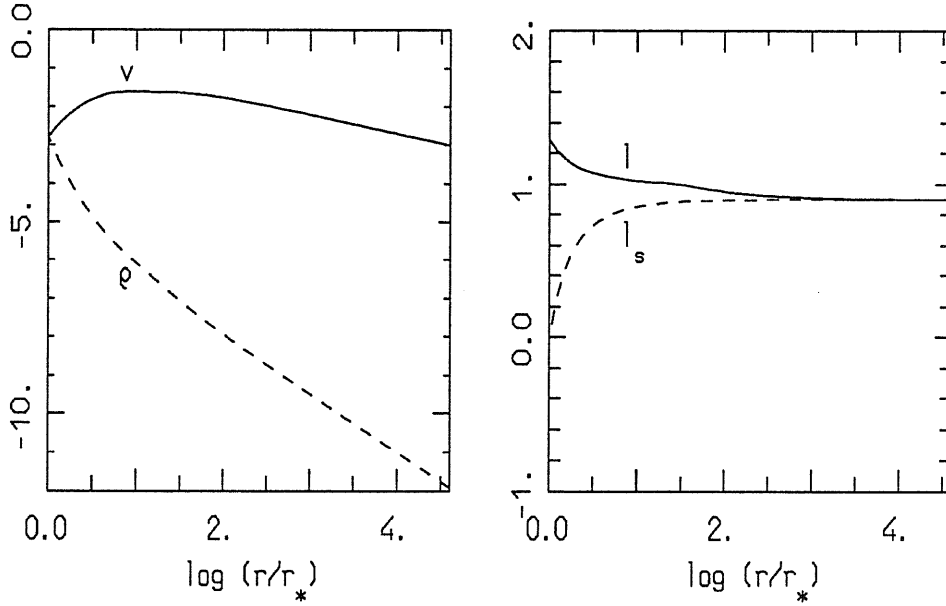
Figure 2.4 – The same as in figure 2.3 for the model with $l_\infty = 0.9$.

within the accretion disc and a corresponding fraction of the radiative luminosity (l_*) is released in the inner part of the disc near the star surface. Then, the total luminosity observed at infinity will be the sum of two contributions, the first coming from the disc (l_*) and the second produced by the radial accretion flow $(\eta_{eff}\dot{m}_r)$

$$l_\infty = l_* + \eta_{eff}\dot{m}_r , \qquad (2.64)$$

where $\dot{m}_r = 0.3\dot{m}$ (see Park & Miller (1991) for a discussion of a radial distributed source of photons in the disc). The results of this calculation are shown in figure 2.5. Although the density at the outer boundary is smaller, the deceleration of the flow becomes more precipitous (see again Park & Miller 1991) and in the inner region ρ increases above the value of the model with the mass flux entirely within the spherical component. As a consequence, the optical depth at the star surface is larger and $(\tau v/c)_*$ is still sufficiently large in order dynamical comptonization to be of importance (see table 2.1).

The integration of equations (2.51) and (2.52) has been performed using an original
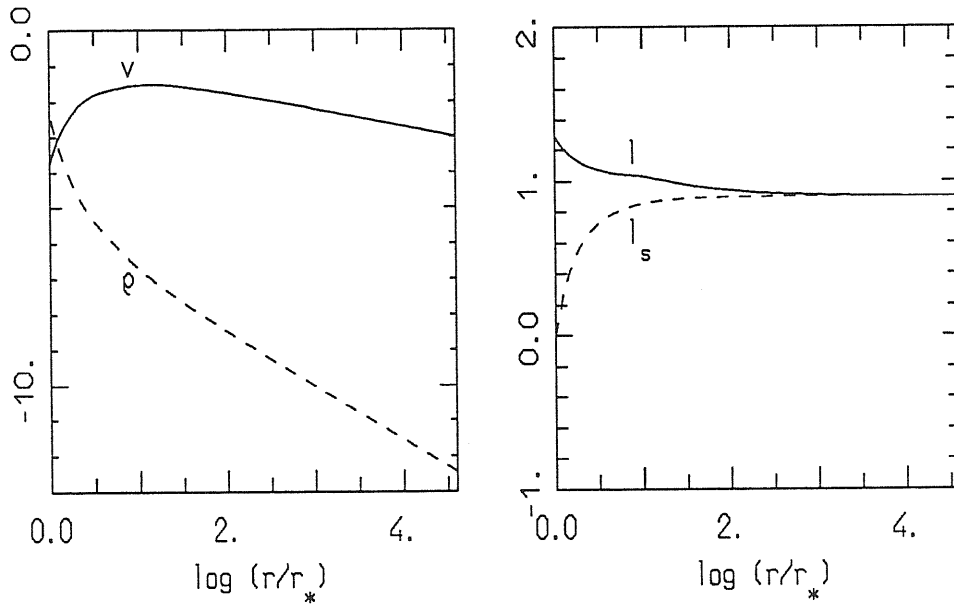
Figure 2.5 – The same as in figure 2.3 for the model with $l_\infty = 0.9$ and $\dot{m}_r = 0.3\dot{m}$.

numerical code based on a relaxation method (for a detailed presentation see Nobili, Turolla & Zampieri 1993). A 30 frequency bins × 60 radial zones grid was used with $0.4 < \log x < 5$ and $-0.5 < \ln(h\nu/KT_*) < 1.2$. Some representative spectra are shown in figures 2.6 and 2.7 and results are summarized in table 2.1, where the "soft" and "hard" colors of the emergent spectrum are quoted together with the count rate in the 1–17 keV energy band; the last column gives the value of the photon spectral index if a power–law tail forms at high energies. The number flux was computed assuming a distance of 8 kpc for the source. Owing to the fact that $3(\tau v/c)_*$ is sufficiently large, the spectrum of the model with the reduced radial mass flux does not show significant quantitative differences with respect to the spectrum shown in figure 2.7. For this reason, since we are interested mainly in the spectral properties of the solutions, we will not distinguish further between models with $l_\infty = 0.9$ and different radial accretion rates.

Table 2.1 – Characteristic Parameters for Selected Models

l_∞	τ_*^{a}	$(\tau v/c)_*$	$\dfrac{(3\text{–}6)}{(1\text{–}3)}^{\text{b}}$	$\dfrac{(6\text{–}17)}{(3\text{–}6)}^{\text{c}}$	count rate[d]	α^{e}
0.1	0.3	0.17	0.17	0.02	0.40	-
0.2	0.7	0.31	0.31	0.06	0.73	-
0.3	1.3	0.37	0.40	0.09	0.96	-
0.4	2.2	0.38	0.68	0.20	1.00	-
0.5	4.0	0.38	1.06	0.49	0.87	-
0.6	7.1	0.39	1.28	0.70	0.86	-
0.7	14	0.38	1.44	0.98	0.82	-
0.8	33	0.34	1.63	1.23	0.79	3.3
0.9	1.8×10^2	0.30	1.79	1.53	0.75	3.4
0.9^{f}	2.1×10^2	0.05	1.75	1.46	0.76	3.4
0.95	1.2×10^3	0.28	1.87	1.69	0.72	3.5

[a] electron scattering optical depth at the star surface.

[b] "soft" color: N_{3-6}/N_{1-3}, where N is the photon count rate in the specified energy range.

[c] "hard" color: N_{6-17}/N_{3-6}.

[d] count rate: N_{1-17} (arbitrary units).

[e] photon spectral index: $-\partial \ln N_\nu / \partial \ln \nu$, calculated above 20 keV.

[f] model with the reduced mass flux $\dot{m}_r = 0.3\dot{m}$.

As can be clearly seen from the figures, the behaviour of the emergent spectrum changes significantly around $l_\infty = 0.4$. For $l_\infty \lesssim 0.4$, in fact, the flow becomes optically thin to scattering and, although $(\tau v/c)_* \sim 0.3$, bulk motion comptonization has little effect, because the probability for a photon to scatter before escaping to infinity becomes very low. The fact that $(\tau v/c)_*$ is not far from unity means that the typical fractional energy change per scattering is still large but electron–photon collisions are so few that the total energy exchange is negligible. Consequently the spectrum at infinity remains nearly Planckian but is rigidly shifted to the red (see figure 2.6) by the effect of gravity. As l_∞ is increased beyond 0.4, models start to develop a thick core, $(\tau v/c)_*$ remains
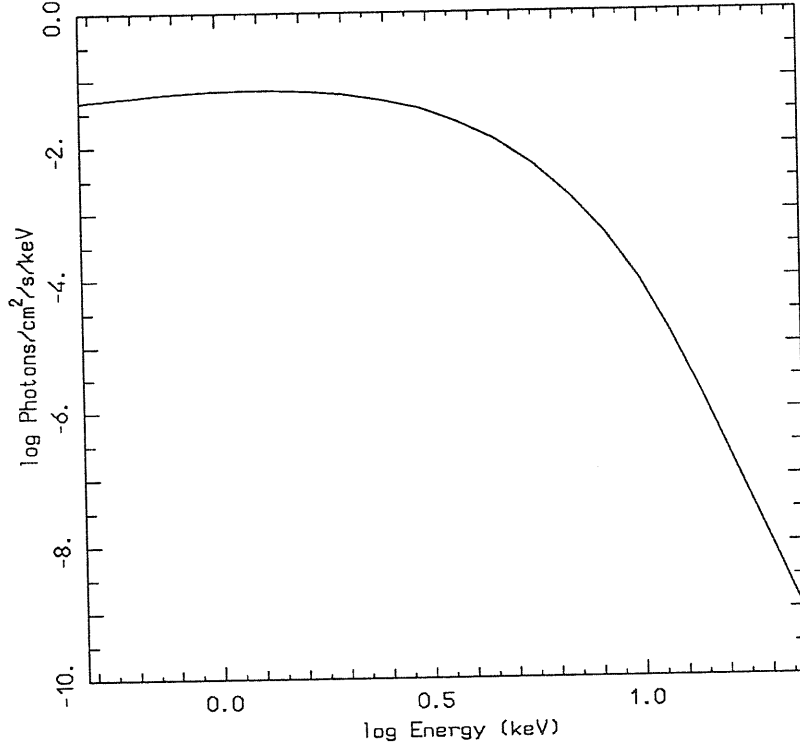
Figure 2.6 – Number flux spectral distribution for the model with $l_\infty = 0.3$. The source is assumed to be at a distance of 8 Kpc.

fairly constant because v_* decreases and τ_* increases, but now dynamical comptonization is important owing to the larger optical depth near the stellar surface. The emergent spectrum is systematically shifted to the blue and a power–law, high–energy tail forms. The dynamical blueshift roughly compensates the gravitational redshift just at $l_\infty \sim 0.4$. A typical dynamically Comptonized spectrum is shown in figure 2.7 for $l_\infty = 0.9$. The spectral shape is essentially Planckian up to energies ~ 10 keV and then becomes a power law with spectral index $\alpha \simeq 3.4$.

We wish to stress that low and high luminosity models have different spectral properties because the former are everywhere optically thin (or at most marginally thick) while the latter do have an optically thick inner region. The fact that $(\tau v/c)_*$ is more or less the same for all the solutions does not contradict the previous statement. In fact,
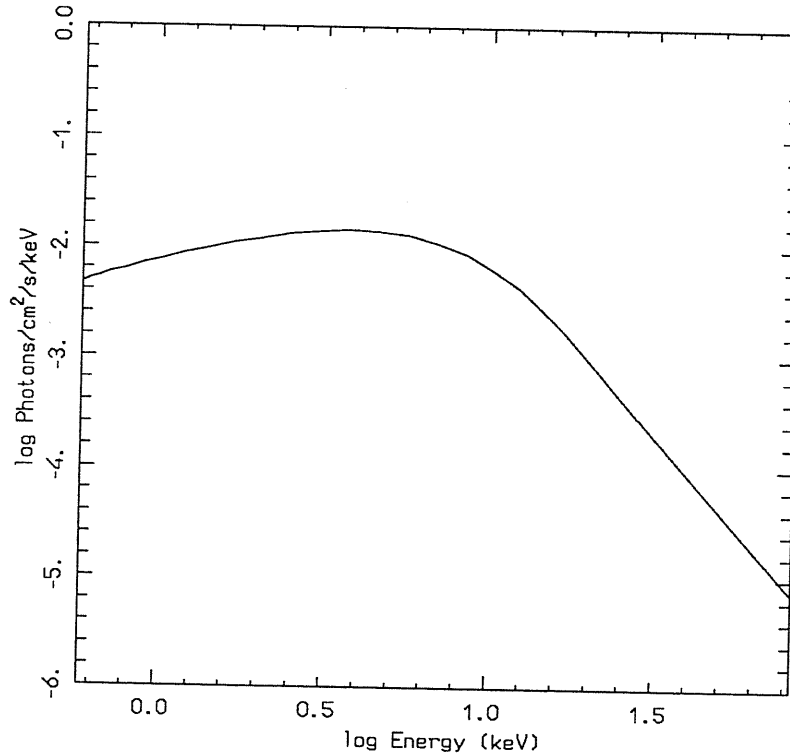
Figure 2.7 – The same as in figure 2.6 for the model with $l_\infty = 0.9$.

from the analysis presented in section 2.2 it follows that $\tau v/c$ is the important parameter for dynamical comptonization, but it should be taken into account that results were obtained in the diffusion limit, that is to say in the hypothesis of very large scattering depth. For optically thin flows the approach presented in section 2.2 does not apply at all and one has to expect the emergent spectrum to show different features. However, when $l_\infty \gtrsim 0.4$, the optical depth becomes larger than unity and spectra originating from near critical accretion onto neutron stars closely resemble those obtained by Payne & Blandford (1981, PB) for spherical accretion onto black holes, showing both a drift toward high frequencies and the formation of a power–law, high–energy tail. Mastichiadis & Kylafis (1992, MK) extended PB's analysis to an accreting flow onto a neutron star. They performed essentially PB's calculations, but replaced the original boundary con-

dition with the requirement that the flux vanishes at the star surface and proved that now the spectral index $\alpha = 1$, irrespective of the value of the velocity gradient. While the overall spectral evolution is quite similar in both cases, some important points, as the value of the final power–law index, seem to depend on the choice of the condition for the radiation field at the inner boundary. This particular aspect deserves a further comment in order to understand how our numerical solutions relate to these analytical results. While PB asked for adiabatic compression of photons as $t \propto \tau v/c \propto r^{-1} \to \infty$, MK used a different condition (vanishing flux) at $r = r_*$ where their integration domain terminates with a finite value of t. Although the input spectrum is a monochromatic line in both cases, the two conditions at the basis of the flow produce two distinct sets of eigenvalues (p_n) and this explains the different form of the emergent spectrum at high frequencies ($\alpha = p_0$ for $\nu \gg \nu_0$). As far as our model is concerned, the integration domain is finite, as in the MK case, so that PB's analysis certainly does not apply; our approach, however differs also from that of MK, because in fixing the input spectrum at r_*, we have assigned a different inner boundary condition. So, in this situation we do not know the analytical solution and the corresponding set of eigenvalues. Indeed, the emergent spectrum shows, a well–defined power–law tail whose index is related to the physical conditions in the region where dynamical effects become important.

In concluding we note that, although present results refer to the radial evolution of a Planckian, the global properties of the model (drift to high frequencies and formation of a power law tail) are largely independent of the form chosen for the input spectrum.

2.3.2 Comparison with spectral observations of Cygnus X–2

As discussed in Chapter 1, the results presented in this chapter can be relevant in connection with the observed spectral properties of Z sources. If the neutron star has a low magnetic field ($B \lesssim 10^8$–10^9 G), as it is believed for Low Mass X–ray Binaries (LMXBs), the radiative opacities and the flow dynamics may be practically unaffected

by its presence. In addition, within the framework of the unified model for LMXBs (Lamb 1989, 1991), at luminosities near the Eddington limit the pressure of radiation escaping from the inner disc drives some plasma into an extended disc corona. This plasma loses its angular and vertical momentum because of radiation drag and falls approximately radially toward the star (Fortner, Lamb & Miller 1989). The spectral properties and the time variability of Z sources seem to be well accounted for by this model (Miller & Lamb 1992; Miller & Park 1995; Psaltis, Lamb & Miller 1995). In this spirit, the results which we have presented in this section may be tentatively compared with the observed spectrum of Z sources and, in particular, of Cygnus X–2 which represents one of the prototypes of this class.

In comparing our synthetic spectra with actual observations one should keep in mind the drastic simplifications of this model. We have considered a unique component, a dynamically Comptonized black body, and in treating radiative transfer we have neglected all emission–absorption processes so that, for instance, line features do not appear. Also, we did not consider such complicated issues as the effects of unsaturated thermal comptonization in the hot central corona which, according to the unified model, should be presented around the neutron star surface and should account for the typical spectral shapes observed in bright LMXBs at moderate luminosities ($\sim 0.5 L_{Edd}$). Then, although a good fit to the spectral data obviously requires the superposition of various physical regions, each emitting a rather complex spectrum, it seems of interest to investigate simple models, physically well defined, which can shed light on some aspects of the formation of the spectrum and be part of the overall picture.

In order to be specific we shall deal with the EXOSAT observations of Cyg X–2 obtained in 1983, which covered the energy band 0.5–20 keV (see Chiappetti *et al.* 1990) and focus our attention on the observations of September 13–22. Assuming a distance of 8 kpc (Cowley, Crampton & Hutchings 1979), the X–ray luminosity is 1.7×10^{38} erg/s, which clearly situates the source close to the Eddington limit for $M_* \sim M_\odot$. A good fit to the data is obtained by the superposition of a bremsstrahlung at 4.4 keV and a black
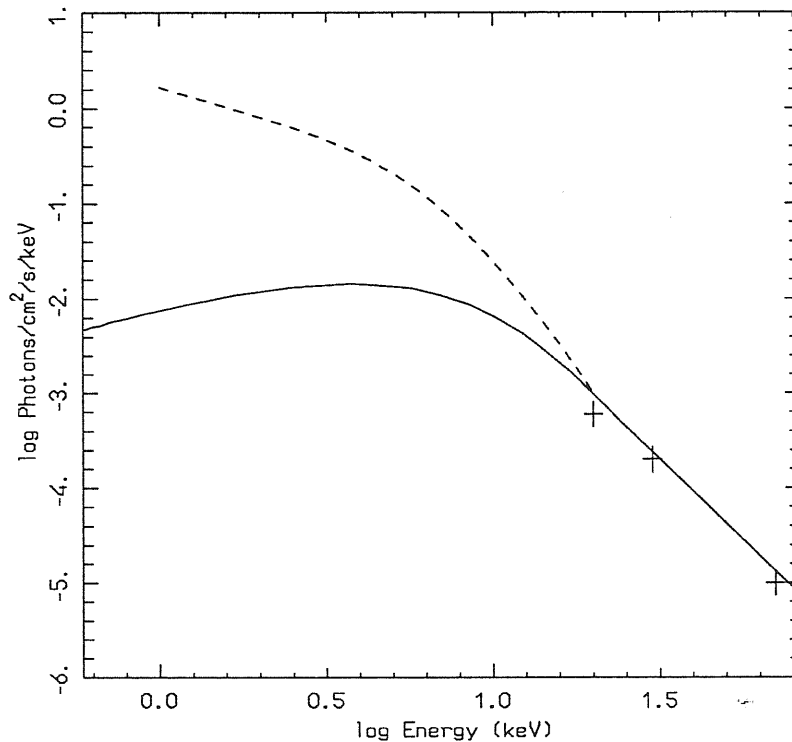
Figure 2.8 – The spectrum of Cyg X–2 in the 1–60 keV range. The dashed line is the best fit to the data of Chiappetti *et al.* (1990), crosses refer to the observations of Maurer *et al.* (1982) and the continuous line is the model spectrum for $l_\infty = 0.9$.

body at 1.2 keV. However, as for other bright LMXBs, several two component models can be fitted equally well to the observed X–ray spectrum (Hirano *et al.* 1984; Vrtilek *et al.* 1986; White, Stella & Parmar 1988; Hasinger *et al.* 1990; Hirano *et al.* 1995). We consider also the high energy observations of Maurer *et al.* (1982), obtained during a balloon flight in May 1976, which detected the source in the 18–60 keV range, with the low energy point at a level comparable to that of the EXOSAT observations. The high energy count rate is well fitted by a power law of spectral index 2.8 ± 0.7. A steep high energy tail (above 20 keV) have been detected also in other balloon–borne observations (Webber & Reinert 1970; Matt *et al.* 1990). Furthermore, an analysis of the HEAO–1 A4 catalogue (van Paradjis & van der Klis 1994) has shown that the ratio of the fluxes

emitted in the 40–80 and 13–25 keV bands is $\simeq 0.016 \pm 0.008$, which is consistent with a power law spectrum with spectral index larger than 3. We have not considered in the present discussion the X–ray spectral observations of Cyg X–2 obtained with Ginga in low–high–voltage mode (2–60 keV; Mitsuda 1992), since, during the observations, the source was mainly in the horizontal branch. In figure 2.8 we have plotted the observed spectrum of Cyg X–2 in the high–level luminosity state (Chiappetti *et al.* 1990), the high energy spectrum of Maurer *et al.* (1982; errors below 20 keV are $\lesssim 10\%$) and our computed spectrum for the model with $l_\infty = 0.9$. A comparison of the synthetic spectrum with the observed one (see figure 2.8) clearly indicates that our model can not describe the number counts in the entire energy range because it exhibits a definite photon deficit at low frequencies. However, the flux energy distribution above ~ 20 keV is a steep power law and it is well fitted by the model; the computed spectral index, $\alpha \simeq 3.4$, is, in fact, consistent with the observed one. On this regard, we note that, at frequencies greater than ~ 10 keV, the energy lost by a photon in the scattering with an electron starts to be no more negligible for the typical bulk velocities of the accreting gas at $l_\infty \sim 0.9$ (see equations (2.41) and (2.42) and the following discussion) and the scattering can no more be considered elastic in the rest frame of the electron. Then, the actual spectral shape at these energies could be modified by the effect of the electron recoil and a more detailed treatment of radiative transfer including thermal comptonization would be required. However, the quantitative good agreement of our computed high energy tails with the observed data of Cyg X–2 may indicate that this effect is not drastically important at least up to energies of ~ 20–30 keV.

As far as the spectral observations of other Z sources are concerned, recent work by the Granat/Sigma group (Barret & Vedrenne 1994) seem to indicate that some of them (GX 5-1, Sco X–1) emit less than $\sim 1\%$ of the total luminosity in hard X–rays (above 30 keV) and that no evidence for flat power law tails can be found. In particular, the spectrum of Sco X–1 obtained with the Kvant module (Sunyaev *et al.* 1991) has a steep high energy cut–off at around 20–30 keV. Using the data contained in the HEAO-1 A4
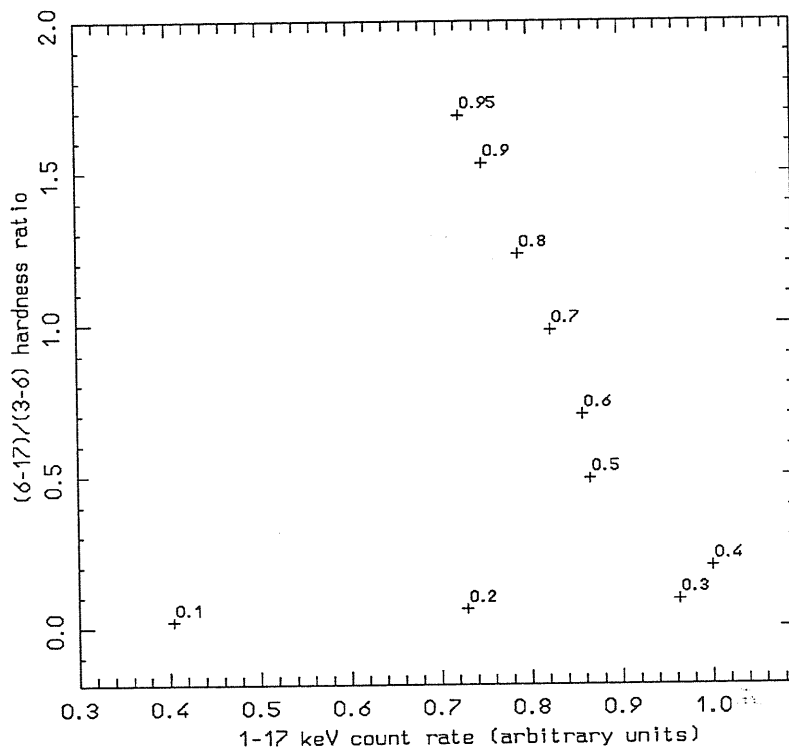
Figure 2.9 – Hardness ratio versus count rate for our models. Each cross is labeled by the value of l_∞ (see also table 2.1).

catalogue, van Paradijs & van der Klis (1994) find that the observed colors of the Z sources are consistent with spectral indices $\alpha > 3$. We note that these results are not in contrast with our conclusions, since the expected power law tails produced by bulk heating in the radial accretion flow are larger than 3 and the flux emitted above 30 keV turns out to be of the order of a few per cent. Moreover, it is likely that the inner disc corona is not perfectly spherically symmetric and inclination effects could come into play. Finally, as discussed above, at high energies ($\gtrsim 30$ keV) ordinary thermal comptonization is no more negligible and, hence, the precise form of the spectrum will depend also on the thermal processes acting in these sources.

As mentioned above, a useful tool for studying the X–ray spectral properties of LMXBs are the intensity–color and color–color diagrams. Cyg X–2 is, in fact, the first

source for which the constancy of the hardness ratio with respect to the intensity was discovered (Branduardi *et al.* 1980). The intensity–color diagram for our solutions is plotted in figure 2.9. The color is defined as the ratio of the number counts in the 6–17 and 3–6 keV bands while the intensity refers to the count rate in the 1–17 keV range. A direct comparison with the observations is of little significance, since the computed spectrum shows a significant deficit of photons with respect to the observed spectrum within the spectral band where the hardness ratio is calculated. In spite of that, the results of figure 2.9 are of interest. As can be seen, for luminosities $l_\infty < 0.4$ the count rate in the 1–17 keV band increases, while, for $l_\infty > 0.4$, it starts to (slowly) decrease, because the spectrum becomes harder and the total number of photons in the interval 1–17 keV becomes lower. This contrasts with the nearly linear dependence of the hardening ratio on the total luminosity (see also table 2.1). The turning point in the diagram corresponds to the model with $l_\infty \simeq 0.4$ which is the value of the luminosity at which the count rate is maximum. We note that the existence of an anticorrelation branch in the intensity–color diagram for our solutions is entirely due to dynamical effects. In fact, in the absence of bulk motion comptonization, the spectrum remains Planckian and drifts to higher frequencies for increasing l_∞ just because $T_* \propto l_\infty^{1/4}$; the gravitational redshift does not enter in these considerations being the same for all the models. It can be easily checked, in fact, that a Planckian spectrum produces always a positive intensity–hardness correlation. The turning point appears only when dynamical effects start to be important. If we explain the X–ray variability of LMXBs in terms of a time varying accretion rate, the turning point present in the intensity–color diagrams of some Z sources, such as Cyg X–2 (see e.g. van der Klis 1991), bears some resemblance with the behaviour of our solutions. As far as the color–color diagram is concerned, within the framework of the unified model of LMXBs (Lamb 1989, 1991), the characteristic Z shape of Cyg X–2 can be qualitatively reproduced. However, as shown by Lamb (1991), if the electron scattering optical depth in the radial inner disc corona is sufficiently high, the observed decrease in the soft color along the normal branch can

be correctly reproduced, whereas the fall in the hard color is too large. As noted by Lamb, several relevant effects were not included in the model, such as the work done on the radiation field by the converging radial flow. Although no direct comparison can be made, we argue that a significant contribution to the hard tail of the spectrum and hence to the hard color along the normal branch could be due to dynamical comptonization.

In conclusion, although the simple model considered here cannot describe the overall X–ray emission of Cyg X–2, we find that dynamical effects due to bulk gas motion (drift to high frequencies and formation of a power law tail) may be an important ingredient to explain some of the observed spectral properties of Z sources. In light of these results, we argue that a more detailed model of spherical accretion onto neutron stars near the Eddington limit, which accounts for an input spectrum different from a black body (such as an unsaturated comptonized spectrum produced from the hot corona) and which can deal with thermal comptonization and free–free emission and absorption along with the effects of bulk acceleration, could allow a more significant comparison of synthetic spectra, intensity–color and color–color diagrams with observations. This study is presently under consideration.

CHAPTER 3
STATIONARY, SPHERICAL ACCRETION ONTO NEUTRON STARS BELOW THE EDDINGTON LIMIT

In section 3.2, results are presented from an investigation of stationary, low rate accretion onto an unmagnetized, non-rotating neutron star. It is found that new "hot" solutions may exist for a wide range of luminosities. These solutions are characterized by a high temperature, 10^9–10^{11} K, and arise from a stationary equilibrium model where the dominant radiative mechanisms are multiple Compton scattering and bremsstrahlung emission. For low luminosities, $\lesssim 10^{-2} \, L_E$, only the "cold" (à la Zel'dovich and Shakura 1969) solution is present.

The spectral properties of X–ray radiation produced in the low temperature, static atmosphere surrounding the neutron star are investigated in section 3.3. Previous results by Alme & Wilson (1973) are extended to the range $10^{-8} \leq L/L_{Edd} \leq 10^{-3}$ to include the typical luminosities, $L \sim 10^{30}$ ergs s^{-1}, expected from isolated neutron stars accreting the interstellar medium. The emergent spectra show an overall hardening with respect to the blackbody at the neutron star effective temperature in addition to a significant excess over the Wien tail.

In the last section of this chapter, the relevance of present spectral results in connection with the observability of Old isolated Neutron Stars (ONSs) accreting from the interstellar medium is discussed. In particular, we focus our attention on the overall soft X–ray emission of ONSs and show that it may provide a substantial contribution to the X–ray background in the 0.5–2 keV band.

3.1 INTRODUCTION

Since the early 1970s, large theoretical efforts have been devoted to investigate the properties of radiation produced by accretion onto neutron stars, in the attempt to model the observed spectra of galactic X–ray sources. Even before the observational evidence that these sources are mostly binary systems containing an accreting neutron star, Zel'dovich & Shakura (1969, ZS in the following) studied in some detail the spectrum of radiation produced by stationary, spherical accretion onto an unmagnetized neutron star and compared their results with the (poor) data available at the time for Sco X–1. The pioneering paper of ZS shows that the resulting spectrum depends essentially on two parameters, the accretion rate (luminosity) and the penetration length of the accreting ions in the outermost neutron star layers. The outcome can be described, in essence, as a black body with a high energy tail due to the Compton heating of thermal photons in the hot, external part of the atmosphere surrounding the neutron star. ZS's analytical work was pushed further by Alme & Wilson (1973, AW in the following), who computed the emergent spectrum for luminosities $L \gtrsim 10^{-2} L_{Edd}$ solving the moments of the transfer equation. Shapiro & Salpeter (1973) adopted essentially ZS solution at the inner boundary and explored the possibility that in the surrounding region a shock is formed, which may modify the resulting spectrum. While models of spherical accretion evolved substantially since then, considering, for instance, the role of nuclear reactions induced in the crust by the bombardment of accreting ions (see e.g. Bildsten, Salpeter & Wasserman 1992), the basic picture proposed by ZS has been maintained.

Here we reinvestigate the thermal and radiative structure of the atmosphere of neutron stars accreting at low rates adopting a set of equations which essentially coincides with those of ZS. We show that ZS's solution for the temperature profile is not unique: for large enough accretion rates, another solution, at considerably higher temperatures, may exist. We have computed also the spectrum emerging from the low temperature, static atmospheres, extending previous calculations by AW to $L \sim 10^{-8} L_{Edd}$. In fact,

up to now the interest mainly focussed on emergent spectra for luminosities in the range $\sim 10^{35} - 10^{38}$ ergs s^{-1}, since most of observed X–ray binaries have $L \gtrsim 10^{34}$ ergs s^{-1}. Much fainter sources may, nevertheless, exist. It was suggested long ago (Ostriker, Rees, & Silk 1970), in fact, that although the thermal emission resulting from cooling of the hot interior is too weak for being observed after a time ~ 10 Gyr, old isolated neutron stars, no longer active as pulsars, may show up as very weak, soft X–ray sources ($L \sim 10^{30} - 10^{31}$ ergs s^{-1}, $T_{eff} \sim 90$ eV; see Chapter 1) if they accrete the interstellar medium (ISM). The low bolometric luminosity and the softness of the spectrum explain the difficulty of observing an isolated ONS. The detection of ONSs was included as a possible target for the *Einstein* mission (Helfand, Chanan & Novick 1980), but it was only a decade later that this issue came to life again when Treves and Colpi (1991, hereafter TC) reconsidered the observability of ONSs with ROSAT. Assuming a black-body spectrum, using the velocity distribution proposed by Paczyński (1990) and a local density 0.07 cm^{-3} for the ISM, they found that thousands of ONSs should appear in the ROSAT PSPC All Sky Survey in the most favorable case of polar cap accretion. A complete analysis by Blaes and Madau (1993, hereafter BM) essentially confirmed TC results. From the numerical calculation of the spectra emitted by low temperature, static atmospheres around neutrons stars, we have found that the emergent spectral distribution at very low luminosity is significantly harder than a blackbody at the star effective temperature. In light of this result and taking into account that the present estimates of the observability of ONSs are all based on the assumption of a Planckian spectrum, we decided to reconsider the issue.

The interest for the X–ray emission from isolated ONSs is not restricted to the detection of individual sources. Despite their intrinsic weakness, in fact, they could provide a contribution to the diffuse X–ray background (XRB), being their total number very large. In a recent paper, Hasinger *et al.* (1993) have analyzed the X–ray emission in selected high–latitude fields and found that the number of resolved sources exceeds by $\sim 60\%$ the number of quasars expected from a standard evolutionary scenario. This

led to the suggestion that a new population of sources can contribute sizeably to the soft X–ray background detected at 0.5–2 keV with ROSAT. Although such a population may be extragalactic in origin, Maoz & Grindlay (1995, hereafter MG) showed that its properties are compatible with those of galactic objects and tentatively identified them with Cataclysmic Variables. Accreting ONSs could have the desired spatial distribution but were ruled out as possible candidates by MG on the basis of their too soft emission. We stress, however, that MG restricted their discussion to the very simple case in which the spectrum is a blackbody at T_{eff}, emitted from the entire star surface. Using our computed spectra we have found that, in the case of polar cap accretion ($B \sim 10^9$ G), the ONSs contribution is $\approx 10\%$ of the total measured intensity in the 0.5–2 keV band, corresponding to $\approx 25\%$ of the observed soft–excess.

3.2 ATMOSPHERIC THERMAL AND RADIATIVE STRUCTURE

We consider a non–rotating, unmagnetized Neutron Star (NS) which undergoes spherical accretion and is surrounded by a geometrically thin, static atmosphere; the envelope material is assumed to be pure hydrogen. As the accretion flow penetrates into the atmosphere, protons are decelerated by Coulomb collisions, their bulk kinetic energy is transferred to electrons and is finally converted into electromagnetic radiation via free–free emission. The input physics of our model essentially coincides with that used in previous studies on this subject (ZS; AW). If the flow velocity vanishes at the star surface, the relativistic efficiency η_{eff} of the accretion process in the Schwarzschild metric is given by equation (2.43)

$$\eta_{eff} = 1 - \sqrt{1 - \frac{r_g}{r}}, \tag{3.1}$$

where $r_g = 2GM_*/c^2$ is the gravitational radius and M_* the mass of the neutron star. For $r_* \simeq 3r_g$ and $M_* \simeq 1.4M_\odot$, $\eta_{eff} \simeq 0.18$. If all of the kinetic energy is converted into photons and considering accretion rates $\dot{M}$ well below the Eddington limit $\dot{M}_{Edd}$,

the luminosity seen by an observer at infinity turns out to be (see equation (2.44))

$$l_\infty = \eta_{eff}\dot{m} \ll 1,\qquad(3.2)$$

where l_∞ and $\dot{m}$ are the luminosity and the accretion rate in Eddington units. Then, the drag exerted by radiation on the impinging flow is negligible and the accreting gas is essentially in free–fall. Significant deviation from free–fall in the accretion flow far from the NS surface can be caused only by heating produced by high temperature radiation coming from the NS atmosphere. However, if we calculate the electron scattering optical depth τ_* between the NS surface and infinity (assuming free–fall), we find

$$\tau_* = \dot{m}\left(\frac{r_*}{r_g}\right)^{-1/2} \ll 1,\qquad(3.3)$$

which implies that Compton heating is very inefficient and any interaction between the radiation field and the accretion flow can be neglected. In these conditions, the radiation spectrum is formed entirely in the static atmosphere around the neutron star.

To study the structure of the geometrically thin atmosphere which surrounds the surface of the neutron star, we introduce the column density

$$\eta = \int_r^\infty \rho\,dr\qquad(3.4)$$

which physically represents the amount of atmospheric material per unit surface above the radius r and can more conveniently be used as the independent variable in place of the radius; here ρ is the matter density. The details of the flow braking are exceedingly complicated (see e.g. Bildsten, Shapiro & Wasserman 1992), also because a collisionless, standing shock can form, as originally suggested by Shapiro & Salpeter (1973). For this reason, following ZS, we treat the total column density of the atmosphere required to stop the incoming protons, η_0, as a free parameter. In the following we will consider $\eta_0 = 5$–20 g cm^{-2}. If the flow velocity v exceeds the electron thermal velocity, v_{th}^e, these values of the proton penetration length are appropriate to describe the stopping of the incoming protons in a hydrogen plasma where only Coulomb interactions take

place. On the contrary, if $v \lesssim v_{th}^e$, the proton stopping through repeated Coulomb scatterings is less effective and other collective processes (e.g. plasma oscillations) need to be considered to keep η_0 within this interval.

The heat injected by the infalling protons per unit time and mass in the atmosphere is assumed to be constant and is related to the total luminosity observed at infinity L_∞ by

$$W = \frac{L_\infty - L_0}{4\pi \int_0^{\eta_0} r^2 y d\eta} \qquad 0 \le \eta \le \eta_0$$
$$= 0 \qquad\qquad\qquad \eta > \eta_0 , \tag{3.5}$$

where $y = (1 - r_g/r)^{1/2}$ and L_0 is the luminosity at the inner boundary of the atmosphere. We note that, owing to the gravitational redshift, the total luminosity seen by a distant observer is related to the local luminosity at the top of the atmosphere by $L_\infty = y^2 L(0)$. More realistic expressions for W, which in general depend on depth, will be considered later.

The runs of pressure, P, and temperature, T, are obtained from the hydrostatic balance and radiative energy equilibrium (equations (1.17) and (1.18) with $v = 0$ and with the additional heating term W)

$$\frac{dP}{d\eta} = \frac{GM_*}{y^2 r^2} \left(\frac{h}{c^2} - \frac{\kappa_1}{\kappa_{es}} \frac{yL}{L_{Edd}} \right) \tag{3.6}$$

$$\frac{W}{c} = (\bar{\epsilon} - \kappa_0 w_0) + 4 k_{es} w_0 \frac{KT}{m_e c^2} \left(1 - \frac{T_\gamma}{T} \right) , \tag{3.7}$$

where w_0 is the radiation energy density, $L = 4\pi r^2 w_1 c$ is the radiative luminosity (both measured by the local observer) and h is the specific enthalpy of the atmospheric gas. The matter density ρ is calculated from the perfect gas equation of state for completely ionized hydrogen, $P = 2\rho KT/m_p$. Since we study the general properties of spherical accretion onto neutron stars for luminosities well below the Eddington limit, in equation (3.6) we neglected the ram pressure exerted by the incoming protons, which is typically two orders of magnitude below the gravitational term. The absorption opacity is approximated using the Planck mean k_P, while the flux mean can be conveniently

expressed as (see equation 4.4)

$$\kappa_1 = k_{es} + 6.4 \times 10^{22} \rho T^{-7/2} \ \mathrm{cm^2 \ g^{-1}} \ . \tag{3.8}$$

Using the Kirchhoff law the free–free emissivity can be re–written as $\bar{\epsilon} = k_P a_R T^4$, where a_R is the blackbody radiation constant. The radiation temperature T_γ is defined in equation (1.32).

The transfer of radiation in the atmosphere is governed by the equations for the radiative luminosity and the radiation energy density which, in spherical symmetry and using the Eddington approximation, can be written as (see equations (1.28) and (1.29) with $v = 0$ and $w_2 = 0$)

$$\frac{d(y^2 L)}{d\eta} = -4\pi r^2 y W \tag{3.9}$$

$$\frac{1}{3}\frac{d(y^4 w_0)}{d\eta} = \kappa_1 \frac{y^3 L}{4\pi r^2 c} \ . \tag{3.10}$$

Since, as numerical models show, the atmosphere does not expand significantly even for high temperature solutions, the Eddington approximation is reasonable.

In general, the radiation temperature T_γ can be computed only solving the full frequency–dependent transfer problem and will depend on η (in ZS, T_γ was taken equal to $[w_0(\eta)/a]^{1/4}$, which is appropriate only in LTE). In the following, T_γ will be calculated from an equation which will be presented in Chapter 4; it describes the variation of the radiation temperature when multiple Compton scattering becomes important and, in terms of the column density $\eta = \tau/k_{es}$, it can be written (see equation (4.11))

$$\frac{d\ln T_\gamma}{d\ln \eta} = 2Y_c \left(\frac{T_\gamma}{T} - 1\right) , \tag{3.11}$$

where $Y_c = (4KT/m_e c^2)\max(\tau, \tau^2)$ is the Compton parameter. As it will be discussed later, use of equation (3.11) requires some care since it is meant to describe the variation of the radiation temperature when multiple Compton scattering is the dominant mechanism to exchange energy between photons and electrons. Equation (3.11) therefore does not apply if either $\tau_{es} < 1$ or true emission–absorption are important. On

the other hand, equation (3.11) gives the correct limit for low optical depth ($Y_c \ll 1$ implying $T_\gamma = constant$), so that one can extend the validity of equation (3.11) to all regimes, provided that no physical significance is attached to T_γ where the effective optical depth $\tau_{eff} > 1$. In this case, the second term on the right hand side of equation (3.7) is negligible compared with the true emission–absorption term and an accurate evaluation of T_γ is no longer needed.

Finally, since we are using the column density η as independent variable, we can compute the radius r directly from equation (3.4)

$$\frac{dr}{d\eta} = -\frac{1}{\rho}\,.$$

(3.12)

During the numerical calculation we used equation (3.12) to check if the atmosphere remains geometrically thin.

3.2.1 Boundary Conditions

The solution of equations (3.6), (3.7), (3.9)–(3.12) provides the variation of P, T, L, w_0, T_γ and r as functions of the column density η and is found numerically; here $10^{-2} \leq \eta \leq 10^2$ g cm^{-2} and all models refer to a neutron star of $r_* = 10$ km and $M_* = 1.4\,M_\odot$. This system of 5 first order, ordinary differential equations plus an algebraic equation have to be supplemented with a corresponding number of boundary conditions which are listed below. In the study of stellar atmospheres the natural boundary condition for the hydrostatic equilibrium equation is that at the top of the atmosphere the gas pressure vanishes: $P = 0$ at $\eta = \eta_{out}$. As far as equation (3.12) is concerned, we require that at the neutron star surface $r = r_*$, $\eta = \eta_{in}$. The appropriate boundary condition for the radiation field at the outer edge of a non–illuminated medium is $w_0(\eta_{out}) = L_\infty/2\pi R^2 y^2 c$, while, at the inner boundary, we account for the possible presence of a radiative input flux: $L(\eta_{in}) = L_{in} = L_0/y^2$. If all of the observed luminosity is generated within the atmosphere, $L_{in} = 0$. This is the same condition used by ZS and is appropriate if the effective optical depth close to η_{in} is very large.

We note that a boundary condition for T_γ must also be imposed because the radiation temperature obeys a differential equation; models were obtained specifying a value of T_γ at $\eta = \eta_{out}$.

3.2.2 Results

We have found that two distinct kinds of solutions, "hot" and "cold", always exist for any η_0 provided that the luminosity exceeds a certain limit, which depends on η_0. The thermal properties of the atmosphere are illustrated in figures 3.1 and 3.2, where the run of T versus column density is shown for different luminosities in the case $\eta_0 = 20$ g cm^{-2}. The "cold" solutions of figure 3.1 are just those already found by ZS and are obtained setting $T_\gamma(\eta_{out}) = [L_\infty/(4\pi r_*^2 \sigma)]^{1/4}$. As can be seen from the figure, the temperature profile is nearly adiabatic in the inner layers where the gas is optically thick to true emission–absorption. The sudden increase of T in the external layers is due to the heating produced by the incoming protons, balanced mainly by Compton cooling at low densities. The temperature "shock" moves at very low values of the column density as luminosity decreases. The "hot" solutions of figure 3.2 exist for values of T_γ satisfying the condition $T_\gamma > T_{crit}(L_\infty, \eta_0)$; here $T_\gamma(\eta_{out}) = 2 \times 10^9$ K. The temperature is close to T_γ in the outer region ($\eta \lesssim 23$ g cm^{-2}), while in the dense layers close to η_{in} LTE is attained at $T \sim 10^7$ K. Cold, thermal photons do not propagate outwards because $L = 0$ for $\eta_0 < \eta < \eta_{in}$, so the hot and the cold zone are thermally decoupled, at least radiatively. On the other hand, we have checked that imposing an outgoing flux at η_{in} does not alter our picture significantly if $|L_0|/L_\infty \lesssim 0.1$.

The presence of two possible regimes has a simple interpretation in terms of the relative efficiency of the two radiative processes we have considered, Compton scattering and free–free emission–absorption. The static atmosphere must, in fact, radiate a given luminosity and, for doing that in the scenario we are proposing, there are two ways. A first possibility is that a lot of soft bremsstrahlung photons are produced in a low–temperature, dense medium in which the effective depth is large. This gives rise
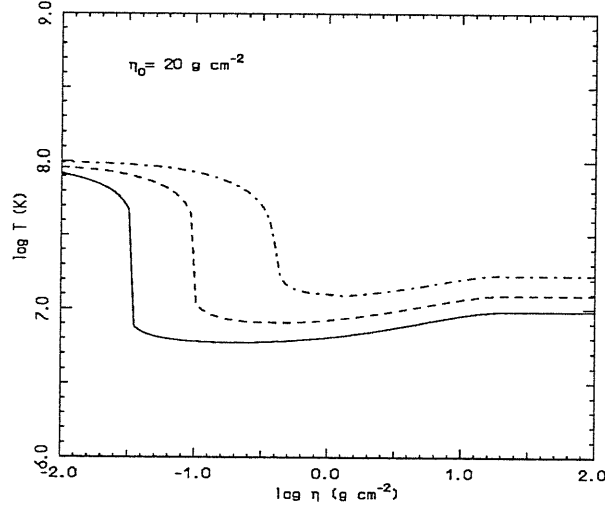
Figure 3.1 – Temperature versus column density of "cold" solutions for $l_\infty = 7 \times 10^{-3}$ (continuous line), $l_\infty = 2 \times 10^{-2}$ (dashed line) and $l_\infty = 7 \times 10^{-2}$ (dashed–dotted line); here $\eta_0 = 20$ g cm^{-2} and $|L_0|/L_\infty \lesssim 0.1$.

to a spectrum which is essentially blackbody and corresponds to the "cold" solution. Comptonization is never dominant because temperature is low and the scattering depth is not large enough to make $Y_c > 1$. The "hot" solutions represent the opposite case, in which much less energy is generated through bremsstrahlung emission in a low–density, hot plasma far from LTE. Comptonization, however, is now so efficient that matter and radiation temperatures are everywhere very close and the same energy output can be obtained.

It is possible to get an insight on the existence of high–temperature solutions and to give an estimate of the limiting value T_{crit} by means of simple analytical considerations, using, for the sake of simplicity, a plane–parallel geometry for the atmosphere. For $\eta < \eta_0$ we can safely neglect free–free absorption in equation (3.7) and, not considering general relativistic effects (i.e. setting $y = 1$), we get the expressions for L, w_0 and ρ as functions of η and T:
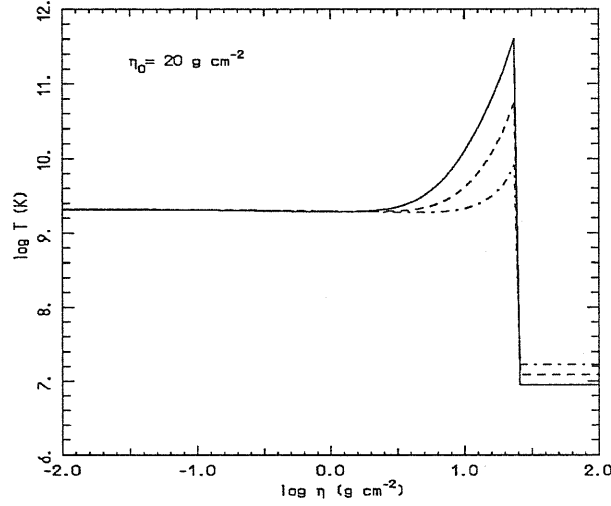
Figure 3.2 – The same as in figure 3.1 for "hot" solutions.

$$L = L_\infty \frac{\eta_0 - \eta}{\eta_0} \tag{3.13}$$

$$w_0 = \frac{W}{c} \left[2\eta_0 + 3k_{es}\eta \left(\eta_0 - \frac{\eta}{2} \right) \right] \tag{3.14}$$

$$\rho = D\frac{\eta}{T} \tag{3.15}$$

where $D = GM_* m_p / 2Kr_*^2 = 8.1 \times 10^5$, in c.g.s. units for $r_* = 10^6$ cm and $M_* = 1\,M_\odot$. Neglecting the term $\kappa_0 w_0$, the energy equation becomes a cubic equation in $\theta = T^{1/2}$, that can be studied analytically for given values of η_0 and L_∞ and treating T_γ as a free parameter. Equation (3.7) can be cast into the form

$$\theta^3 + p_c\,\theta + q_c = 0 \tag{3.16}$$

with

$$p_c = -\left(T_\gamma + A_c \frac{l_\infty}{w_0} \right) \sim -T_\gamma$$

$$q_c = B_c \frac{\eta}{w_0(\eta)} \; ;$$

$A_c = 6.3 \times 10^{22}$ and $B_c = 5.1 \times 10^{25}$, again in c.g.s. units. The approximate expression for p_c holds only for $T_\gamma \gg 10^8 \text{K}$, while, in order to make the analytical treatment possible, in the inner part of the atmosphere q_c is set approximately equal to its maximum value, $(q_c)_{max} = q_c(\eta_0)$. Once η_0 and l_∞ are fixed, equation (3.16) has one or three real roots, according to the sign of the discriminant, and it is easy to prove that all the roots are real only if

$$T_\gamma \geq \frac{2.5 \times 10^8}{\left(1 + \frac{3}{4} k_{es} \eta_0\right)^{2/3} l_\infty^{2/3}} \, \text{K} \, . \tag{3.17}$$

It can also be shown that if just one real root is present, then it satisfies $T \gtrsim T_\gamma$, whereas, if condition (3.17) is satisfied, the three roots have magnitudes $T \gtrsim T_\gamma$, $T << T_\gamma$ and $T \lesssim T_\gamma$, respectively. The solution $T \gtrsim T_\gamma$ is unacceptable since $T > T_\gamma$ will produce a negative radiation temperature gradient (see equation (3.11)) and also $T << T_\gamma$ must be rejected because it is inconsistent with our starting assumption that absorption could be neglected because the plasma is very hot. Finally, the root $T \lesssim T_\gamma$ is the "hot" solution; it exists only when the radiation temperature exceeds the limit given by (3.17), which represents the analytical estimate of T_{crit}.

In figure 3.3 we plot the mean energy of the outgoing photons as a function of the total luminosity for $\eta_0 = 20 \text{ g cm}^{-2}$. For "hot" solutions only the lower bound T_{crit} (dashed line) is shown. As can be seen, while the mean photon energy of the "cold" solutions (crosses) monotonically increases with the luminosity, the lower bound T_{crit} for "hot" solutions shows the opposite behaviour. The "hot" and "cold" solutions coexist for a certain range of luminosities and the mean photon energies of the two modes approach each other for increasing l_∞. The "cold" solution becomes hotter for increasing accretion rate while the "hot" one softens and this behaviour is opposite to the one exhibited by the hot, shocked solutions of Shapiro & Salpeter (1973). Moreover the numerical analysis indicates that high temperature solutions may exist only for high enough values of l_∞ and that the critical luminosity , l_{cr}, below which no "hot" solutions exist depends on η_0: for $\eta_0 = 5 \text{ g cm}^{-2}$, $l_{cr} = 2 \times 10^{-2}$, while for $\eta_0 = 20 \text{ g cm}^{-2}$, $l_{cr} = 6 \times 10^{-3}$.
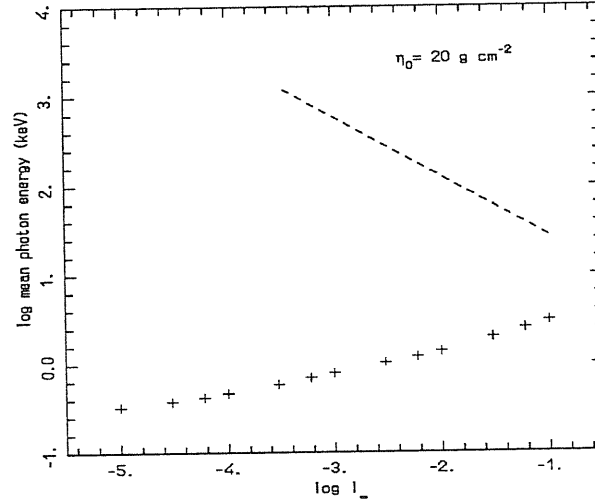
Figure 3.3 – Mean energy of the outgoing photons versus total emitted luminosity for $\eta_0 = 20$ g cm^{-2}; crosses refer to "cold" models. The dashed line represents the lower limit for the existence of "hot" solutions given by equation (3.17).

The anticorrelation between T_{crit} and l_∞, and the lack of "hot" solutions at low luminosities can be explained as follows. As l_∞ decreases, W and w_0 start to decrease (see equations (3.5) and (3.14)) and, since Compton heating (which is dominant over cooling) becomes progressively smaller in magnitude, the free–free emissivity $\left(\bar{\epsilon} \propto \rho T^{1/2} \propto P/T^{1/2}\right)$ must also decrease for the energy equation to be satisfied. This can be achieved only by an increase of temperature (and a decrease of density, see equation (3.15)) because the pressure profile is nearly independent on the thermal properties of the gas. The lack of "hot" solutions at small luminosities is due to the fact that, when density is very low, the envelope becomes photon starved and even a strong comptonization is unable to produce the required luminosity.

Comptonization and bremsstrahlung emission from this hot layer could produce hard X–ray spectra (50–100 keV). The existence of both "cold" and "hot" solutions for the same values of the flow parameters has been already found in black hole accretion (Park 1990a; Nobili, Turolla & Zampieri 1991) when both free–free and Compton scattering

are present. An alternative picture for the production of hard X-rays (~ 100 keV) from accreting neutron stars has been proposed by Kluźniak & Wilson (1991). In their model matter coming from the inner edge of an accretion disk hits the stellar surface at a shallow angle, creating a hot equatorial belt in which Compton cooling is very efficient. It is quite interesting to note that also Zel'dovich & Shakura proposed a "hot" model in which the reduction of the mean free path of the incident protons, due to the deceleration produced by plasma oscillations, can raise the temperature in the outer part of the atmosphere up to 10^9 K.

The basic limitations of our approach are obviously that the analysis is stationary and the spectrum is described just in terms of a mean photon energy. The fact that "hot" models may exist only for high enough radiation temperatures, $T_\gamma \gtrsim T_{crit} \simeq 10^9$K at the outer boundary, suggests that, in order to get started, an extra energy input, different from that produced by the incoming matter flux, must be supplied. A physically consistent scenario should be investigated in a time–dependent picture. Furthermore temperatures are mildly relativistic and the expression we used for the Compton heating–cooling term is just an approximation. Moreover, pair production–annihilation can not be neglected for $l_\infty \gtrsim 10^{-2}$ when the compactness parameter becomes $\gtrsim 10$. Above $l_\infty \sim 0.1$, the dynamical effects of radiation pressure and bulk motion comptonization become also important (see Chapter 2) and are not included in the present model.

The existence of "hot" solutions for intermediate luminosities with temperatures ~ 100 keV suggests that a class of hard X-ray sources, which possibly have not yet been discovered, may exist. The transition between the "hot" and the "cold" regime, even at luminosities where the two solutions are rather different, may be expected in a time–dependent scenario. Non–stationary calculations are also needed to explore the stability properties of the two solutions.

3.3 EMITTED SPECTRUM FOR "COLD" SOLUTIONS

As shown in the previous section, at very low accretion rates (the threshold depends on η_0) there is a unique solution, the "cold" one discovered by ZS (see figure 3.3). Since in the following we are interested in investigating the spectral properties at very low accretion rates, such those encountered in Old isolated Neutron Stars accreting from the interstellar medium, we will focus on the study of these solutions.

We have demonstrated that no significant expansion occurs in both "cold" and "hot" envelopes, so that in the following we will treat the radial coordinate as a constant, equal to the neutron star radius r_*. The heat injected per unit time and mass in the envelope is calculated using a more realistic expression for the energy loss rate due to Coulomb collisions of super–thermal protons (see Bildsten, Salpeter & Wasserman 1992),

$$W = \frac{L_\infty - L_0}{8\pi r_*^2 \eta_0 y} \frac{1 + v_{th}^2/v_i^2}{[1 - (1 - v_{th}^4/v_i^4)(\eta/\eta_0)]^{1/2}} \qquad 0 \le \eta \le \eta_0$$
$$= 0 \qquad \eta > \eta_0 ,$$

(3.18)

where $v_i^2 = c^2(1 - L_\infty/L_{Edd})/3$ is the "modified" free–fall velocity, $v_{th}^2 = 3kT/m_p$ is the proton thermal velocity.

The monochromatic radiation energy density W_0 and flux $F = cW_1$ (both measured by the local observer) are obtained solving the first two frequency–dependent transfer moment equations in the Eddington approximation (equations (1.24) and (1.25) with $v = 0$ and $W_2 = W_3 = 0$)

$$\frac{F}{cW_0}\left[\frac{\partial \ln F}{\partial \eta} - \frac{GM_*}{c^2 \rho y^2 r_*^2}\left(1 - \frac{\partial \ln F}{\partial \ln \nu}\right) - \frac{2}{\rho r_*}\right] = -\frac{S_0}{yW_0\rho}$$

(3.19)

$$\frac{1}{3}\frac{\partial \ln W_0}{\partial \eta} - \frac{GM_*}{c^2 \rho y^2 r_*^2}\left(1 - \frac{1}{3}\frac{\partial \ln W_0}{\partial \ln \nu}\right) = -\frac{S_1}{yW_0\rho} .$$

(3.20)

The first two moments of the source function, S_0 and S_1, account for the exchange of energy and momentum between electrons and photons and, for the radiative processes we are considering, bremsstrahlung and electron scattering, they have the form (1.26) and (1.27), respectively. The free–free opacity for a completely ionized hydrogen gas is

expressed by

$$k_{ff} = 1.318 \times 10^{56} \rho T^{-1/2} \frac{1 - e^{-h\nu/kT}}{\nu^3} \bar{g}(\nu, T) \; \mathrm{cm}^2 \, \mathrm{g}^{-1} \,, \tag{3.21}$$

where a functional fit to Karzas & Latter's (1961) tables was used for the velocity-averaged Gaunt factor $\bar{g}(\nu, T)$. Since equations (3.19) and (3.20) define a second order elliptic operator, conditions must be prescribed on the entire boundary of the integration domain and their form is discussed in Nobili, Turolla & Zampieri (1993). In particular, we assume that diffusion holds in the deep layers where LTE is certainly attained and this automatically fixes the luminosity at the inner boundary, L_{in}.

Although the total radiation energy density and luminosity needed in equations (3.6) and (3.7) are just the integrals of W_0 and $4\pi r_*^2 F$ over frequency, we found numerically more convenient to derive them from the first two gray moment equations (3.9) and (3.10). Taking $r = r_* = constant$ and considering the expression for W given in equations (3.18), equation (3.9) can be solved analitically

$$\begin{aligned}
L &= \frac{L_\infty}{y^2} - \left(\frac{L_\infty}{y^2} - L_{in} \right) \frac{1 - [1 - (1 - v_{th}^4/v_i^4)(\eta/\eta_0)]^{1/2}}{1 - v_{th}^2/v_i^2} \qquad & 0 \leq \eta \leq \eta_0 \\
&= L_{in} & \eta > \eta_0 \,,
\end{aligned} \tag{3.22}$$

with the boundary condition $L(\eta_{in}) = L_{in} = L_0/y^2$. The radiation temperature T_γ is computed directly from its definition (equation (1.32)).

Equations (3.6), (3.7), (3.10), (3.19) and (3.20) were solved numerically by means of an original finite differences relaxation scheme (see Nobili, Turolla & Zampieri 1993) on a logarithmic grid of 50 frequency bins $\times$ 100 depth zones. The integration range was typically $-0.7 < \log h\nu/kT_* < 1.1$, with $T_* = T(\eta_{in})$, $-7.6 < \log \eta < \log \eta_{in}$, with η_{in} marginally smaller than η_0. A typical run required ~ 15 minutes of CPU time on an IBM RISC/6000. Two sets of models were computed, both with $r_* = 12.4$ km, $M_* = 1.4 M_\odot$: $\eta_0 = 20 \, \mathrm{g \, cm}^{-2}$ and luminosities in the range $4 \times 10^{-8} \leq L_\infty/L_{Edd} \leq 0.2$, $\eta_0 = 5 \, \mathrm{g \, cm}^{-2}$ and $10^{-7} \leq L_\infty/L_{Edd} \leq 10^{-5}$. Our numerical method should guarantee a fractional accuracy better than 1% on all the variables. As a further check, the total

luminosity, given by equation (3.22), was compared with the numerical integral of F over the frequency mesh at each depth: agreement was always better than 10%. We have also verified that our solutions with $L_\infty \gtrsim 10^{-2} L_{Edd}$ reproduce almost exactly those computed by AW. For low–luminosity models, which we are mainly interested in, particular care must be used to handle properly the absorption and flux mean opacities, since the envelope thermal balance depends entirely on the free–free integrated source term and the radiation spectrum becomes very nearly Planckian in the deeper layers.

The emergent spectra are shown in figures 3.4 and 3.5 for different values of L_∞. In all these models it is $\eta_0 = 20$ g cm^{-2}; solutions with $\eta_0 = 5$ g cm^{-2} show the same qualitative behaviour. A quite unexpected feature emerging from figures 3.4 and 3.5 is that the spectral shape deviates more and more from a blackbody as L_∞ decreases. The model with $L_\infty = 2.25 \times 10^{-2} L_{Edd}$ is, in fact, quite Planckian in shape (see also AW), showing only a moderate hard excess. On the contrary, solutions with $L_\infty < 10^{-4} L_{Edd}$ are characterized by a very broad maximum and by a slow decay at high energies. Comptonization is relatively important for $L \gtrsim 10^{-2} L_{Edd}$, similarly to what happens in X–ray burster atmospheres (see e.g. London, Taam, & Howard 1986). For less luminous models, however, non–conservative scatterings play essentially no role in the formation of the spectrum, as it should be expected since the temperature, and hence the Compton parameter, becomes lower.

Although the hard excess present in our low–luminosity spectra may be of interest as far as predictions on the observability of ONSs are concerned, more important, in this respect, seems to be the comparison of the actual emerging spectrum with the blackbody at the neutron star effective temperature, $B_\nu(T_{eff})$, $T_{eff} = [L_\infty/(4\pi r_*^2 \sigma)]^{1/4}$, which was assumed to be the emitted spectrum in all previous investigations (e.g. TC, BM). It is apparent from figure 3.5 that model spectra with $L \lesssim 10^{-5} L_{Edd}$ are substantially harder than the blackbody at the star effective temperature. The spectral hardening
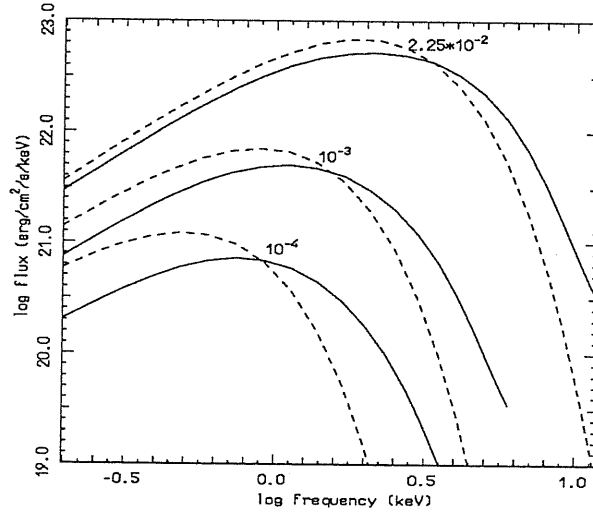
Figure 3.4 – Emergent spectra for $L_\infty = 2.25 \times 10^{-2}, 10^{-3}, 10^{-4}$ L_{Edd} (full lines), together with the corresponding blackbody spectra at the neutron star effective temperature (dashed lines).

can be quantified introducing a hardening ratio

$$\gamma = \frac{T_\gamma}{T_\gamma[B_\nu(T_{eff})]} \, , \tag{3.23}$$

where $T_\gamma[B_\nu(T_{eff})] = 0.96 T_{eff}$. This differs from the usual definition, $\gamma = T_{col}/T_{eff}$, where T_{col} is the color temperature, because our spectra are not always well fitted by a blackbody. For $\eta_0 = 20$ $g\,cm^{-2}$, γ steadily increases from ~ 1.5 (value typical of X–ray bursters in the static phase) for $L \sim 10^{-2}$–$10^{-3}L_{Edd}$, up to ~ 2.5 for $L \sim 10^{-6}$–$10^{-8}L_{Edd}$ (see table 3.1).

The significant deviation of low–luminosity spectra from a Planckian equilibrium distribution could appear unexpected, since radiation is in LTE in a medium where the scattering depth is always much less than the absorption one. The source function should be Planckian and the emergent spectrum, formed at the thermal photosphere, should coincide with $B_\nu(T_{eff})$. However, if the atmosphere develops smooth temperature and density gradients in layers where the medium becomes optically thin to free–free, the differential nature of absorption opacity plays an important role. High–frequency photons
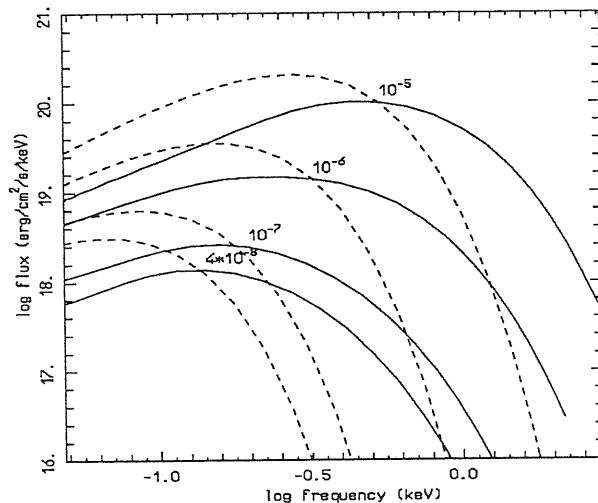
Figure 3.5 – The same as in figure 3.4 for models with $L_\infty = 10^{-5}, 10^{-6}, 10^{-7}, 4 \times 10^{-8} \; L_{Edd}$.

decouple in the deeper, hotter layers and then propagate freely to infinity, contributing to the high–energy part of the emergent spectral flux. At large enough frequencies, the observed shape of the spectrum turns out to be a superposition of planckians at different temperatures. This result resembles closely that of standard accretion disks, where the emergent spectrum shows a broad plateau due to the combined, thermal emission of rings at different temperatures.

Our present result that low–luminosity spectra are harder than a blackbody is consistent with the previous finding by Romani (1987), who computed model atmospheres for cooling neutron stars. Although he considered a quite different physical scenario, an atmosphere in radiative energy equilibrium illuminated from below, the free–free opacity in his cool, He models ($T_{eff} \sim 3 \times 10^5$ K) acts in much the same way as in our faint solutions, producing a hardening of the spectrum. Both in Romani's and in our analysis the effects of the neutron star magnetic field were ignored. An insight on the role of a strong magnetic field, $B \sim 10^{12}$ G, on radiative transfer was recently provided by Miller (1992) and Shibanov *et al.* (1992), who showed that departures from a blackbody

Table **3.1** – Characteristic Parameters for Selected Models

$\dfrac{L_\infty}{L_{Edd}}$	T_γ (keV)	$\dfrac{F_{>0.1}}{F^{bb}_{>0.1}}$ [a]	γ [b]	γ [c]
2.25×10^{-2}	1.03	1.01	1.40	–
10^{-3}	0.53	1.03	1.56	–
10^{-4}	0.35	1.01	1.88	–
10^{-5}	0.24	1.02	2.21	2.06
10^{-6}	0.15	1.07	2.44	2.31
10^{-7}	0.09	1.34	2.64	2.55
4×10^{-8}	0.07	1.92	2.72	–

[a] Ratio of integrated flux to blackbody one above 0.1 keV, for models with $\eta_0 = 20\,\mathrm{g\,cm^{-2}}$.
[b] Hardening ratio, defined in equation (3.23), for models with $\eta_0 = 20\,\mathrm{g\,cm^{-2}}$.
[c] Hardening ratio for models with $\eta_0 = 5\,\mathrm{g\,cm^{-2}}$.

become less pronounced, since the decay of the opacity is less steep at high frequency than in the unmagnetized case. Finally we note that the assumption of a pure hydrogen chemical composition used here, is not entirely ad hoc. In fact, contrary to what happens in equilibrium atmospheres, such as those considered by Romani and Miller who allowed for different compositions, it is likely that metals are destroyed in the accretion flow (Bildsten, Salpeter & Wasserman 1992), leaving just a hydrogen envelope.

As we already noticed, the leading motivation for studying the spectral properties of X–ray radiation coming from neutron stars accreting at low rates, stems from the possible detection of isolated objects fed by the interstellar gas. Their expected luminosities, $\sim 10^{30}$ ergs s^{-1}, could be within reach of satellites like Einstein and ROSAT. Very recently Stocke *et al.* (1995) pointed out that one of the objects in the Einstein Extended Medium Sensitivity Survey may be actually an ONS, consistently with the original suggestion by TC. The knowledge of the emitted spectrum is fundamental in estimating the observability of any X–ray source and our synthetic spectra, being significantly harder than the blackbody at T_{eff}, may indeed increase the chances of detection. In table

3.1 we have listed the ratios of the computed flux above 0.1 keV to the blackbody one for various luminosities; the threshold of 0.1 keV was suggested by the sensitivity of ROSAT. The solutions with $L \sim 10^{-7}$ and $\sim 10^{-5} L_{Edd}$ can be taken as representative of the typical luminosities expected from ONSs embedded in the average ISM or in Giant Molecular Clouds (see Colpi, Campana & Treves 1993). As can be seen from the table, the ratio becomes larger than unity and the flux above 0.1 keV is from $\sim 10\%$ to $\sim 40\%$ larger than the blackbody one for $10^{30} \lesssim L \lesssim 10^{31}$ ergs s^{-1}. We will investigate the consequences of these results in connection with the observability issue of ONSs in the following section.

3.4 OLD ISOLATED NEUTRON STARS

As discussed in Chapter 1, if certain conditions are satisfied, at a certain stage of their life isolated neutron stars may undergo accretion from the surrounding interstellar gas and may show up as weak, soft X–ray sources, as firstly suggested by Ostriker, Rees & Silk (1970). The very hypothesis of accretion is questionable if a relic magnetic field is present and, to ensure that accretion is not stopped by the joint action of magnetic pressure and rotation, in the following we will assume that the neutron star magnetic field B is $\lesssim 10^9$ G.

The total luminosity L emitted by an ONS moving with velocity v relative to the ISM and undergoing accretion from interstellar gas of density n is (Novikov & Thorne 1973)

$$\ell = \eta_{eff} \dot{m} = 1.85 \times 10^{-3} \eta_{eff} \frac{n}{v^{-3}} \, , \tag{3.24}$$

where η_{eff} is the relativistic efficiency defined in equation (2.43) ($\eta_{eff} \simeq 0.18$ for $r_* \simeq 3r_g$ and $M_* \simeq 1.4 M_\odot$), $n = (1 + \chi)n_H$ ($\chi = 0.36$ for standard chemical composition), n_H is the hydrogen number density, ℓ and $\dot{m}$ are the luminosity and the accretion rate in Eddington units; the velocity is in km/s. If the star moves subsonically relative to the ISM, equation (3.24) remains valid provided that the ISM sound speed c_s is used in place of v ($c_s \simeq 10\sqrt{(T/10^4 \, \mathrm{K})}$ km s^{-1}). For typical values of the emitted flux and the

ISM density, the Strömgren radius, inside which the ambient medium is photoionized by the neutron star emission, is much larger than the accretion radius and then the temperature of the accreting gas is always $\gtrsim 10^4$ K.

As shown by equation (3.24), in order to investigate the detectability issue and to evaluate the contribution to the X-ray background of ONSs, it is crucial to have knowledge of the density distribution of the ISM and the velocity distribution of ONSs in the Galaxy. Calculations of the time evolution of the distribution function f of ONSs have been carried out by many authors (Paczyński 1990; Blaes & Rajagopal 1991; BM). Unfortunately, the velocity distribution of pulsars at birth is poorly known and any evolutionary scenario remains affected by this indetermination. In a detailed study, Narayan & Ostriker (1990), starting from the observational data of about 300 pulsars, showed that their distribution in the parameter space can be well fitted assuming the presence of two populations of NSs at birth, slow (S) and fast (F) rotators. In a recent paper, based on a sample of 29 young pulsars, Lyne & Lorimer (1994) suggested the possibility that neutron stars are born with typical velocities higher than both the F and S populations of Narayan & Ostriker. Their sample, however, is not complete and the result would *prima facie* imply that most pulsars evaporate from globular clusters and the Galactic plane, leaving at present only a small Galactic population of low velocity objects. For this reason we retain the velocity distribution at birth proposed by Narayan & Ostriker. Since high velocity objects do not contribute sizeably to the possibility of detection (see equation (3.24)) and no detailed tabulation for f is given, we have repeated the calculation presented by BM, evolving the distribution function for the population F (which is characterized by the lowest value of the mean velocity) of model b of Narayan & Ostriker. All NSs were assumed to be born at $t = 0$. The Galactic potential is sum of three contributions, disk, spheroid and halo, and is taken from Blaes & Rajagopal (1991). The fraction of F objects is 55 % of the total number of neutron stars, and we use $N_{tot} = 10^9$. The distribution function was calculated integrating the orbits of 48000 stars, up to $t = 10^{10}$ ys. Initial conditions at $t = 0$

were obtained assuming that the velocity distribution is gaussian in each component, together with the vertical distribution; the radial one is poissonian and the azimuthal one is uniform. In the local region 7.5 kpc $\leq R \leq$ 9.5 kpc (R is the galactocentric radius) we find $\langle z^2 \rangle^{1/2} = 739$ pc: $\langle z \rangle = 261$ and 249 pc in the northern and southern hemisphere, respectively (z is the height above the plane of the Galaxy). The mean velocity in this local region, averaged over $|z| \leq 200$ pc, turns out to be 78 km/s, and $\langle v^2 \rangle^{1/2} = 87$ km/s. All these values are in close agreement with the results obtained by BM.

As far as the structure of the Local Interstellar Medium is concerned, it has been widely investigated by a number of authors (Frisch and York 1983; Paresce 1984; Welsh et al. 1994; Diamond et al. 1995). Within ~ 50–100 pc from the Sun, the gas is tenuous ($n \simeq 0.05 - 0.07$ cm^{-3}) and warm ($T \simeq 10^4$ K), although at distances less than 20 pc, in the so called "Local Fluff", the very local value of the density is slightly higher ($n \simeq 0.1$ cm^{-3}). On much larger scales, according to Dickey & Lockman (1990), the average density of cool ($T \simeq 10^2$ K) material in the Galactic plane is generally known to be $n \simeq 0.6$ cm^{-3} with a scale height variable with the distance from the Sun, although there are a number of hot ($T \simeq 10^5$–10^6 K) bubbles almost devoid of material ($n \simeq 0.01$ cm^{-3}). In the following, in connection with the observability of individual sources, the local ISM will be approximately described as a constant density medium with $n_H = 0.2$–1 cm^{-3}, whereas for the distribution of the ISM in the Galaxy we consider the following picture, based on the presence of two main components, namely neutral hydrogen and molecular hydrogen: for a wide range of distances ($0.4 \leq R/R_0 \leq 1$, where $R_0 = 8.5$ Kpc is the distance of the Sun from the Galactic center), the neutral hydrogen distribution is nearly constant with radius and can be well fitted by a superposition of two gaussians and an exponential with a mid–plane density ~ 0.6 cm^{-3} and a scale height above the Galactic plane $\simeq 230$ pc (Dickey & Lockman 1990). Observations for the molecular hydrogen distribution are less conclusive and here it will be approximated with a local gaussian distribution with central density ~ 0.6 cm^{-3} and scale height $\simeq 70$ pc (Bloemen

1987; De Boer 1991). Finally, in the calculation of the ONS contribution to the soft X–ray background, the presence of the Local Bubble of radius ~ 100 pc surrounding the Sun has been neglected, since the fraction of sample stars that falls within this underdense region turns out to be negligible.

As already discussed in Chapter 1, another fundamental ingredient to investigate the detectability of ONSs is the knowledge of the region of the electromagnetic spectrum in which they emit the bulk of their energy. In the previous section we have calculated the spectra produced in the LTE atmosphere surrounding a NS accreting at low rates and here we will use these results to investigate the detectability issue of ONSs. We will consider also another possibility: since a relic magnetic field is likely to be present, the accretion flow can be channeled into the polar caps and, if we neglect all the radiative effects produce by the magnetic field (on this regard see e.g. Miller 1992; Shibanov *et al.* 1992; Nelson et *et al.* 1995), the main consequence is to limit the size of the emitting region by a factor $A_c/2\pi r_*^2$, where $A_c = \pi r_*^3/r_A$ is the area of the polar cap and r_A is the Alfvén radius. As discussed in Chapter 1, this fact will produce a hardening of the spectrum with respect to the unmagnetized case with the same luminosity, since the flux emitted per unit surface is $F_{mag} = L/2A_c > F_{unmag} = L/4\pi r_*^2$.

3.4.1 Observability of individual sources

A star of luminosity $\overline{L}$ (i.e. moving at $v = \overline{v}$) can be observed up to a maximum distance d_{max} at which the count rate

$$N = \int_0^\infty \frac{1}{h\nu} \frac{L_\nu}{4\pi d^2} e^{-\sigma_\nu N_H} A_\nu \, d\nu \qquad (3.25)$$

becomes lower than the sensitivity limit of the detector S. In equation (3.25), d is the distance of the source, σ_ν is the absorption cross–section (Morrison & McCammon 1983) and N_H the column density of the ISM, A_ν the detector effective area. In the following we will refer to the PSPC on board ROSAT (the response curves for A_ν have been taken from the ROSAT guide for observers). Due to the combined differential

effects introduced by the response of the detector and the absorption of the ISM, this analysis crucially relies on the spectral shape of the radiation emitted by the NS.

The total number of ONSs which can be observed within a certain distance d_{max} is the sum of all the objects with luminosity $L \geq \overline{L}$ (i.e. moving at $v \leq \overline{v}$)

$$N_{ons} \left(\leq d_{max}, \leq \overline{v} \right) = \int_0^{\overline{v}} \int_\Omega \int_0^{d_{max}} f(r, b, l, v) r^2 \, dr \, d\Omega \, dv \,, \qquad (3.26)$$

where f is the distribution function of ONSs and r is the radial distance from the Sun. Here, we assume a uniform medium and treat n_H as a free parameter. Obtaining a reliable statistical sample of objects in the local region near the Sun from the evolution of f would require prohibitively high computational times. Since the ONSs which have reasonable chances to be detected are those in the vicinity of the Sun, we tried to minimize the effects of the small number of local objects introducing a suitable approximation to equation (3.26), based on the hypothesis of a local uniform spatial distribution (details are given in Zane *et al.* 1995).

Results are presented in table 3.2 for typical values of the luminosity and the density of the ISM and taking into account also for the possible presence of a magnetic field $B = 10^9$ G. ONSs with $z \geq z_{ISM} \simeq 300$ pc are assumed not to accrete. The numbers in brackets refer to a black body emission at the star effective temperature and are shown for comparison. Calculations have been repeated for two values of the sensitivity limit of ROSAT, $S_1 = 1.5 \times 10^{-2}$ counts s^{-1} and $S_2 = 10^{-3}$ counts s^{-1}, which roughly correspond to the thresholds of the All Sky Survey (ASS) and the Deep Exposure (DE). As can be seen, the maximum detectability distances obtained using our computed spectra are systematically greater (up to a factor 2–3) than the black body ones, owing to the hardness of the spectrum. We obtain that, for luminosities $l \sim 10^{-8}$, at the sensitivity limit of the ASS ONSs should be detectable up to distances $\sim 200 - 300$ pc even in the absence of magnetic fields. This result is of the order of TC estimates for polar cap accretion and shows that, due to the form of the computed spectrum, ONSs may be observable even if unmagnetized and that the extreme softness of the

Table 3.2

$\frac{L}{L_{Edd}}$	n_H	$\bar{v}$	d^a_{max}	N^a_{ons}	d^b_{max}	N^b_{ons}
	cm^{-3}	km s^{-1}	pc		pc	
$B = 0$						
10^{-7}	0.2	9.9	525 (375)	260 (132)	1170 (725)	1293 (497)
10^{-7}	0.5	13	360 (240)	333 (148)	845 (425)	1837 (465)
10^{-7}	1	17	275 (165)	253 (55)	675 (275)	2495 (414)
4×10^{-8}	0.2	14	380 (220)	402 (135)	840 (445)	1965 (552)
4×10^{-8}	0.5	19	265 (145)	312 (51)	555 (275)	2324 (570)
4×10^{-8}	1	23	195 (105)	262 (41)	415 (185)	2737 (544)
$B = 10^9$ G						
10^{-7}	0.2	9.5	760 (705)	480 (413)	2480 (2110)	5112 (3700)
10^{-7}	0.5	13	685 (595)	1069 (802)	2055 (1675)	9563 (6353)
10^{-7}	1	16	615 (515)	1823 (1279)	1690 (1330)	13769 (8528)
3×10^{-8}	0.2	15	410 (385)	611 (539)	1350 (1060)	6630 (4088)
3×10^{-8}	0.5	20	370 (305)	1345 (914)	1160 (845)	13224 (7017)
3×10^{-8}	1	25	340 (260)	2382 (1393)	990 (695)	20128 (9954)

[a] All Sky Survey sensitivity limit: $S_1 = 1.5 \times 10^{-2}$ counts s^{-1}
[b] Deep Exposure sensitivity limit: $S_2 = 1 \times 10^{-3}$ counts s^{-1}
$N_{tot} = 5.5 \times 10^8$

X–ray spectrum could be a wrong criterion for selecting ONSs. Another relevant result is that, if a magnetic field $B = 10^9$ G is taken into account, the maximum distance at which ONSs can be observable is 1.5–2.5 times the corresponding distance for the unmagnetized case and about 10 sources per square degree should be observable at the DE sensitivity limit; this value is 10 times larger than the estimates by TC.

From a direct analysis of the on line catalogue of the ROSAT PSPC pointings (ROSATSRC), we found that the mean number of sources detected with flux larger

than 10^{-3} counts s^{-1} is $\sim$ 30–40 deg^{-2}. This result is formally in agreement with the mean number of ONSs predicted by our model at the same flux limit, $\sim$ 10 deg^{-2}, although we are aware that the ratio of ONSs over the total number of sources is relatively high. This fact could require a reconsideration of the presently adopted assumptions.

A very promising environment for the detection of ONSs are the nearby Giant Molecular Clouds, where the density of the ISM is sufficiently high for a single NS to emit a considerable amount of radiation (BM; Colpi, Campana & Treves 1993). However, in this case also the absorption of the ISM will be enhanced and the possibility of detection will crucially rely on the delicate balance between the emitted luminosity and the absorbed flux. We have analyzed the 18 Clouds already considered by Colpi, Campana & Treves (where all the relevant parameters are quoted; see also Dame *et al.* 1987). Since density is much higher than the average value of the ISM, we repeated the calculation of the detectable number of ONSs, assuming that all of the absorption is due to the gas in the Cloud. Results are summarized in table 3.3, where a typical luminosity $l \sim 10^{-7}$ and the possible presence of a magnetic field $B = 10^9$ G have been considered. As can be seen from the table, even for the unmagnetized case more than half of the clouds have count rates above the DE sensitivity limit. Confirming previous estimates (Colpi, Campana & Treves 1993), Clouds 5–7 and 9–13 represent the most favorable sites for the observability. At present, we are analyzing the data from the pointings of the ROSAT satellite in the direction of two Molecular Clouds (Cygnus Rift and Cygnus OB7) of this sample to see whether any ONSs can be detected within them (Belloni & Zampieri 1995).

3.4.2 Contribution to the soft X–ray background

Recently Hasinger *et al.* (1993), performing an analysis of the X–ray emission detected by ROSAT in 27 selected high–latitude pointings, found that the number density of resolved sources (413 deg^{-2}) exceeds by $\sim$ 60% the number density of quasars predicted by a standard evolutionary scenario (see also Comastri *et al.* 1995) and that

Table 3.3

		Cloud Name	d_c pc	R_c pc	n_c cm^{-3}	Count Rate 10^{-3} s^{-1}	v^a km s^{-1}	N^a_{ons}
$B = 0$								
	1	Cloud A	500	20	50	1.6 (2.1×10^{-3})	56	4
	2	Cloud B	300	20	51	4.4 (5.2×10^{-3})	56	4
	3	Cloud C	500	16	67	1.5 (1.5×10^{-3})	62	2
	4	Vul Rft	400	23	61	1.7 (8×10^{-4})	60	5
	5	Cyg Rft	700	67	29	0.3 (8.2×10^{-5})	47	95
	6	Cyg OB7	800	64	29	0.3 (7.4×10^{-5})	47	83
	7	Cepheus	450	45	20	2.3 (4.4×10^{-3})	41	18
	8	Taurus	140	13	134	9.9 (3.1×10^{-3})	78	1
	9	Mon OB1	800	34	40	0.4 (2.2×10^{-4})	52	15
	10	Orion A	500	27	84	0.5 (8.5×10^{-5})	67	12
	11	Orion B	500	31	56	0.8 (2.4×10^{-4})	58	13
	12	Mon R2	830	32	36	0.5 (3.9×10^{-4})	50	10
	13	Vela Sheet	425	26	46	1.8 (1.3×10^{-3})	55	7
	14	Cham	215	13	44	15.4 (0.24)	54	1
	15	Coalsack	175	8.5	65	24 (0.43)	61	0
	16	G317–4	170	5	203	13.8 (1.7×10^{-2})	90	0
	17	Lupus	170	18	53	14.8 (2.3×10^{-2})	57	3
	18	Rcr A	150	7.6	68	34.9 (0.81)	62	0
$B = 10^9$ G								
	1	Cloud A	500	20	50	20.5 (12.4)	54	3
	2	Cloud B	300	20	51	56.4 (33.9)	54	3
	3	Cloud C	500	16	67	19.7 (11.7)	59	2
	4	Vul Rft	400	23	61	26.2 (14.4)	58	5
	5	Cyg Rft	700	67	29	6.7 (3.3)	45	78
	6	Cyg OB7	800	64	29	5.3 (2.7)	45	68
	7	Cepheus	450	45	20	26.7 (16.6)	40	18
	8	Taurus	140	13	134	180 (94.1)	75	1
	9	Mon OB1	800	34	40	6.7 (3.7)	50	12
	10	Orion A	500	27	84	11.5 (5.4)	64	10
	11	Orion B	500	31	56	14.4 (7.4)	56	13
	12	Mon R2	830	32	36	6.9 (4)	48	10
	13	Vela Sheet	425	26	46	25.7 (14.8)	52	7
	14	Cham	215	13	44	140 (96)	52	1
	15	Coalsack	175	8.5	65	220 (150)	59	0
	16	G317–4	170	5	203	180 (110)	86	0
	17	Lupus	170	18	53	180 (110)	55	2
	18	Rcr A	150	7.6	68	300 (210)	60	0

the flux produced by extragalactic sources is only $\sim 40\%$ of the total flux measured in the 0.5–2 keV band (2.47×10^{-8} erg cm^{-2} s^{-1} sr^{-1}). Although this excess could be explained in terms of a different quasars evolutionary scenario, another interesting possibility is that the observed soft emission could be produced by a new population of sources. Very recently Maoz & Grindlay (1995) showed that the observed data for the unresolved soft XRB can be accounted for invoking the presence of a galactic population of objects, which they have tentatively identified with Cataclysmic Variables; using the hypothesis of black body spectrum at the star effective temperature, ONSs were ruled out because of their too soft emission. Here we reconsider the issue in light of the fact that our computed spectra for accreting ONSs show a significant hardening with respect to a black body and that the possible presence of a magnetic field tends to make the emission even harder.

The contribution to the soft XRB by accreting ONSs is calculated summing the fluxes per unit solid angle emitted by all the population of objects in the Galaxy

$$\left\langle \frac{dI}{d\Omega} \right\rangle = \frac{1}{4\pi} \int_0^\infty \int_\Omega \int_0^{r_{max}} f\left(r, b, l, v\right) \frac{\tilde{L}_x}{4\pi r^2} r^2 \, dr \, d\Omega \, dv \, , \qquad (3.27)$$

where the integrals in r, Ω span the entire Galaxy and $\tilde{L}_x$ is the source luminosity in the 0.5–2 kev band, corrected for interstellar absorption. As far as the number of resolved sources is concerned, we repeated the calculation of the integral (3.26), where now d_{max} is the maximum distance at which a star of luminosity ℓ produces a count rate above the threshold of Hasinger *et al.* (estimated to be $\sim 2 \times 10^{-4}$ counts s^{-1}), the integral is extended to all velocities and the result is divided by 4π to calculate the projected number density of sources.

The results of our calculations are presented in table 3.4. Similarly to the finding of MG and BM, for the unmagnetized case the ONS contribution to the XRB is negligible, although the flux is almost 40 % larger than that estimated by BM. However, for polar cap accretion, it turns out that 10% of the observed XRB could be explained in terms of emission from ONSs and 5% of the total number of resolved sources would be ONSs. In

Table 3.4

	$\left\langle \frac{dI}{d\Omega} \right\rangle^a$	$\left\langle \frac{dN}{d\Omega} \right\rangle^b$	$\frac{\langle dI/d\Omega \rangle}{\mathrm{F_{XRB}}}{}^c$	$\frac{\langle dN/d\Omega \rangle}{\mathrm{N_{XRB}}}{}^d$
$B = 0$				
	6.3×10^{-11}	0	$2.5 \times 10^{-3}\%$	0
$B = 10^9$ G				
all b	2.4×10^{-9}	22	9.8%	5.3%
$|b| \geq 30°$	1.3×10^{-9}	6	5.2%	1.4%
$|b| \leq 30°$	3.6×10^{-9}	38	14.5%	9.2%

a $\mathrm{erg\,cm^{-2}s^{-1}sr^{-1}}$

b $\mathrm{sources\,deg^{-2}}$

c $F_{XRB} = 2.47^{-8}\ \mathrm{erg\,cm^{-2}s^{-1}sr^{-1}}$

d $N_{XRB} = 413\ \mathrm{sources\,deg^{-2}}$

order to quantify the degree of anisotropy, the calculations for polar cap accretion have been repeated for objects with high ($|b| \geq 30°$) and low ($|b| \leq 30°$) galactic latitude. The first case allows a closer comparison with Hasinger *et al.* and MG. As can be seen from the table, the ratio of the X–ray flux emitted by objects below and above 30° is about 2–3. This degree of anisotropy is not in contrast with the observed near isotropy of the XRB (McCammon & Sanders 1990) since ONSs can contribute at most to 25% of the soft excess.

The strongest constraint to our results derives from the expected number of sources above 10^{-3} counts s^{-1} (see section 3.4.1) and this will determine the importance of the ONSs contribution to the X–ray background. Actually, the contribution of ONSs would scale as the percentage of sources which will be identified as ONSs. We note that our results are not strongly dependent on the overall shape of the velocity distribution of ONSs, but only on the number of objects in the low velocity tail, here calculated using the Narayan & Ostriker distribution function. However, one should keep in mind that the distribution in the low velocity tail of ONSs remain very uncertain; in fact, in addition to the possibility that the distribution could be much more depleted of low

velocity objects than that of Narayan & Ostriker (Lyne & Lorimer 1994), it can also be affected by dynamical heating, as suggested by Madau & Blaes (1994). This process, observed in the local disk star population, causes the velocity dispersion to increase with age as a consequence of scattering by molecular clouds and spiral arms (Wielen 1977). If ONSs participate the same process, dynamical heating over the lifetime of the Galaxy may scatter a fraction of low velocity stars to higher speeds. This could have a major effect on the source number counts (that can be decreased up to a factor 10) and it may reduce the contribution of luminous ONSs to the background. Other factors of indetermination, like the poor knowledge about the NSs birth rate, and hence, of their present total number, may affect our conclusions to the same extent. In addition, present estimates of the magnetic field of ONSs are subject to various uncertainties. We conclude that, even if Neutron Stars do not account completely for the characteristics of the galactic population proposed by Hasinger et al. (1993) and MG, their contribution may be of importance.

CHAPTER 4
TIME–DEPENDENT ANALYSIS OF SPHERICAL ACCRETION ONTO BLACK HOLES

In this chapter results are presented from a time–dependent, numerical investigation of spherical accretion onto black holes, within the framework of relativistic radiation hydrodynamics. We have studied the stability of self–consistent, stationary solutions of black hole accretion with respect to thermal and radiative perturbations and also the non–linear evolution of unstable, high temperature models, heated by the high–temperature radiation produced by the accretion flow itself in the inner region near to the horizon. In some cases, a hydrodynamic shock forms at around 10^3–10^4 Schwarzschild radii, where Compton heating exceeds radiative cooling. The calculations were made using a suitably designed radiation hydrodynamics code, in which radiative transfer is handled by means of the PSTF moment formalism and which contains an original treatment of the radiation temperature equation.

4.1 INTRODUCTION

Stationary, spherical accretion onto black holes is a well–known and extensively studied topic. Starting from the seminal paper by Bondi (1952), many papers have been devoted to the analysis of spherical accretion under a variety of conditions, mainly in order to obtain a definite estimate of the efficiency of the process. In contrast with accretion onto neutron stars, the efficiency is not fixed by the requirement that all the gravitational potential energy of the accreting gas must be converted into radiation, since no rigid surface exists which can stop the flow. Matter can cross the horizon carrying a substantial fraction of the gravitational potential energy liberated and the efficiency of the process is determined solely by the effectiveness of the radiative processes in converting the internal energy of the accreting gas into radiation, as first noted

by Shvartsman (1971). As shown by many authors (see e.g. Michel 1972; Novikov & Thorne 1973; Blumenthal & Mathews 1976; Begelman 1978; Brinkmann 1980), the flow properties are fixed once the accretion rate is specified, so that stationary solutions can be completely characterized by their position in the $(\dot{m}, l)$ plane, where $\dot{m}$ and l are, respectively, the accretion rate and luminosity in Eddington units. Stationary spherical accretion onto black holes was investigated in detail by Nobili, Turolla & Zampieri (1991, hereafter NTZ); figure 4.1 shows the $(\dot{m}, l)$ diagram for the complete set of their solutions. At low accretion rates ($\dot{m} < 1$), spherical accretion is very inefficient in converting gravitational energy into radiation since the density is too low for cooling processes to be effective; the emitted luminosity is also very low (lower branch in figure 4.1, hereafter the LL branch). These models are essentially adiabatic and have very high temperatures (see also Shapiro 1973a). In this regime, the only possibility for increasing the efficiency of the accretion process is related to the presence of magnetic fields, which can cause strong dissipation (e.g. through reconnection of field lines) and induce strong emission of synchrotron radiation (Shapiro 1973b; Mèszàros 1975). Soffel (1982) studied in some detail the transition from the optically thin regime to the optically thick one: as $\dot{m}$ increases, the cooling processes become more effective and the gas temperature decreases, causing in turn a decrease in the total emitted luminosity (with a local minimum at around $\dot{m} \simeq 0.1$). For higher values of the accretion rate, free–free absorption is no longer negligible and the gas becomes optically thick in the inner region near to the horizon of the black hole. The temperature increases because heating exceeds cooling and also the luminosity rises since radiation is in LTE with the gas in the inner core. Preliminary investigations of spherical accretion in the diffusion regime were made by Tamazawa *et al.* (1974), Maraschi, Reina & Treves (1974), Kafka & Mészáros (1976), Vitello (1978), Begelman (1979), Gillman & Stellingwerf (1980) and Freihoffer (1981), while a complete treatment was finally given by Flammang (1982, 1984), who showed the existence of a subcritical point related to the equation for the radiative luminosity. When $\dot{m} > 1$, the inner core starts to be optically thick to elec-
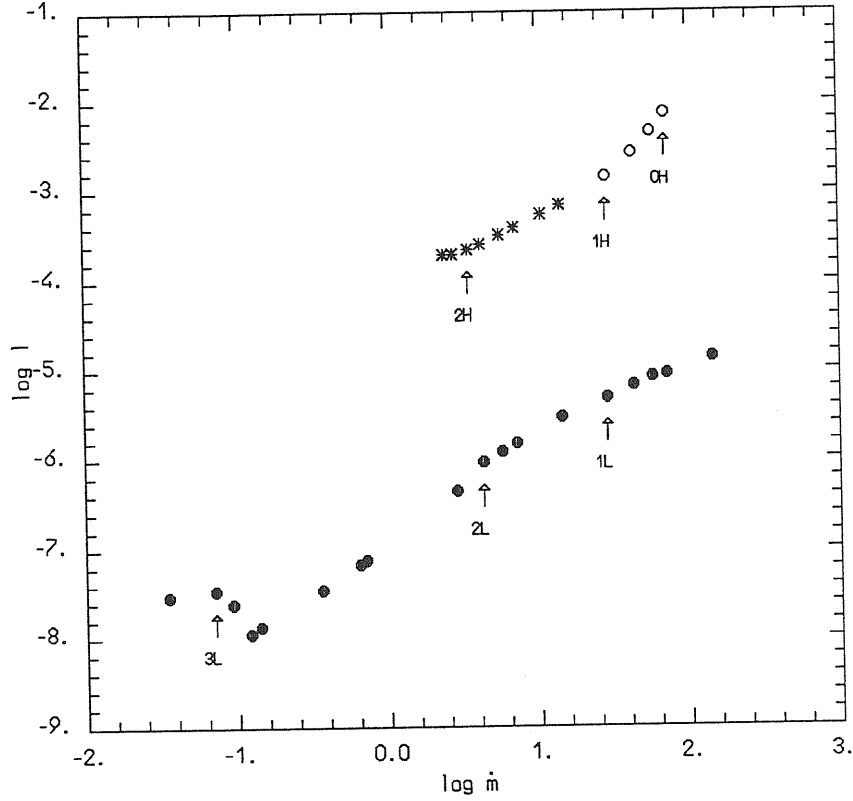
Figure 4.1 – The $(\dot{m}, l)$ diagram for the complete set of stationary solutions found by NTZ (circles). Also shown are the 6 initial models whose relevant parameters are listed in table 4.1. Filled circles mark the stable LL stationary solutions, while open circles denote the unstable HL models. Asterisks indicate the low $\dot{m}$ HL solutions, which might still be unstable, but on much longer time–scales.

tron scattering as well. Stationary, spherical accretion onto black holes with $\dot{m} \gg 1$ has been studied by Blondin (1986). In this regime, a trapping radius appears (Rees 1978; Begelman 1978), below which all of the radiative energy is advected into the black hole, since the outward diffusion velocity of the photons is smaller than the inward velocity of the accretion flow. This makes the process less efficient and the rate of increase of luminosity with $\dot{m}$ becomes slower.

For $3 \lesssim \dot{m} \lesssim 100$, there is also another class of solutions, characterized by hav-

ing high temperatures and luminosities (upper branch in figure 4.1, hereafter the HL branch). These are dominated by the effects of comptonization which keeps the gas and radiation temperatures almost equal in the inner part of the flow where the density is sufficiently high to make the Compton parameter very large. In the intermediate region between 10^2 and $10^5 \, r_g$ (where r_g is the Schwarzschild radius of the black hole), Compton heating dominates and the only competitive cooling mechanism is free–free emission. The first authors to investigate the possible existence of high luminosity solutions were Wandel, Yahil & Milgrom (1984) and Park (1990a,b), who performed a detailed study of spherical accretion for a large range of accretion rates and considered also a two–temperature model with pair production. High luminosity stationary solutions have relatively high efficiency and appear to exist only for a very definite range of accretion rates. Already in 1976, Ostriker and collaborators (Ostriker *et al.* 1976) pointed out that, because of the non–local nature of comptonization, the heating produced in the flow by the high–temperature radiation coming from the inner region can increase the gas temperature in such a way that the internal energy density becomes larger than the gravitational energy density and the accretion process is then stopped. This effect is called *preheating*. Later on, Cowie, Ostriker & Stark (1978), Shull (1979), Stellingwerf & Buff (1982) and Krolik & London (1983) showed that preheating is very important in placing limits on the region of parameter space within which HL solutions for black hole accretion can exist, although the strength of preheating is reduced if Compton cooling is taken into account (see e.g. Bisnovatyi–Kogan & Blinnikov 1980). As shown by NTZ, preheating *at* the sonic point for the matter prevents the existence of high luminosity solutions with $\dot{m} \lesssim 3$, while preheating *within* the sonic radius prevents the existence of stationary solutions for $\dot{m} \gtrsim 100$. The stability of these solutions remains a completely open question and represents the main goal of the present study. The first attempt to investigate the stability of isothermal accretion was made by Stellingwerf & Buff (1978) using an Eulerian scheme, based on an extension of the Henyey relaxation method. They found that transonic accretion is quite stable. By means of a general relativistic

analytical calculation, Moncrief (1980) showed that, for isentropic flows, no unstable normal modes exist which extend outside the sound horizon. The first studies including the heating and cooling terms due to the presence of the radiation field (Cowie, Ostriker & Stark 1978; Stellingwerf & Buff 1982; Stellingwerf 1982) were devoted to analysing the effect of preheating on the stability of the accretion flow and to defining the region of the $(\dot{m}, l)$ plane where the existence of stationary solutions is not allowed. In particular, Stellingwerf (1982) presented a local stability analysis of optically thin, X–ray heated accretion flows and showed that, for sufficiently high luminosities, a finite amplitude drift instability can develop, due to the form of the free–free cooling function, causing a time–dependent behaviour of the solution on a time–scale ranging between a day and a few tens of days. Krolik & London (1983) used the WKB method to derive the dispersion relation for modes coupling density, temperature and velocity perturbations in an optically thin, accreting gas and found that, although stationary solutions with high temperature and luminosity can exist, heating of the gas inside the sonic radius leads to the onset of a thermal instability in a large region of the $(\dot{m}, l)$ plane. Gilden & Wheeler (1980) and Vitello (1984) investigated time–dependent, optically thick accretion within the framework of General Relativity, treating the radiation field in the diffusion approximation and using two different numerical schemes: a Lagrangian hydrodynamic code in the first case and a Linearized Block Implicit Algorithm in the second one. They found that, within this approximation, no matter which initial conditions the code started from, convergence toward stationary LL solutions was rapidly achieved, showing that they are intrinsically stable. Finally, NTZ, using an argument originally suggested by Nobili, Calvani & Turolla (1985) and based on Prigogine's criterion, argued that HL solutions might be unstable because of the large value of the entropy production rate.

Despite the fact that the stationary problem has been extensively investigated, mainly for shedding light on the efficiency of the radiation generation, we think that several aspects require further consideration such as, for instance, investigating the stability properties of the high luminosity solutions and searching for the existence and

non–linear evolution of possible heated or shocked models. In this chapter we present an analysis of the stability and time–dependent behaviour of the solutions for spherical accretion onto black holes within the framework of general relativistic radiation hydrodynamics.

4.2 THE MODEL

In the following, we will consider spherical accretion of a self–gravitating hydrogen gas in the gravitational field of a non–magnetized, non–rotating black hole. The basic equations have been presented in Chapter 1 (section 1.1.2). The radiation hydrodynamic equations (1.35)–(1.41), together with the first two moment equations (1.42) and (1.43) need to be supplemented with the constitutive equations for the gas, the expressions for the source moments, a prescription for the closure function and suitable boundary conditions. Stationary, spherical accretion onto black holes has recently been investigated in detail by NTZ. The main goal of the present analysis is to ascertain the stability properties of the solutions found by NTZ; in particular, we want to study the behaviour of the models in a certain range of accretion rates, for which both low and high luminosity solutions exist. To allow a direct comparison of our results with those of NTZ, we will adopt the same input physics which they considered.

If the dominant radiative processes are free–bound, free–free and isotropic scattering, the radial source moments s_0 and s_1 can be written (see equations (1.30) and (1.31))

$$s_0 = \rho \left(\bar{\epsilon}_{fb} - k_0 w_0 \right) + k_{es} \rho w_0 \frac{4KT}{m_e c^2} \left(1 - \frac{T_\gamma}{T} \right) , \qquad (4.1)$$

$$s_1 = -\rho k_1 w_1 , \qquad (4.2)$$

where $c\bar{\epsilon}_{fb}$ is the emissivity per unit mass per unit time, k_0, k_1 and k_{es} are the absorption, flux–mean and scattering opacities, respectively, and T_γ is the radiation temperature, defined in equation (1.32). As discussed in Chapter 1, the second term on the right hand side of equation (4.1) accounts for the energy exchange between matter and

radiation due to non–conservative scatterings and is obtained by integrating the Kompaneets equation over frequency and neglecting the non–linear term which describes induced emission. Since it is derived in the Fokker–Planck approximation, this term is certainly not adequate for describing the interaction between photons and electrons when the latter become relativistic, as happens in some of the solutions which we have computed. However, even in this case, the model can give a good qualitative indication of the correct results. We have expressed the emissivity using the interpolation of the cooling function Λ given by Stellingwerf & Buff (1982)

$$\bar{\epsilon}_{fb} = \frac{\rho\Lambda}{m_p^2 c} \, , \tag{4.3}$$

$$\Lambda = \left[\left(1.42 \times 10^{-27} T^{1/2} \beta_{rel} + 6.0 \times 10^{-22} T^{-1/2} \right)^{-1} + \right.$$

$$\left. + 10^{25} \left(\frac{T}{15,849 K} \right)^{-12} \right]^{-1} \quad \mathrm{erg\ cm^3\ s^{-1}} \, ,$$

$$\beta_{rel} = \left(1 + 4.4 \times 10^{-10} T \right) \, ,$$

which includes bound–bound, free–bound, e–p and e–e bremsstrahlung for a pure hydrogen gas; the factor β_{rel} is a relativistic correction. Assuming LTE between emitters and absorbers, we can use the Kirchhoff law to obtain the Planck mean opacity, $k_P = \bar{\epsilon}_{fb}/a_R T^4$, where a_R is the blackbody radiation constant. Since the actual spectral distribution of the radiation energy density is not known in a frequency–integrated calculation, we use k_P in place of the absorption opacity k_0. The flux–mean opacity k_1 can be split into two terms: the first is the scattering opacity k_{es} and the second is the sum of the contributions from all of the other radiative processes; however, since k_{es} is always dominant for the range of densities and temperatures encountered in the present problem, we have approximated the additional term using the Rosseland mean k_R calculated taking into account only free–free processes

$$k_1 \simeq k_{es} + k_R \, , \tag{4.4}$$

$$k_R = 6.4 \times 10^{22} \rho T^{-7/2} \quad \text{cm}^2 \text{ g}^{-1} \, .$$

Finally, we need to specify the constitutive equations for a pure hydrogen gas

$$P = [1 + x(T)] \frac{\rho K T}{m_p} \, , \tag{4.5}$$

$$e = \rho c^2 \left\{ 1 + \frac{3}{2} [x(T) + x^*(T)] \frac{KT}{m_p c^2} - [1 - x(T)] \frac{E_H}{m_p c^2} \right\} \, , \tag{4.6}$$

where T is the gas temperature, $E_H = 13.6$ eV is the hydrogen ionization potential and $x(T)$ is the degree of ionization, computed by equating the collisional–ionization and radiative–recombination rates (Buff & McCray 1974) and expressed using the interpolation formula of Stellingwerf and Buff (1982)

$$x(T) = \frac{F}{1 + F} \, , \tag{4.7}$$

with

$$F = 2 \left(\frac{T}{1 \text{ K}} \right) \exp \left(\frac{-1.58 \times 10^5 \text{ K}}{T} \right) \, .$$

In equation (4.6)

$$x^*(T) = \frac{2}{3} \left[\theta^{-1} \left(\bar{\eta} - 1 \right) - 1 \right] \, , \tag{4.8}$$

where $\theta = KT/m_e c^2$ and $\bar{\eta} = K_3(\theta^{-1})/K_2(\theta^{-1})$ (K_n is the modified Bessel function of order n). A polynomial fit by Service (1986) was used to calculate $\bar{\eta}$, giving an accuracy of a few parts in 10^5. The third term inside the curly brackets in equation (4.6) accounts for the electrostatic potential energy of bound electrons in the neutral hydrogen atoms.

The constitutive equations (4.5) and (4.6) can be used to express two fluid variables in terms of the other ones. Since the values of the temperature T and the density ρ are needed for evaluating the source moments s_0 and s_1, it is more convenient to use them in the hydrodynamic equations and to calculate e and P from equations (4.5) and (4.6). Inserting equations (4.5) and (4.6) into equation (1.35), the Energy equation can be written in the form

$$\left[\frac{3}{2} (x + x^*) + \left(\frac{3}{2} + \frac{E_H}{k_B T} \right) \frac{dx}{d \ln T} + \frac{3}{2} \frac{dx^*}{d \ln T} \right] \frac{k_B T}{m_p c^2} \frac{T_t}{T} + \frac{P}{c^2} \left(\frac{1}{\rho} \right)_t + \frac{a s_0}{c \rho} = 0 \, . \tag{4.9}$$

As far as the closure function is concerned, in the present calculation we chose to relate w_2 to w_0 using the following expression

$$f = \frac{w_2}{w_0} = \frac{2}{3} \left[1 + \left(\frac{\tau}{\tau_0} \right)^n \right]^{-1} , \qquad (4.10)$$

where τ_0 and n are free parameters. We made several trials with different expressions for f and found that the fractional difference between solutions obtained with different reasonable closures turns out to be no larger than ~ 20 %, which is acceptable here. In fact, a change in the closure parameters was used to perturb the initial stationary solution, as we will discuss later.

4.2.1 Equation for the Radiation Temperature

In the frequency–integrated transfer problem, the radiation temperature T_γ cannot be directly computed from its definition (equation (1.32)). However, since T_γ appears only in the term in s_0 which accounts for comptonization, it only becomes important when the energy exchange between matter and radiation due to non–conservative scatterings starts to be effective. In a medium at rest, the fractional change of the mean photon energy ($E = 4KT_\gamma$) because of scatterings with a thermal, non–relativistic distribution of electrons, follows the relation

$$\frac{dE}{E} = \frac{4KT}{m_e c^2} \left(\frac{E}{4KT} - 1 \right) \alpha d\tau ,$$

(Rybicki & Lightman 1979; Wandel, Yahil & Milgrom 1984) where τ is the scattering depth, $4KT(E/4KT - 1)/m_e c^2$ is the mean energy change per scattering and $\alpha d\tau$ is the mean number of scatterings which a photon undergoes between τ and $\tau + d\tau$, with

$$\alpha = 1 \qquad \text{for } \tau < 1 ,$$

$$\alpha = 2\tau \qquad \text{for } \tau > 1 .$$

From the computational point of view, it is convenient to write an equation for T_γ which is valid over all of the integration domain with continuous coefficients; for this reason the

previous equation is usually written in the following form, which is an approximation near to $\tau \simeq 1$ (Park & Ostriker 1989; Park 1990a):

$$\frac{d\ln T_\gamma}{d\ln \tau} = 2Y_c \left(\frac{T_\gamma}{T} - 1\right) , \qquad (4.11)$$

where $Y_c = 4KT \max(\tau, \tau^2)/m_e c^2$ is the Compton parameter. In stationary calculations, this equation has been used directly to give the variation of T_γ with r, at Eulerian constant time $\tilde{t}$, but for non–stationary flows it is not satisfactory to integrate it along the time–slice (i.e. at constant Lagrangian time t) as this would imply an infinite speed of propagation of information. Instead, we apply it along the outward–pointing characteristics of the radiation field, $\mu_c(t)$ (defined from the moment equations (1.42) and (1.43)), and calculate the optical depth τ along the same lines using

$$\tau = \int_\mu^\infty k_{es}\rho b\Gamma d\mu . \qquad (4.12)$$

This seems a reasonable choice because the radiation temperature is strictly related, by definition, to the radiation energy density and we expect that information will propagate along the characteristic lines of the radiation field. In this case it is not difficult to show (see Appendix B, equation (B5)) that

$$\frac{\partial T_\gamma}{\partial t} = -a\Gamma v_c \left[\frac{2k_{es}\rho Y_c}{\tau} T_\gamma \left(\frac{T_\gamma}{T} - 1\right) + \frac{1}{b\Gamma}\frac{\partial T_\gamma}{\partial \mu}\right] , \qquad (4.13)$$

where $v_c = b\dot{\mu}_c/a = (f + 1/3)^{1/2}c$ is the characteristic velocity for the radiation field and $\dot{\mu}_c = d\mu_c/dt$. This is the actual form of the equation for T_γ used in our calculations. Equation (4.13) applies when comptonization is the dominant radiative process and also gives the correct behaviour (outgoing wave) when non–conservative scattering becomes inefficient as long as true emission and absorption can be neglected. For the HL models, true absorption is never dominant and true emission is never likely to significantly affect T_γ and so the use of equation (4.13) is always satisfactory. For the LL models, true emission and absorption *are* dominant but in this case the second term on the right hand side of equation (4.1) is small compared with the other terms and an accurate

evaluation of T_γ is no longer needed. The stationary limit of equation (4.13) (see again Appendix B, equation (B8)) is

$$\left(1 + \frac{uc}{\Gamma v_c}\right) \frac{\partial T_\gamma}{\partial r}\bigg|_{\tilde{t}} = -\frac{2k_{es}\rho Y_c}{\tau} T_\gamma \left(\frac{T_\gamma}{T} - 1\right), \qquad (4.14)$$

where the partial derivative is taken at constant Eulerian time $\tilde{t}$. In this form, the presence of a critical point where $u = -\Gamma v_c/c$ is made apparent. We note that this result is a consequence of the finite velocity of propagation in equation (4.13); in fact, as is well–known, the presence of critical points in the hydrodynamic equations for stationary flows is a relic of the characteristic velocity of the corresponding time–dependent equations. This result represents the main difference between the form of the T_γ equation used here and the one considered in all previous studies of this problem in the framework of black hole accretion (Park & Ostriker 1989; Park 1990a; NTZ).

4.2.2 Boundary Conditions

From the mathematical point of view, the equations of radiation hydrodynamics (1.36)–(1.41) and (4.9), the first two moment equations (1.42) and (1.43) and the radiation temperature equation (4.13) form a hyperbolic system. In order for the problem to be well–posed, we need to specify values for all of the variables at some initial time $t = t_0$ over all of the integration domain $\mu_{in} \leq \mu \leq \mu_{out}$ and also to assign suitable boundary conditions at the spatial boundaries μ_{in}, μ_{out}. The number of boundary conditions needed depends on the sign of the eigenvalues of the characteristic equations at each boundary. At the outer boundary, negative eigenvalues signify that information is propagating into the integration domain from outside and a corresponding number of conditions must be assigned; the same is true for positive eigenvalues at the inner boundary. In the present case it can be shown that we need to prescribe 7 boundary conditions (4 at the inner boundary and 3 at the outer boundary) as follows: 2 conditions related to the fluid equations, 2 related to the moment equations, 1 each for the equations for T_γ, a and M. As far as the fluid boundary conditions are concerned, we

set a floating boundary (extrapolation in r) for u at $\mu = \mu_{out}$; at $\mu = \mu_{in}$, we dropped the pressure gradient term from the Euler equation, making it advective in form and assuming strict free–fall very near to the black hole horizon. The inner conditions on T_γ and w_1 and the outer condition on w_0 were all taken as floating boundaries. The choice of a floating boundary is suitable when one does not want to put any constraint on a variable, leaving it free to adjust itself or to oscillate if there are waves propagating out of the integration domain (as for a vibrating string with free endpoints).

As far as a and M are concerned, the time–slice at constant t is a characteristic direction for equations (1.39) and (1.40) and we put

$$a = 1 \qquad \mu = \mu_{out}, \qquad (4.15)$$

$$M = M_0 \qquad \mu = \mu_{in}. \qquad (4.16)$$

The condition on a, equation (4.15), corresponds to synchronizing coordinate time with the proper time of a comoving observer at the outer edge of the grid. This is also equal to the Eulerian clock time there, if the outer edge of the grid is placed sufficiently far away from the black hole.

Finally, we note that, if the system tends to a stationary limit, the time–dependent equations reduce to their stationary form and the solution which crosses any critical points in a regular way is automatically selected.

4.2.3 Numerical Method

The equations presented in this chapter and in section 1.1.2 have been solved numerically for matter being accreted spherically onto a Schwarzschild black hole, using a Lagrangian finite difference scheme with a standard Lagrangian organization of the grid. The code was adapted from one developed by Miller & Rezzolla (1995) for solution of the equations of radiation hydrodynamics in the context of the cosmological quark–hadron transition. We divided the integration domain (from the black hole horizon at $r = r_g$ out to $10^9 r_g$) into a succession of comoving zones with each one having width $\Delta\mu$

21% larger than the one interior to it. Whenever the inner edge of the innermost zone crosses the horizon (which happens every 4–5 cycles with our time–step constraints), we remove it from the calculation and perform a regridding of all the variables. We followed a regridding procedure previously adopted by Szuszkiewicz & Miller (1995) in connection with the study of disc accretion onto black holes. Originally a cubic spline interpolation was used, but this turned out to produce a numerically unstable evolution in our case. A local cubic interpolation was eventually used instead, which was found to be satisfactory and efficient. At the initial time the effective mass contained within the inner boundary, M_0, is equal to the initial black hole mass M_{bh}, which we take to be $3M_\odot$ as in the stationary calculations. As time elapses, M_0 increases as zones pass through the horizon and are removed from the calculation. However, during a characteristic evolutionary time interval, the mass of the material accreted is small compared with M_{bh}.

To have second–order accuracy in time, u and w_1 are both evaluated at an intermediate time level. They are advanced to the new time level at the end of each cycle after all of the other variables have been calculated. The time–step is adjusted in accordance with the relativistic Courant condition and two additional constraints on the fractional variations of ρ and T in each time–step, which are required to be smaller than 5%. In practice, we found that the time–step is usually limited by the last two conditions due to the fact that the variation of density and temperature, as seen by comoving observers, becomes very rapid near to the horizon where the flow velocity approaches the speed of light. As far as the spatial centering is concerned, ρ, T, w_0, T_γ and a are treated as mid–zone quantities, while r, M, u and w_1 are treated as zone boundary quantities.

Once the finite difference representation has been introduced, equations (1.36), (1.37), (1.39), (1.40) and (1.41) can be solved explicitly for u, ρ, a, M and r, respectively. Where necessary, linear interpolation and extrapolation in time were used to obtain the values of quantities at suitable time levels. The semi–logarithmic derivatives present in the Continuity equation (1.37) and the equation for a (1.39) were solved

using the Crank–Nicholson operator for equation (1.37) and the Leith–Hardy operator for equation (1.39) (see e.g. May & White 1967). For the moment equations (1.42) and (1.43), we adopted a mixed representation: after dividing the first equation by w_0 and the second by w_1 we grouped together the terms in the following way:

$$\frac{(w_0)_t}{w_0} = -\left[\frac{4}{3}\left(\frac{b_t}{b} + 2\frac{r_t}{r}\right) + \left(\frac{b_t}{b} - \frac{r_t}{r}\right)f\right] + \frac{ac}{w_0}\left[s_0 - \frac{1}{a^2br^2}(w_1a^2r^2)_\mu\right], \quad (4.17)$$

$$\frac{(w_1)_t}{w_1} = -2\left(\frac{b_t}{b} + \frac{r_t}{r}\right) + \frac{ac}{w_1}\left[s_1 - \frac{1}{3a^4b}(w_0a^4)_\mu - \frac{1}{abr^3}(fw_0ar^3)_\mu\right], \quad (4.18)$$

where w_2 has been expressed using the closure relation $w_2 = fw_0$ with f being defined as in equation (4.10). The terms on the left hand side of equations (4.17) and (4.18) were treated using the Crank–Nicholson operator, while the quantities appearing on the right hand side were calculated at the correct time level by means of interpolation or extrapolation where necessary. Because the dependence on temperature in the Energy equation is rather sensitive, we adopted a semi–implicit scheme for equation (4.9) using a secant iteration method. The temperature at the new time level is calculated iteratively starting from two initial estimates, based on the value at the previous time–step. Convergence is rapidly achieved in 4–5 iterations. Since s_0 is in general very sensitive to the value of the temperature, the iteration was extended to include also the zero–th moment equation (4.17).

The equation for T_γ (equation (4.13)) presents a particular numerical problem because of the delicate balance between T and T_γ which, following Bowers & Wilson (1991), we treated using a fully implicit differencing for $(T - T_\gamma)$ to achieve numerical stability.

4.3 NUMERICAL RESULTS AND DISCUSSION

We have calculated the time evolution of 6 models, starting from the stationary solutions listed in table 4.1 whose position in the $(\dot{m}, l)$ plane is shown in figure 4.1. Because of the different form of the T_γ equation used here, the present stationary solutions differ slightly from those of NTZ (see equation (4.14) and the following discussion).

Table 4.1 – Characteristic Parameters for Stationary Models.

	$\dot{m}$	l	$\eta_{eff} = l/\dot{m}$
1L	28.5	4.8×10^{-6}	1.7×10^{-7}
2L	4.27	9.2×10^{-7}	2.2×10^{-7}
3L	0.071	3.5×10^{-8}	4.9×10^{-7}
0H	70.8	7.3×10^{-3}	1.0×10^{-4}
1H	28.3	1.4×10^{-3}	5.0×10^{-5}
2H	3.45	2.2×10^{-4}	6.5×10^{-5}

The definitions of relevant time–scales for the present discussion are listed in table 4.2. Along with the dynamical time–scale, t_d (which is the characteristic time for an element of fluid with velocity u to travel a distance r), we have listed also the sound crossing times for the gas, t_{sg}, and for the radiation, t_{sr} (these are defined as the ratio of the radial length scale to the relevant characteristic velocity and represent the time needed for a "sound" wave in the gas or radiation fluid to travel a distance r). For determining whether stationary solutions are stable or not, we should in principle evolve each model for a time comparable with the relevant t_{sg} or t_{sr} in order to allow information to travel from the inner regions to the outer ones. At $10^5 r_g$, $t_{sg} \sim 10^4$ s and $t_{sr} \sim 1$ s. To reach an evolutionary time $t = 10^4$ s would require prohibitively high computational times but in fact, as we shall see, all of the models evolve on a much shorter time–scale (typically of a few seconds) which is mainly determined by the thermal and radiative processes. The thermal balance is regulated by the cooling and heating time–scales, t_c and t_h, which are the ratios of the internal energy of the gas to the cooling rate (C) and heating rate (H), respectively, and are both defined in table 4.2. We have also introduced the thermal time–scale, t_{th}, defined as the ratio of the internal energy of the gas to the net rate of energy input or output for the gas, $|H - C|$.

For each model we started the numerical calculation from an initial perturbed solution which was calculated by changing the closure function. By varying τ_0 and n in

Table 4.2 – Time–scales

$t_d = \frac{r}{uc}$	dynamical time	
$t_{sg} = \frac{r}{v_s}$	sound crossing time for the gas	$v_s = \left(\frac{\partial P}{\partial \rho}\right)^{1/2}\Big|_{entropy}$
$t_{sr} = \frac{r}{v_c}$	sound crossing time for the radiation	$v_c = \left(f + \frac{1}{3}\right)^{1/2} c$
$t_c = \frac{e - \rho c^2 + P}{C}$	cooling time	$C = \rho c \left(\bar{\epsilon}_{fb} + k_{es} w_0 \frac{4 k_B T}{m_e c^2}\right)$
$t_h = \frac{e - \rho c^2 + P}{H}$	heating time	$H = \rho c w_0 \left(k_0 + k_{es} \frac{4 k_B T_\gamma}{m_e c^2}\right)$
$t_{th} = \frac{e - \rho c^2 + P}{|H - C|}$	thermal time	

equation (4.10), we obtained a perturbation of the order of 10–20 % in the gas temperature and in the radiation moments. This way of setting the perturbation was not effective for model 3L, which is optically thin everywhere, and so, only in this case, we decided to evolve the solution without any initial perturbation just to have an indication of the intrinsic stability of these models. The solution after 14 seconds remains exactly in the initial stationary state. This is not surprising since, in this case, we know that cooling is very inefficient and so the result obtained by Moncrief (1980), who found that adiabatic flows are stable, was likely to apply here. In fact, optically thin solutions are not of great interest and we did not spend further time in the numerical analysis of the stability of these models.

In figure 4.2 the results from the numerical calculation for model 1L are shown. This solution is representative of the behaviour of all optically thick LL models. As can be seen from the figure, the solution relaxes toward the stationary state (shown with a continuous line) on a time–scale of the order of t_{th} which, for this solution, is much shorter than 1 second within $10^3 r_g$. This shows that these solutions are stable, in agreement with the result obtained by Vitello (1984). The perturbation does not directly involve velocity and density, which remain essentially equal to their initial values and the accretion rate also remains extremely constant. Radiation and gas pressure have negligible effect in these cases and matter is essentially in free–fall from the sonic radius
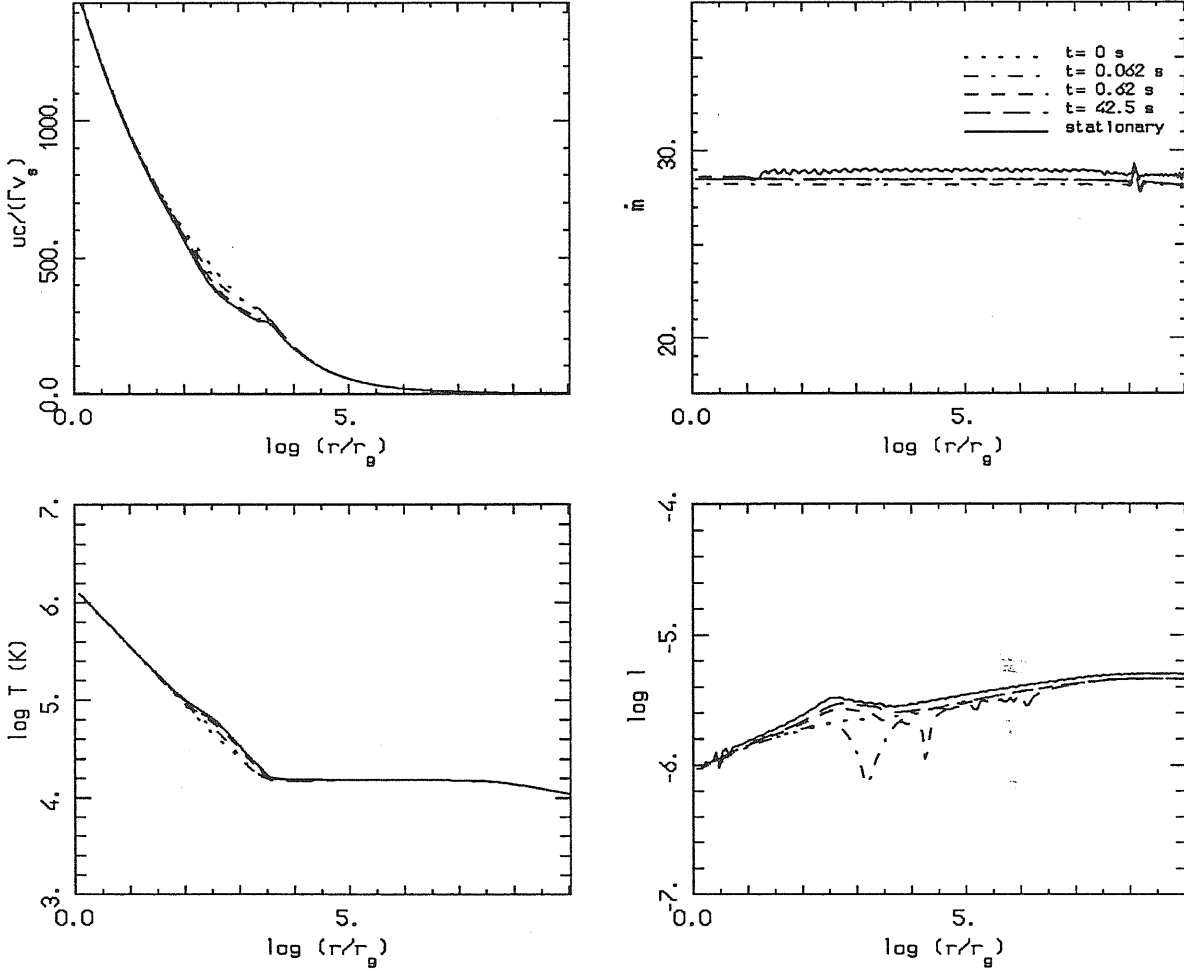
Figure 4.2 – The Mach number $uc/(\Gamma v_s)$, the accretion rate in Eddington units $\dot{m}$, the gas temperature T and the radiative luminosity $l = 4\pi r^2 c w_1/L_E$ are plotted versus $\log(r/r_g)$ for model 1L at different times.

(located at $r \simeq 10^9 r_g$) down to the black hole horizon. Temperature and luminosity relax very quickly to their stationary values. In the optically thick inner core, matter and radiation are in LTE and the luminosity is proportional to the local value of the temperature gradient; in the outer region compressional heating balances free–bound cooling and the gas is essentially in radiative energy equilibrium at the hydrogen recombination temperature, $T \simeq 10^4 K$.

For models on the high luminosity branch, the behaviour of the time–dependent solutions is completely different. In figures 4.3 and 4.4, we show the results of numerical calculations for models 2H and 1H, respectively. For model 2H a small deviation from free–fall is observed in the velocity profile at around 10^3–$10^4 r_g$, due to the high gradients in the gas pressure. However, even in this case, the matter fluid is essentially in free–fall and the accretion rate is constant. The interpretation of the temperature and luminosity profiles shown in figure 4.3 is less straightforward. They do not seem to converge at all toward the stationary solutions found by NTZ, but, after 70 seconds, they are still in essentially the initial perturbed state. We postpone discussion of these solutions to the end of this section.

For model 1H (having larger $\dot{m}$), a thermal instability appears in the inner part of the flow after about 2–3 seconds, as can be seen from figure 4.4, and the temperature increases by almost an order of magnitude. The cause of the onset of this instability will be discussed later. A few seconds after this, the velocity profile starts to deviate significantly from free–fall owing to the large drag exerted by the internal pressure gradients. A compression wave develops, whose front becomes progressively steeper as it propagates outward and, after 8–10 seconds, a hydrodynamic shock forms at around 10^3–$10^4 r_g$. Across the shock, the kinetic energy of the gas is dissipated into thermal energy and the density increases; matter starts to accumulate at the shock front and a corresponding decrease in ρ is seen in the inner region. Immediately behind the shock front, the gas accelerates and free–fall is rapidly restored. We note that, since the shock is very far away from the black hole horizon, the local free–fall velocity is $\sim 10^{-2} c$; for this reason the kinetic energy dissipated at the shock is relatively small and the radiative luminosity does not increase significantly through it. As far as we know, this is the first time that a shock has been found in self–consistent solutions of black hole accretion (see Chang & Ostriker 1985 for a discussion of shock formation in stationary models). The large increase of l in the first 3 seconds (by more than one order of magnitude) is due to the enhancement in efficiency of free–free and Compton cooling caused by the increase
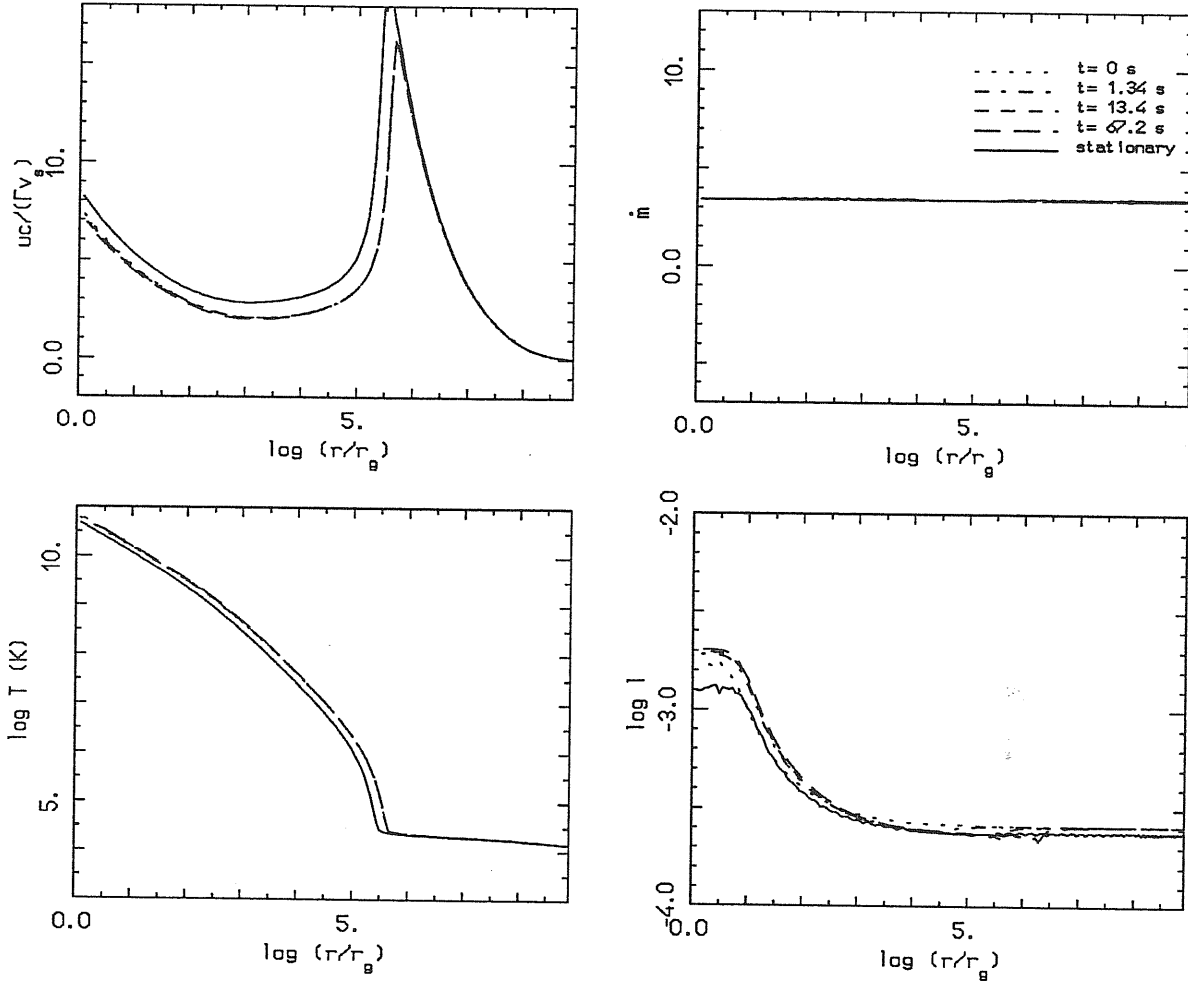
Figure 4.3 – The same as figure 4.2 for model 2H.

in T. Looking carefully at the profile of the Mach number, it can be seen that the shock front is moving outward, at an approximate speed of 10^8 cm/s $\simeq 10^{-2}c$. Hence this solution is definitely non–stationary as confirmed by the fact that the accretion rate is not constant and matter keeps accumulating at the shock front. With the aim of getting a better treatment of the shock region, we repeated the calculation inserting a source of artificial viscosity. Figure 4.4 shows the result of this computation. Following the standard prescription by von Neumann and Richtmyer (1950), a dissipative term Q,
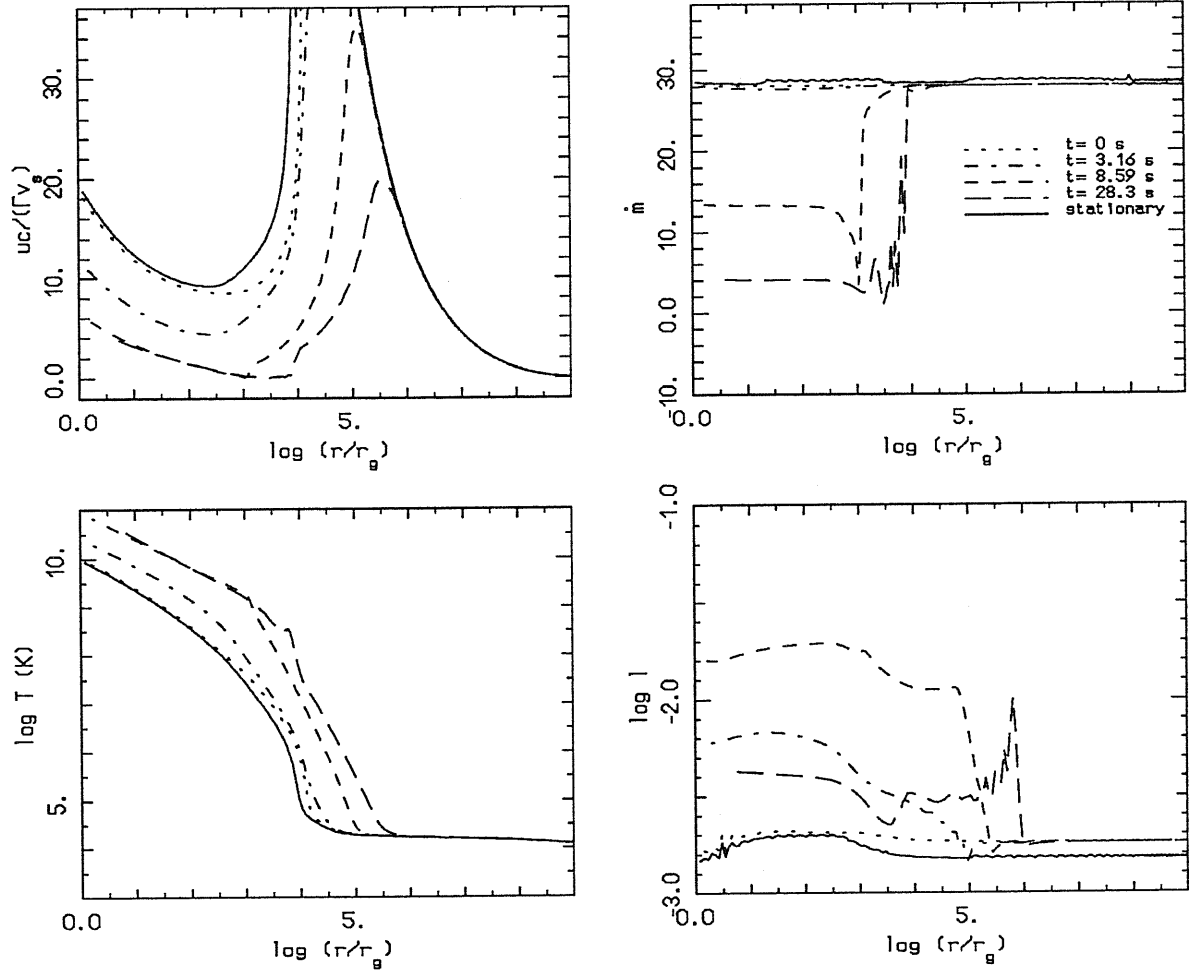
Figure 4.4 – The same as figure 4.2 for model 1H.

proportional to $\rho_{i-1/2}\left(u_i - u_{i-1}\right)^2$, was inserted into the equations (here the subscripts indicate the locations on the finite difference grid at which each variable is evaluated; i represents a zone boundary and $i - 1/2$ represents a mid–zone). However, since the flow is being compressed continuously from the sonic radius down to the black hole horizon, the amount of dissipation would be excessive, especially in the vicinity of r_g, unless some modification is made to the standard procedure. In view of this, we decided to switch on the artificial viscosity only when the fractional variation of u across a grid
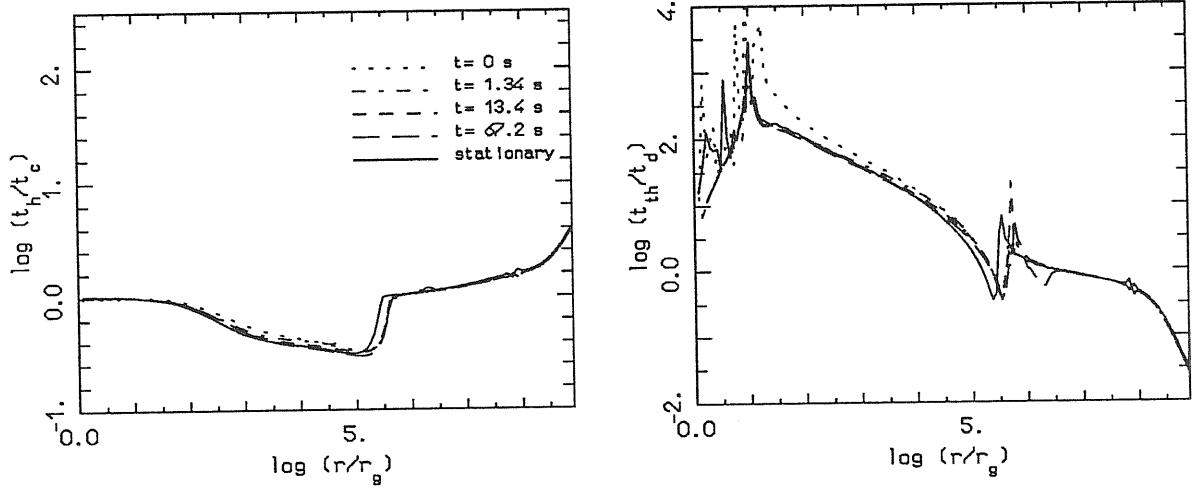
Figure 4.5 – Ratios of the heating time (t_h) to the cooling time (t_c) and of the thermal time (t_{th}) to the dynamical time (t_d) plotted against $\log(r/r_g)$ for model 2H at different times.

zone $\alpha = 2(u_i - u_{i-1})/(u_i + u_{i-1})$ becomes larger than 30%. As the shock forms, α increases above 0.3 and the viscous term

$$Q_{i-1/2} = k \left(1 - \frac{0.3}{\alpha}\right) \rho_{i-1/2} \left(u_i - u_{i-1}\right)^2 c^2 \qquad (4.19)$$

then starts to be progressively more effective. Here k is an adjustable constant ($k = 2$ in the actual calculation). About 30 seconds after the beginning of the evolution and approximately 20 seconds after the shock formation, we were nevertheless forced to stop the calculation because of the formation of large numerical oscillations at the shock front and some more sophisticated treatment would clearly be desirable. However, for the present purposes, we were content simply to demonstrate the existence of the shocked solutions.

The evolution described for model 1H, with the appearance of a thermal instability and the formation of a hydrodynamic moving shock, is a common feature of all of the high luminosity models along the high $\dot{m}$ part of the HL branch. We have made a systematic search for the point on the $(\dot{m}, l)$ plane which marks the onset of the
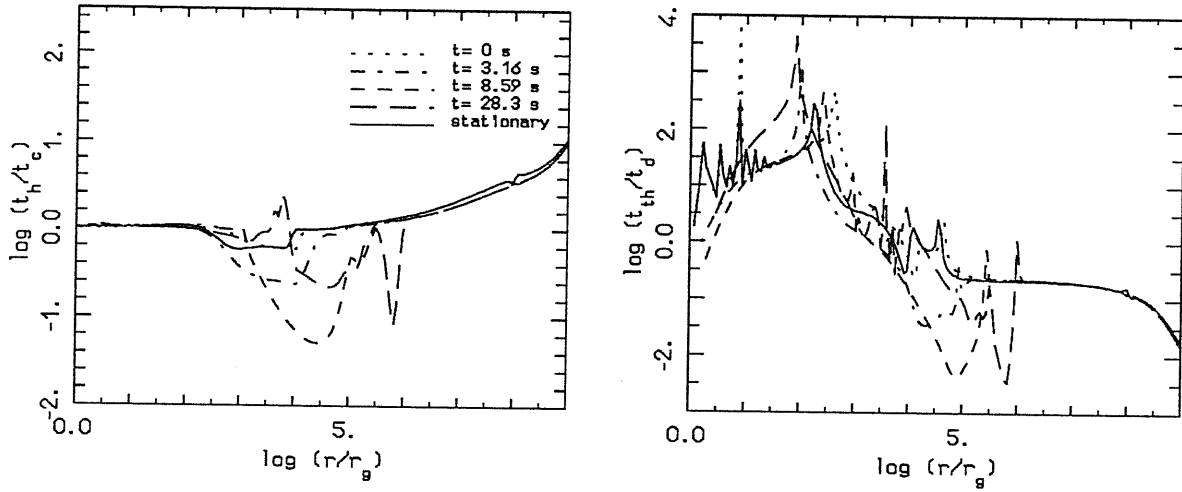
Figure 4.6 – The same as figure 4.5 for model 1H.

instability and the result is shown in figure 4.1, where all of the HL unstable models are plotted as open circles. According to the analysis of Field (1965) and Stellingwerf (1982), the form of the free–free cooling function implies that the gas should be thermally unstable to isobaric short–wavelength perturbations so that, if the Compton heating rate exceeds the cooling rate at some radius, it will continue to do so until matter there has been heated to a temperature which is essentially equal to that of the radiation. In the present case, owing to the large value of the Compton parameter Y_c, Compton cooling is equally as efficient as Compton heating and the analysis by Stellingwerf (1982) does not strictly apply. However, as discussed by Cowie, Ostriker & Stark (1978), the instability is clearly due to the fact that the heating rate is greater than the cooling rate and, at the same time, the heating time is shorter than the dynamical time. In figures 4.5 and 4.6, we have plotted the ratios of the heating time (t_h) to the cooling time (t_c) and of the thermal time (t_{th}) to the dynamical time (t_d). These quantities are plotted against r/r_g at different times for models 2H and 1H, respectively. As can be seen from figure 4.6, at the beginning t_h is slightly smaller than t_c in the region around 10^3–$10^4 r_g$. There,

heating exceeds cooling and, since the flow cannot advect the excess energy efficiently $(t_d \simeq t_{th})$, a small perturbation is sufficient to make heating more effective and the onset of a thermal instability is unavoidable. Also the value of the thermal time–scale, $t_{th}(10^3 r_g) \sim t_d(10^3 r_g) \sim 1$ s, is consistent with the time–scale for the onset of the instability found numerically. The region of instability then moves to larger radii, as can be seen from figure 4.6, and so it is not surprising that the shock keeps moving outward. On the other hand, figure 4.5 shows that the ratio t_{th}/t_d is significantly larger than unity for model 2H in the region where heating is more effective than cooling and so the thermal instability is advected into the hole on a dynamical time–scale. In other words, since the models along the low $\dot{m}$ part of the HL branch have small gas densities, the radiative heating and cooling are comparatively less efficient than compressional heating and the gas is essentially adiabatic. Only very far away, around $3 \times 10^5 r_g$, do the conditions seem to be favourable for the onset of the thermal instability; however, the thermal time–scale in that region is $\sim 10^3$ s and the evolutionary time becomes very large. This means that these solutions might also be unstable but on much longer time–scales.

Then, we confirm that all of the low luminosity, NTZ stationary solutions, which are characterized by negligible comptonization, are indeed stable to thermal and radiative perturbations in agreement with previous investigations (e.g. Gilden & Wheeler 1980; Vitello 1984). On the other hand, the time evolution of high luminosity solutions, for which self–comptonization of bremsstrahlung photons is the main radiative and thermal process, exhibits a much richer phenomenology. As we have shown, the upper part of the HL branch (for $\dot{m} \gtrsim 10$) enters the region of the $(\dot{m}, l)$ plane where preheating effects start to be important and this leads to the onset of a strong thermal instability giving rise to the formation of an outward–propagating hydrodynamic shock. These shocked solutions show significant transient increases in the total luminosity. Finally, we note that, during the evolutionary times considered, we did not find any evidence for possible transitions between the HL and the LL branch.

We are planning to apply this code also to the study of the stability and the time-dependent behaviour of accreting neutron stars in order to shed further light on the observational properties both of the bright LMXBs accreting near the Eddington limit and of the ONSs accreting from the interstellar medium.

APPENDIX A

In this appendix we derive the solution of the Fokker–Planck equation (2.10) for the variable $u_1 = W_1 t^{-2}$. This solution is obtained applying to $\tilde{u}_1$ (equation (2.15)) the inverse Fourier transformation

$$u_1 = \frac{1}{2\pi} \int_{-\infty}^{+\infty} \tilde{u}_1 e^{ikt} dk \,. \tag{A1}$$

By defining $\xi = 1/e^{z-z_0} = (\nu_0/\nu)^{3/(2+\beta)}$ and introducing the new complex variable $s = ik(1/\xi - 1) + 1$, the Fourier integral (A1) can be cast in the form

$$u_1 = \frac{A}{2\pi i} \frac{\xi}{1-\xi} \exp\left(-\frac{\xi t + t_0}{1-\xi}\right) \int_{1-i\infty}^{1+i\infty} s^{1+\beta} \exp\left(\frac{\xi t}{1-\xi} s + \frac{t_0}{1-\xi} \frac{1}{s}\right) ds \,. \tag{A2}$$

It can be shown (see e.g. Grobner & Hofreiter 1973; Prudnikov, Brychkov & Marichev 1986) that equation (A2) is an integral representation of the Bessel function J_α:

$$J_\alpha(2\sqrt{pq}) = \frac{1}{2\pi i} \left(\frac{p}{q}\right)^{\alpha/2} \int_{\lambda-i\infty}^{\lambda+i\infty} s^{\alpha-1} e^{ps-q/s} ds \,. \tag{A3}$$

Comparing equation (A2) and (A3), we get

$$u_1 = A \frac{\xi}{1-\xi} \left(\frac{t_0}{\xi t}\right)^{(2+\beta)/2} \exp\left(-\frac{\xi t + t_0}{1-\xi}\right) (-1)^{(2+\beta)/2} J_{2+\beta}\left[2i \frac{(\xi t t_0)^{1/2}}{1-\xi}\right] \,. \tag{A4}$$

Taking into account that $(-1)^{\alpha/2} J_\alpha(iu) = I_\alpha(u)$ (u real and positive), we finally have

$$u_1 = A \frac{\xi^{-\beta/2}}{1-\xi} \left(\frac{t_0}{t}\right)^{(2+\beta)/2} \exp\left(-\frac{\xi t + t_0}{1-\xi}\right) I_{2+\beta}\left[2 \frac{(\xi t t_0)^{1/2}}{1-\xi}\right] \,, \tag{A5}$$

which is exactly equation (2.16). We note that, although the absolute convergence on the complex plane of the integral representation (A3) is proved only for p, q, $\lambda > 0$ and Re $\alpha < 1$, direct substitution of equation (A5) into the Fokker–Planck equation (2.10) shows that (A5) is a solution with the only restriction $\xi < 1$. Moreover, equation (A5) coincides with the solution obtained by Payne & Blandford (1981) using separation of variables.

Finally, in strict analogy with what has been done here, it is possible to show that the solution of equation (2.21) for a radial outflow is given by equation (2.22) (with $\xi > 1$).

APPENDIX B
EQUATION FOR THE RADIATION TEMPERATURE

In this appendix we derive the expression of the equation for the radiation temperature which has been used in the calculations presented in Chapter 4. As discussed in section 4.2.1, we assume that equation (4.11), which gives the fractional change of the mean photon energy in a medium at rest because of scatterings with a thermal, non–relativistic distribution of electrons (Rybicki & Lightman 1979; Wandel, Yahil & Milgrom 1984; Park & Ostriker 1989; Park 1990a), is valid along the outward–pointing characteristics of the radiation field, $\mu_c(t)$ (defined from the moment equations (1.42) and (1.43)), with the optical depth being defined along the same lines by

$$\tau = \int_\mu^\infty k_{es}\rho b\Gamma d\mu . \qquad (B1)$$

Then, we have

$$\frac{d\tau}{d\mu} = -k_{es}\rho b\Gamma . \qquad (B2)$$

(Throughout this Appendix the total derivatives are taken along the outward–pointing characteristics of the radiation field). Using equations (B2) and (4.11), we can write

$$\frac{dT_\gamma}{dt} = \frac{dT_\gamma}{d\tau}\frac{d\tau}{d\mu}\dot{\mu}_c = -k_{es}\rho b\Gamma\dot{\mu}_c\frac{dT_\gamma}{d\tau} = -a\Gamma v_c\frac{2k_{es}\rho Y_c}{\tau}T_\gamma\left(\frac{T_\gamma}{T} - 1\right) , \qquad (B3)$$

where $\dot{\mu}_c = d\mu_c/dt$ and $v_c = b\dot{\mu}_c/a$. However, also

$$\frac{dT_\gamma}{dt} = \left.\frac{\partial T_\gamma}{\partial t}\right|_\mu + \left.\frac{\partial T_\gamma}{\partial \mu}\right|_t \dot{\mu}_c \qquad (B4)$$

and so we finally get

$$\left.\frac{\partial T_\gamma}{\partial t}\right|_\mu = -a\Gamma v_c\left[\frac{2k_{es}\rho Y_c}{\tau}T_\gamma\left(\frac{T_\gamma}{T} - 1\right) + \frac{1}{b\Gamma}\left.\frac{\partial T_\gamma}{\partial \mu}\right|_t\right] . \qquad (B5)$$

In practice, we obviously cannot calculate the integrated value of τ directly from expression (B1) evaluated along the outward–pointing characteristics for the radiation since this would involve knowledge of information ahead of the current time reached in the calculation. Instead, we evaluated equation (B1) along the time–slice and this should give reasonable values. While it is important to calculate the *derivative* (B2) along the correct directions in order to ensure a satisfactorily causal propagation of information, the calculation of the *integral* (B1) should not be so sensitive.

To derive the stationary limit of equation (B5), we need first to write it in terms of the Eulerian time and radial coordinates, $(\tilde{t}, r)$. Using the chain rule for differentiation in equation (B5), we obtain

$$\tilde{t}_t \frac{\partial T_\gamma}{\partial \tilde{t}}\bigg|_r + r_t \frac{\partial T_\gamma}{\partial r}\bigg|_{\tilde{t}} = -a\Gamma v_c \left[\frac{2k_{es}\rho Y_c}{\tau} T_\gamma \left(\frac{T_\gamma}{T} - 1 \right) + \frac{1}{b\Gamma} \tilde{t}_\mu \frac{\partial T_\gamma}{\partial \tilde{t}}\bigg|_r + \frac{1}{b\Gamma} r_\mu \frac{\partial T_\gamma}{\partial r}\bigg|_{\tilde{t}} \right].$$

$$(B6)$$

The condition of stationarity is expressed with respect to the fixed (constant r) Eulerian observers by

$$\frac{\partial}{\partial \tilde{t}}\bigg|_r = 0.$$

$$(B7)$$

Taking the stationary limit in equation (B6) and using $r_t = acu$ and $r_\mu = b\Gamma$ finally yields

$$\left(1 + \frac{uc}{\Gamma v_c} \right) \frac{\partial T_\gamma}{\partial r}\bigg|_{\tilde{t}} = -\frac{2k_{es}\rho Y_c}{\tau} T_\gamma \left(\frac{T_\gamma}{T} - 1 \right),$$

$$(B8)$$

which corresponds to equation (4.14).

REFERENCES

Abramowitz, M., & Stegun, L. 1970, "Handbook of Mathematical Functions" (New York: Dover)

Alme, M.L., & Wilson, J.R. 1973, ApJ, 186, 1015 (AW)

Alpar, M.A., & Shaham, J. 1985, Nature, 316, 18

Anderson, J.L., & Spiegel, E.A. 1972, ApJ, 171, 127

Anile, A.M., & Romano, V. 1992, ApJ, 386, 325

Barret, D., & Vedrenne, G. 1994, ApJ, 92, 505

Begelman, M.C. 1978, A&A, 70, 583

Begelman, M.C. 1979, MNRAS, 187, 237

Belloni, T., & Zampieri, L. 1995, in preparation

Bhattacharya, D., Wijers, R.A.M.J., Hartman, J.W., & Verbunt, F. 1992, A&A, 254, 198

Bildsten, L., Salpeter, E.E., & Wasserman, I. 1992, ApJ, 384, 143

Bisnovatyi–Kogan, G.S., & Blinnikov, S.I. 1980, MNRAS, 191, 711

Blaes, O., & Madau, P. 1993, ApJ, 403, 690 (BM)

Blaes, O., & Rajagopal, M. 1991, ApJ, 381, 210

Blandford, R.D., & Payne, D.G. 1981a, MNRAS, 194, 1033

Blandford, R.D., & Payne, D.G. 1981b, MNRAS, 194, 1041

Bloemen, J.B.G.M. 1987, ApJ, 322, 694

Blondin, J.M. 1986, ApJ, 308, 755

Blumenthal, G.R., & Mathews, W.G. 1976, ApJ, 203, 714

Bondi, H. 1952, MNRAS, 112, 195

Bowers, R.L., & Wilson, J.R. 1991, "Numerical Modeling in Applied Physics and Astrophysics" (Boston: Jones & Bartlett Publishers)

Bradt, H.V.D., McClintock, J.E. 1983, ARA&A, 21, 13

Branduardi, G., Kylafis, N.D., Lamb, D.Q., & Mason, K.O. 1980, ApJ, 235, L153

Brinkmann, W. 1980, A&A, 85, 146

Buff, J., & McCray, R. 1974, ApJ, 189, 147

Castor, J.I. 1972, ApJ, 178, 779

Cernohorsky, J., & Bludman, S.A. 1994, ApJ, 433, 250

Chandrasekhar, S. 1960, "Radiative Transfer" (New York: Dover)

Chang, K.M., & Ostriker, J.P. 1985, ApJ, 288, 428

Chiappetti, L., *et al.*

Colpi, M. 1988, ApJ, 326, 223

Colpi, M., Campana, S., & Treves, A. 1993, A&A, 278, 161

Comastri, A., Setti, G., Zamorani, G., & Hasinger, G. 1995, A&A, in press

Cowie, L.L., Ostriker, J.P., & Stark, A.A. 1978, ApJ, 226, 1041

Cowley, A.P., Crampton, D., & Hutchings, J.B. 1979, ApJ, 231, 539

Dame, T.M., *et al.* 1987, ApJ, 322, 706

De Boer, H. 1991, in Proceedings of the 144th IAU Symposium, H. Bloemen ed.
    (Kluwer: Dordrecht), 333

Diamond, C.J., Jewell, S.J., & Ponman, T.J. 1995, MNRAS, 274, 589

Dickey, J.M., & Lockman, F.J. 1990, ARA&A, 28, 215

Field, G.B. 1965, ApJ, 142, 431

Flammang, R.A. 1982, MNRAS, 199, 833

Flammang, R.A. 1984, MNRAS, 206, 589

Forman, W.C., *et al.*, 1978, ApJS, 38, 357

Fortner, B., Lamb, F.K., & Miller, G.S. 1989, Nature, 342, 775

Freihoffer, D. 1981, A&A, 100, 178

Frisch, P.C., & York, D.G. 1983, ApJ, 271, L59

Fu, A. 1987, ApJ, 323, 227

Gilden, D.L., & Wheeler, J.C. 1980, ApJ, 239, 705

Gillman, A.W., & Stellingwerf, R.F. 1980, ApJ, 240, 235

Gröbner, W., & Hofreiter, N. 1973, "Integraltafel" (Wien: Springer–Verlag)

Hasinger, G. 1987, A&A, 186, 153

Hasinger, G., Lanmeier, A. Sztajno, M., Trümper, J., Lewin, W.H.G., & White, N. 1986, Nature, 319, 469

Hasinger, G., Burg, R., Giacconi, R., Hartner, G., Schmidt, M., Trümper, J., & Zamorani, G. 1993, A&A, 275, 1

Hasinger, G., & van der Klis, M. 1989, A&A, 225, 79

Hasinger, G., *et al.* 1990, A&A, 235, 131

Hauschildt, P.H., & Wehrse, R. 1991, JQSRT, 46, 81

Helfand, D.J., Chanan, G.A., & Novick, R. 1980, Nature, 283, 337

Hewish, A., Bell, S.J., Pilkington, J.D.H., Scott, P.F., & Collins, R.A. 1968, Nature, 217, 709

Hirano, T., *et al.* 1984, PASJ, 36, 769

Hirano, T., *et al.* 1995, ApJ, 446, 350

Kafka, P., & Mèszàros, P. 1976, Gen. Rel. Grav., 7, 841

Karzas, W.J., & Latter, R. 1961, ApJS, 6, 167

Katz, J.I. 1976, ApJ, 206, 910

Kershaw, D.S. 1987, JQSRT, 38, 347

Kershaw, D.S., Prasad, M.K., & Beason, J.D. 1986, JQSRT, 36, 273

Kluźniak, W., & Wilson, J.R. 1991, ApJ, 372, L87

Kompaneets, A.S. 1957, Soviet Phys.–JEPT 4, 730

Krolik, J.H., & London, R.A. 1983, ApJ, 267, 18

Kulkarni, S.R. 1986, ApJ, 306, L85

Lamb, F.K. 1989, in Proceedings of the 23rd ESLAB Symposium "Two Topics in X–ray Astronomy", N.E. White ed. (ESA SP–296), 215

Lamb, F.K. 1991, in "Neutron Stars: Theory and Observation", J. Ventura & D. Pines eds. (Dordrecht: Kluwer), 445

Lamb, F.K., Shibazaki N., Alpar M.A., & Shaham J. 1985, Nature, 317, 681

Levermore, C.D., & Pomraning, G.C. 1981, ApJ, 248, 321

Lindquist, R.W. 1966, Ann. Phys. (N.Y.), 37, 487

Loeb, A., Mc Kee C.F., & Lohav, O. 1991, ApJ, 374, 44

London, R.A., Taam, R.E., & Howard, W.E. 1986, ApJ, 306, 170

Lyne, A.G., & Lorimer, D.R. 1994, Nature, 369, 127

Lyne, A.G., Manchester, R.N., & Taylor, J.H. 1985, MNRAS, 213, 613

Madau, P., & Blaes, O. 1994, ApJ, 423, 748

Maoz, E., & Grindlay, J.E. 1995, ApJ, 444, 183 (MG)

Maraschi, L., Reina, C., & Treves, A. 1974, A&A, 35, 389

Maraschi, L., Reina, C., & Treves, A. 1978, A&A, 66, 99

Mastichiadis, A., & Kylafis, N.D. 1992, ApJ, 384, 136 (MK)

Matt, G., Costa, E., Dal Fiume, D., Dusi, W., Frontera, F., & Morelli, E. 1990, ApJ, 355, 468

Maurer, G.S., Neil Johnson, W., Kurfess, J.D., & Strickman, M.S. 1982, ApJ, 254, 271

May, M.M., & White, R.H. 1967, "Methods in Computational Physics", Vol. 7, B. Alder, S. Fernbach, & M. Rotenberg eds. (New York: Academic Press)

McCammon, D., & Sanders, W.T. 1990, ARA&A, 28, 657

Melia, F., & Zylstra, G.J. 1991, ApJ, 374, 732

Mèszàros, P. 1975, A&A, 44, 59

Michel, F.C. 1972, Ap&SS, 15, 153

Middleditch, J., & Priedhorsky, W.C. 1986, ApJ, 306, 230

Mihalas, D. 1980, ApJ, 237, 574

Mihalas, D., Kunasz, P.B., & Hummer, D.G. 1975, ApJ, 202, 465

Mihalas, D., Kunasz, P.B., & Hummer, D.G. 1976, ApJ, 206, 515

Mihalas, D., & Weibel Mihalas, B. 1984, "Foundations of Radiation Hydrodynamics" (Oxford: Oxford University Press)

Mihalas, D., Winkler, K–H., & Norman, M.L. 1984, JQSRT, 31, 479

Miller, G.S. 1990, ApJ, 356, 572

Miller, G.S., & Lamb, F.K. 1992, ApJ, 388, 541

Miller, G.S., & Park, M.-G. 1995, ApJ, 440, 771

Miller, J.C., & Rezzolla, L. 1995, Phys. Rev. D, 51, 4017

Miller, M.C. 1992, MNRAS, 255, 129

Mitsuda, K. 1992, in Proceedings of the 28th Yamada Conference "Frontiers of X-ray Astronomy", Y. Tanaka & K. Koyama eds. (Universal Academy Press), 115

Mitsuda, K., *et al.* 1984, PASJ, 36, 741

Mitsuda, K., Inoue, H., Nakamura, N., & Tanaka, Y. 1989, PASJ, 41, 97

Moncrief, V. 1980, ApJ, 235, 1083

Morrison, R., & McCammon, D. 1983, ApJ, 270, 119

Narayan, R., & Ostriker, J.P. 1990, ApJ, 270, 119

Nelson, R.W., Wang, J.C.L., Salpeter, E.E., & Wasserman, I. 1995, ApJ, 438, L99

Nobili, L., Calvani, M., & Turolla, R. 1985, MNRAS, 214, 161

Nobili, L., Turolla, R., & Zampieri, L. 1991, ApJ, 383, 250 (NTZ)

Nobili, L., Turolla, R., & Zampieri, L. 1993, ApJ, 404, 686

Nomoto, K., & Tsuruta, S., 1987, ApJ, 312, 711

Novikov, I.D., & Thorne, K.S. 1973, in "Black Holes", C. DeWitt & B.S. DeWitt eds. (New York: Gordon & Breach), 343

Ostriker, J.P., McCray, R., Weaver, R., & Yahil, A. 1976, ApJ, 208, L61

Ostriker, J.P., Rees, M.J., & Silk, J. 1970, Astrophys. Letters, 6, 179

Paczyński, B. 1990, ApJ, 348, 485

Paresce, F. 1984, AJ, 89, 1022

Park, M.-G. 1990a, ApJ, 354, 64

Park, M.-G. 1990b, ApJ, 354, 83

Park, M.-G., & Miller, G.S. 1991, ApJ, 371, 708

Park, M.-G., & Ostriker, J.P. 1989, ApJ, 347, 679

Payne, D.G., & Blandford, R.D. 1981, MNRAS, 196, 781 (PB)

Pomraning, G.C. 1973, "The Equations of Radiation Hydrodynamics" (Oxford: Pergamon Press)

Ponman, T.J., Foster, A.J., & Ross, R.R. 1990, MNRAS, 246, 287

Prasad, M.K., Shestakov, A.I., Kershaw, D.S., & Zimmerman G.B. 1988, JQSRT, 40, 29

Prudnikov, A.P., Brychkov, Yu.A., & Marichev, O.I. 1986, "Integrals and Series" (New York: Gordon and Breach)

Psaltis D., Lamb F.K., & Miller, G.S. 1995, ApJ Letters, submitted

Rees, M.J. 1978, Phys. Scripta, 17, 193

Rezzolla, L., & Miller, J.C. 1994, Class. Quantum Grav, 11, 1815

Romani, R.W. 1987, ApJ, 313, 718

Rybicki, G.B., & Lightman, A.P. 1979, "Radiative Processes in Astrophysics" (New York: Wiley)

Schinder, P.J. 1988, Phys. Rev. D, 38, 1673

Schinder, P.J., & Bludman, S.A. 1989, ApJ, 346, 350

Schmid–Burgk, J. 1978, Ap&SS, 56, 191

Schneider, P., & Bogdan, T.J. 1989, ApJ, 347, 496

Schulz, N.S., Hasinger, G., Trümper, J. 1989, A&A, 225, 48

Service, A.T. 1986, ApJ, 307, 60

Shakura, N.I., & Sunyaev, R.A. 1973, A&A, 24, 337

Shapiro, S.L. 1973a, ApJ, 180, 531

Shapiro, S.L. 1973b, ApJ, 185, 69

Shapiro, S.L., & Salpeter, E.E. 1973, ApJ, 198, 761

Shestakov, A.I., Kershaw, D.S., & Prasad, M.K. 1988, JQSRT, 40, 577

Shibanov, Yu.A., Zavlin, V.E., Pavlov, G.G., & Ventura, J. 1992, A&A, 266, 313

Shull, J.M. 1979, ApJ, 229, 1092

Shvartsman, V.F. 1971, Soviet Astr.-AJ, 15, 377

Simon, R. 1963, JQSRT, 3, 1

Soffel, M.H. 1982, A&A, 116, 111

Stellingwerf, R.F. 1982, ApJ, 260, 768

Stellingwerf, R.F., & Buff, J. 1978, ApJ, 221, 661

Stellingwerf, R.F., & Buff, J. 1982, ApJ, 260, 755

Stocke, J.T., Wang, Q.D., Perlman, E.S., Donahue, M., & Schachter, J. 1995, AJ, 109, 1199

Sunyaev, R.A., & Titarchuk, L.G. 1980, A&A, 86, 121

Sunyaev, R.A., *et al.* 1991, Sov. Astron. Lett., 17, 409

Szuszckiewicz, E., & Miller, J.C. 1995, in preparation

Tamazawa, S., Toyama, K., Kaneko, N., & Ôno, Y. 1974, Ap&SS, 32, 403

Thomas,L.H. 1930, Q. J. Math., 1, 239

Thorne, K.S. 1981, MNRAS, 194, 439

Thorne, K.S., Flammang, R.A., & Żytkow, A.N. 1981, MNRAS, 194, 475

Treves, A., & Colpi, M. 1991, A&A, 241, 107 (TC)

Treves, A., Colpi, M., & Lipunov, V.M. 1993, A&A, 269, 319

Turolla, R., & Nobili, L. 1988, MNRAS, 235, 1273

Turolla, R., Zampieri, L., Colpi, M., & Treves, A. 1994, ApJ, 426, L35

Turolla, R., Zampieri, L., & Nobili, L. 1995, MNRAS, 272, 625, 629

Vacca, W.D., *et al.* 1987, A&A, 172, 143

van der Klis, M. 1989, ARA&A, 27, 517

van der Klis, M. 1991, in "Neutron Stars: Theory and Observation", J. Ventura & D. Pines eds. (Dordrecht: Kluwer), 319

van der Klis, M., Jansen, F., van Paradijs, J., Lewin, H.G., van den Heuvel, E.P.J., Trümper, J.E., & Sztajno, M. 1985, Nature, 316

van Paradijs, J., & van der Klis, M. 1994, A&A, 281, L17

Vitello, P.A.J. 1978, ApJ, 225, 694

Vitello, P.A.J. 1984, ApJ, 284, 394

von Neumann, J., & Richtmyer, R.D. 1950, J. Appl. Phys., 21, 232

Vrtilek, S.D., *et al.* 1986, ApJ, 307, 698

Wandel, A., Yahil, A., & Milgrom, M. 1984, ApJ, 282, 53

Webber, Y., & Reinert, C. P. 1970, ApJ, 162, 883

Welsh, B.Y., Craig, N., Vedder, P.W., & Vallerga, J.V. 1994, ApJ, 437, 638

White, N.E., Nagase, F., & Parmar A.N. 1993, in "X–ray Binaries", W.H.G. Lewin, J. van Paradijs, & E.P. van den Heuvel (Cambridge University Press), 1

White, N.E., Peacock, A. & Taylor, B.G. 1985, ApJ, 296, 475

White, N.E., *et al.* 1986, MNRAS, 218, 129

White, N.E., Stella, L., & Parmar, A.N. 1988, ApJ, 324, 363

Wielen, R. 1977, A&A, 60, 263

Zampieri, L., Miller, J.C., Turolla, R. 1995, MNRAS, submitted

Zampieri, L., Turolla, R., & Treves, A. 1993, ApJ, 419, 311

Zampieri, L., Turolla, R., Zane, S., & Treves, A. 1995, ApJ, 439, 849

Zane, S., Turolla, R., Zampieri, L., Colpi, M., & Treves, A. 1995, ApJ, in press

Zel'dovich, Ya., & Guseynov, O. 1965, ApJ, 144, 840

Zel'dovich, Ya., & Shakura, N. 1969, Soviet Astron.–AJ, 13, 175 (ZS)